



UNIVERSITY OF THE PHILIPPINES

Master of Science in Physics

John Rommel V. Oidem

*Chaos and Escapes of Charged Particles Orbiting Uniformly  
Magnetized Gravitational Centers*

Thesis Adviser:

Michael Francis Ian G. Vega II, Ph.D.  
National Institute of Physics  
University of the Philippines Diliman

Date of Submission:  
June 2024

Thesis Classification:  
**P**

*This thesis is available only after consultation with author/adviser for thesis.*

Title of Thesis / Dissertation: Chaos and Escapes of Charged Particles Orbiting Uniformly  
Magnetized Gravitational Centers

Author: John Rommel V. Oidem

MS Thesis

National Institute of Physics

University of the Philippines Diliman

June 2021

Classification\* : P

\* I – invention or creation, P – publication, C – confidential information

Available to the general public	No
Available only after consultation with author/adviser for thesis	Yes
Available only to those bound by nondisclosure or confidentiality agreement	No



(signature above printed name)

John Rommel V. Oidem

Student



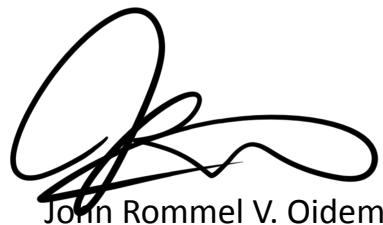
(signature above printed name)

Michael Francis Ian G. Vega II, Ph.D.

Thesis / Dissertation Adviser

### **Honor Code**

By submitting this thesis / dissertation, I affirm that I uphold the core values of Honor and Excellence as codified in the University of the Philippines Code of Student Conduct. This work adheres to the highest standards of academic integrity wherein scholarly sources have been attributed accurately; data has been collected and analyzed in accordance with established academic and scientific practices; and results have been reported in a scholarly and transparent manner.



A handwritten signature in black ink, appearing to read "John Rommel V. Oidem".

Name and Signature of Student

National Institute of Physics  
College of Science  
University of the Philippines  
Diliman, Quezon City

### ENDORSEMENT

This is to certify that this thesis titled, **CHAOS AND ESCAPES OF CHARGED PARTICLES ORBITING UNIFORMLY MAGNETIZED GRAVITATIONAL CENTERS**, prepared and submitted by John Rommel V. Oidem in partial fulfillment of the requirements for the degree of Master of Science in Physics, is recommended for acceptance.

  
MICHAEL FRANCIS IAN G. VEGA II, Ph.D.  
Thesis Adviser  
  
REINABELLE C. REYES, Ph.D.  
Thesis Reader

The National Institute of Physics endorses acceptance of this dissertation in partial fulfillment of the requirements for the degree of Master of Science in Physics.

WILSON O. GARCIA, Ph.D.  
Director  
National Institute of Physics

This dissertation is officially accepted in partial fulfillment of the requirements for the degree of Master of Science in Physics.

GIOVANNI A. TAPANG, Ph.D.  
Dean  
College of Science

PLEASE POST

NATIONAL INSTITUTE OF PHYSICS

PLEASE POST

College of Science  
University of the Philippines  
Diliman, Quezon City

ANNOUNCEMENT OF THE MASTER'S EXAMINATION

of

**JOHN ROMMEL V. OIDEM**

in defense of his M.S. Thesis

**CHAOS AND ESCAPES OF CHARGED PARTICLES ORBITING UNIFORMLY MAGNETIZED  
GRAVITATIONAL CENTERS**

for the degree of M.S. Physics

1:00 P.M., WEDNESDAY, 5 JUNE 2024 at NIP R211.

**THESIS ADVISER**

**THESIS READER**

MICHAEL FRANCIS IAN G. VEGA II, Ph.D.  
Professor of Physics  
National Institute of Physics  
C.S., U.P. Diliman, Quezon City

REINABELLE C. REYES, Ph.D  
Associate Professor of Physics  
National Institute of Physics  
C.S., U.P. Diliman, Quezon City

**THESIS EXAMINER**

**THESIS EXAMINER**

MIGUEL A. SULANGI, Ph.D.  
Associate Professor of Physics  
National Institute of Physics  
C.S., U.P. Diliman, Quezon City

WILSON O. GARCIA, Ph.D.  
Professor of Physics  
National Institute of Physics  
C.S., U.P. Diliman, Quezon City

**ENDORSED BY:**

  
WILSON O. GARCIA, Ph.D.  
Director  
National Institute of Physics 

**AUTHORIZED BY:**

  
GIOVANNI A. TAPANG, Ph.D.  
Dean  
College of Science

# Acknowledgments

I would like to show my appreciation to..

**Sir Ian** my adviser, for his dedication, patience, and excellence that inspires me to strive.

**Ma'am Reina** my reader, for her care and meticulousness that has significantly improved my manuscript.

**Sir Sulangi and Sir Garcia** my examiners, for their challenging and thoughtful inquiries that have tempered my work for the better

**My dear friends** who have shown me that I can become a better person

## ABSTRACT

### CHAOS AND ESCAPES OF CHARGED PARTICLES ORBITING UNIFORMLY MAGNETIZED GRAVITATIONAL CENTERS

**John Rommel V. Oidem**  
**University of the Philippines (2024)**

**Adviser:**  
**Michael Francis Ian G. Vega II,  
Ph.D.**

We study the chaotic and escape dynamics of a charged massive particle in a uniform magnetic field, orbiting either a Newtonian point mass, or a Schwarzschild black hole. We derive a non-dimensionalized Hamiltonian for both cases, then quantify the following: the equilibrium points that gives the local extremum of the potential , the energy value that opens the permissible phase space to infinity which loosely imply escape, and the position of the opening of the escape channel. The exact location where trajectories can be qualified as “escaped”, called the escape basins, are located at infinity in the two systems, which would mean that typical escape definitions cannot be used. So we construct our own definition of escape using the fact that the asymptotic motion of the system is a cyclotron. With the new definition of escape, we analyze escapes in both systems using the time it takes for a trajectory to escape, or escape time, and how many times a trajectory crosses the equatorial plane, or escape pass. The systems’ chaotic nature is also investigated, primarily through the Single Alignment Index, which is a scalar quantity that has a distinct convergence in time for ordered and chaotic trajectories. Using these tools that quantify chaos and escape, we derive different qualities of the systems, some of which are the following: the number of trajectories that directly escape depend on the width of the escape channel; also, trajectories that have initial conditions close to escaping trajectories travel further before returning to the equatorial plane which in turn results to them generally have larger escape times. We also show the existence of trapped orbits, trajectories that have energies that allow escape but will never escape the system; this is due to them being closed ordered trajectories. These properties exists for both systems; the main difference are the orbits that may be captured by the black hole, which does not exist for the Newtonian point mass case. All in all, these qualities of escaping trajectories show that energy is not the only limiting factor for escapes in both systems; some initial conditions and parameters can either delay their time of escape greatly, or not allow them to escape at all.

PACS: 04.70.Bw [Classical black holes], 04.20.-q [Classical general relativity], 98.35.Eg [Electric and magnetic fields], 98.62.Dm [Kinematics, dynamics, and rotation]

# Table of Contents

<b>Acknowledgments</b>	<b>i</b>
<b>Abstract</b>	<b>ii</b>
<b>List of Figures</b>	<b>iv</b>
<b>1 Introduction</b>	<b>1</b>
1.1 Uniformly Magnetized Black Holes . . . . .	2
1.2 Escapes . . . . .	2
1.3 Chaos . . . . .	3
1.4 Problem Statement . . . . .	4
<b>2 Magnetized Newtonian Center</b>	<b>5</b>
2.1 System Set-up . . . . .	5
2.2 Hamiltonian of the System . . . . .	6
2.3 Potential Analysis . . . . .	10
2.3.1 Equilibrium Points . . . . .	11
2.3.2 Zero Velocity Curves . . . . .	11
2.3.3 Open Zero Velocity Curves . . . . .	12
2.4 Reparametrization of Energy . . . . .	14
<b>3 Escapes from a Magnetized Newtonian Center</b>	<b>15</b>
3.1 New Definition of Escape . . . . .	16
3.2 Escape Time and Escape Pass . . . . .	18
3.3 0-pass Trajectories . . . . .	22
3.4 Trapped Orbits . . . . .	23
<b>4 Chaos on a Magnetized Newtonian Center</b>	<b>25</b>
4.1 Poincaré Plots . . . . .	25
4.2 SALI . . . . .	29
<b>5 Magnetized Black Hole</b>	<b>37</b>
5.1 System Set-up . . . . .	37
5.2 Hamiltonian of the System . . . . .	39
5.3 Potential Analysis . . . . .	42
5.3.1 Equilibrium . . . . .	42
5.3.2 Open Zero Velocity Curves . . . . .	44

5.3.3	Black Hole Capture . . . . .	45
5.4	Reparametrization . . . . .	45
5.5	Newtonian Limit . . . . .	49
<b>6</b>	<b>Escapes from a Magnetized Black Hole</b>	<b>51</b>
6.1	Escape Definition . . . . .	51
6.2	Escape Quantities . . . . .	52
6.3	0-pass trajectories . . . . .	55
6.4	Trapped Orbits . . . . .	57
<b>7</b>	<b>Chaos on a Magnetized Black Hole</b>	<b>59</b>
<b>8</b>	<b>Summary, Conclusions, and Recommendations</b>	<b>62</b>
<b>A</b>	<b>Code</b>	<b>66</b>
<b>B</b>	<b>LCN vs SALI</b>	<b>67</b>

# List of Figures

2.1	The MNC system in cylindrical coordinates $(r, \theta, z)$ . The test particle has mass $m$ and charge $q$ . It is orbiting a central point mass $M$ immersed in a uniform magnetic field $\mathbf{B}$ along the $+z$ direction. . . . .	6
2.1	Sample 3d trajectories of particles in the MNC, where the origin is marked by a black dot. . . . .	10
2.2	Each dashed curve represents a zero velocity curve of the potential for the given $L$ and $U$ . The sole minimum of the system is shown with a black dot, where the ZVC converges as we reduce the energy to $U_{\text{eq}}$ . Darker colors mean lower magnitudes of the effective potential energy. ZVC's for energies higher than $U_{\text{esc}}$ are omitted. . . . .	12
2.3	Zero Velocity Curves (black) of the potential given $L = 1$ with energies equal to or greater than $U_{\text{esc}}$ in Figs. (2.3a) and (2.3b) respectively. The asymptotes of escape are shown as red dashed lines. Higher energies widens this escape channel. . . . .	13
3.1	Sample trajectories that shows the difference between an escaping and an inescaping trajectory. Escape depends on whether or not the amplitudes of the cyclotronic oscillation (Green) are within the boundaries of the asymptotes of escape (Red). The escaping trajectory in 3d is shown in Fig. (2.1e). The inescaping trajectory in 3d is in Fig. (2.1f), it is shown there that it eventually escapes, not just in this specific launch. . . . .	17
3.2	Newtonian gravity potential energy and specific trajectories, which are a bound elliptic orbit and an unbound escaping elliptic orbit. . . . .	17
3.3	Sample escape plots for constants of motion $E = 1.05$ , $L = 1$ , and maximum integration time $t = 1,000$ . A black line border around the plot bounds all trajectories, everything outside it is kinematically forbidden (negative kinetic energy). . . . .	19
3.4	Escape plot zooming in on the border of ordered trajectories, showing the gradient of escape times that increases as the initial conditions approach the ordered region. Maximum integration time for this plot is $t = 10,000$ to further probe into these asymptotic escape times . .	20
3.5	Heatmap of the turning point $z$ value corresponding to initial conditions of trajectories that do not directly escape and eventually collapse back towards the equatorial plane $z = 0$ . . . . .	21

3.6	Proportion of 0-pass escaping trajectories to the total number of trajectories vs escape channel width. Each point represents a pair of constants of motion $E$ and $L$ . . . . .	22
3.7	Escape time plots for increasing values of $L$ , with a constant energy $E = 1.1$ . Increasing $L$ seems to decrease the number of escaping trajectories. . . . .	23
3.8	Escape pass plots for increasing values of $L$ , with a constant energy $E = 1.1$ . The regions with no escaping trajectories in Fig. (3.7) seem to have high number of passes. . . . .	24
4.1	A sample Poincaré plot (a) with its corresponding trajectory plot (b). . . . .	26
4.2	A sample Poincaré plot for $E = 1.5$ and $L = 1$ with an ensemble of 20 trajectories time integrated until each trajectory generated 200 Poincaré points. Different regions of display different topologies that correspond to ordered and chaotic trajectories, i.e., the region with closed curves are generally ordered periodic and quasi-periodic trajectories, and the region with noise-like structure are chaotic trajectories. . . . .	26
4.3	Sample Poincaré and trajectory plot of an ordered periodic trajectory with constants of motion $(L, E) = (1, 0.5)$ , and initial conditions $(r, p_r, z) = (1.7844903, 0, 0)$ . . . . .	27
4.4	Sample trajectory and Poincaré plot of an ordered quasi-periodic trajectory with constants of motion $(L, E) = (1, 0.5)$ , and initial conditions $(r, p_r, z) = (1.8, 0, 0)$ . . . . .	28
4.5	Sample trajectory and Poincaré plot of a chaotic trajectory with constants of motion $(L, E) = (1, 0.5)$ , and initial conditions $(r, p_r, z) = (1.85, 0, 0)$ . . . . .	29
4.6	Illustration of the time evolution of deviation vectors for ordered and chaotic trajectories. . . . .	30
4.7	Time-evolved SALI values for a periodic ordered (blue), quasi-periodic ordered (orange), and chaotic (green) trajectory. . . . .	31
4.8	Plots for $(L, E) = (1.0, 0.42)$ that differentiate order and chaos. The SALI plot (b) more clearly shows the distinction between ordered and chaotic trajectories compared to the Poincaré plot (a). . . . .	32
4.9	SALI plots of increasing $L$ , with a constant energy $E = 1.1$ . Escaping trajectories are omitted. The regions with no escaping trajectories in Fig. (3.7) have low SALI values. . . . .	33
4.10	SALI plot for $(L, E) = (5.0, 1.0)$ . . . . .	34
4.11	Plots of increasing $L$ , with a constant energy $E = 1.1$ , which show the ordered trajectories in yellow, and chaotic trajectories in blue. . . . .	34
4.12	Heatmap showing the percentage of ordered trajectories for varying $E$ and $L$ . . . . .	35
4.13	Trajectory plots of a trapped orbit showin in 3D (a) and in 2D (b). The gravitational force weak enough to keep the helical motion of the orbits, but strong enough to “trap” the orbit. . . . .	36

5.1	Sample plots of the potential along the equatorial plane. For $ L  <  L_{\text{ISCO}} $ (blue curve), there are no equilibrium points, so the potential energy is monotonically increasing away from $R$ . For $ L  =  L_{\text{ISCO}} $ (orange curve), the equilibrium is located on the ISCO radius $\rho$ . For $ L  >  L_{\text{ISCO}} $ (green), the equilibrium points diverge to two points, the inner being unstable, and the outer being stable. . . . .	43
5.2	Plots that demonstrate how the equilibrium points bifurcate from $\rho$ as $ L $ increases for $L > 0$ values (a) and $L < 0$ values (b). The equilibrium points originate from $L_{\text{ISCO}}$ represented by the dashed black lines. . . . .	43
5.3	Zero Velocity Curves (dashed) of the potential for a given $(B, L)$ with energies equal and greater than $U_{\text{esc}}$ , where the asymptotes of escape are shown in red dashed lines. Higher energies widens this escape channel. . . . .	44
5.4	Each dashed curve represents a zero velocity curve of the potential for a given set of parameters. Darker colors mean lower magnitudes of the effective potential energy, in other words, darker colors represent the “depth” of the energy well. Lower energy ZVC’s are enclosed by the higher energy ones. Each plot represents a pair of parameters $B$ and $L$ chosen such that it differs whether capture to the black hole or escape to infinity opens first for lower energies. We highlight the ZVC that first opens to $z \rightarrow \infty$ (blue) with potential energy $U_{\text{esc}}$ , and the ZVC that first opens to the black hole (red) with potential energy $U_{\text{un}}$ . $U_{\text{st}}$ is the potential energy of the stable equilibrium. . . . .	46
5.5	A plot that demonstrates how the equilibrium points bifurcate from $\rho$ as $r_{\text{esc}}$ increases. The equilibrium points originate from $r_{\text{esc}, \text{ISCO}}$ represented by the dashed black lines. . . . .	48
6.1	Case I: Black hole capture is impossible; $(r_{\text{esc}}, \rho, E) = (4.0, 1.8, 1.2)$ . . . . .	52
6.2	Case II: Black hole capture is possible; $(r_{\text{esc}}, \rho, E) = (1.8, 1.2, 1.2)$ . . . . .	53
6.3	Case III: Black hole capture is possible; $(r_{\text{esc}}, \rho, E) = (3.0, 2.8, 1.2)$ . . . . .	54
6.4	Zoom-ins on the borders of some ordered regions from Fig. (6.2) to demonstrate the asymptotically increasing escape times (a and b), or the lack thereof (c). . . . .	55
6.5	Two trajectories from case II, with initial conditions $R = 1.25$ , and slightly different initial $p^R$ . The equatorial plane (orange) and the ZVC (black) are also displayed. . . . .	56
6.6	Proportion of 0-pass escaping trajectories to the total number of trajectories vs escape channel width. Each point represents a set of parameters $E$ , $\rho$ , and $r_{\text{esc}}$ . . . . .	56
6.7	Escape time plots of increasing $r_{\text{esc}}$ , with constant parameters $\rho = 1.2$ and $E = 1.2$ . Increasing $L$ seems to decrease the number of escaping trajectories. . . . .	58
6.8	Escape pass plots of increasing $r_{\text{esc}}$ , with constant parameters $\rho = 1.2$ and $E = 1.2$ . The regions with no escaping trajectories in Fig. (6.7) seem to have high number of passes. . . . .	58

7.1	SALI plots of increasing $r_{\text{esc}}$ , with constant parameters $\rho = 1.2$ and $E = 1.2$ . Escaping trajectories are omitted. The regions with no escaping trajectories in Fig. (6.7) have low SALI values. . . . .	60
7.2	A plot of the percentage of ordered trajectories in a given set of parameters. The white line separates the region where black hole capture is possible (left of the line) and impossible (right of the line). . . . .	61
B.1	Sample plots of SALI and LCN for the same constants of motion $(L, E) = (1.0, 0.42)$ in the MNC system . . . . .	68

# Chapter 1

## Introduction

General relativity and astronomy are two fields of science that are very adjacent. The effects of relativity are only seen in extreme mass scales, those that are only found in our cosmos, the stage of our astronomical play. These two fields mutually grow and advance, relativity is repeatedly legitimized by astronomical observations, and in turn, it gives back by explaining and making predictions on many astronomical phenomena. Some breakthroughs that resulted from this are the perihelion precession of Mercury [1], the Eddington experiment during the 1919 solar eclipse [2, 3], the detection of gravitational waves in LIGO [4], and the Event Horizon Telescope imaging the supermassive black hole at the center of the M87 galaxy. [5].

Very recently on March 27 2024, the Event Horizon Telescope collaboration published a paper [6] analyzing data from observations of supermassive the black hole at the center of our galaxy, Sagittarius A\*. They reported that the observed light from the ring morphology surrounding the black hole has a prominent polarization structure that shows a non-negligible magnetic field affecting this ring. Similar results have been found for the observational data found from the M87 central black hole [7]. A prominent phenomenon seen in the M87 central black hole are the plasma outflows that linearly protrude from the black hole known as jets [8, 9]. These jets are composed of charged plasma ejected by the black hole at relativistic speeds [10] whose outflow is orthogonal to the accompanying accretion disk [11]. These jets are yet to be observed in Sagittarius A\*. The possible mechanisms for these highly energetic outflows are through magnetic effects of either the Blandford-Znajek process [12] or an accretion disk orbiting the black hole [13]. General-relativistic magnetohydrodynamic simulations [14] are the most successful and accurate models for these jets, though their complexity often muddles the possible qualities of the system that

may be easier to derive from simpler models.

## 1.1 Uniformly Magnetized Black Holes

One example of a simple model often used to study the behaviours of these jets is a charged particle orbiting a non-rotating Schwarzschild black hole all immersed in a uniform magnetic field, more commonly known as a *Magnetized Black Hole* (MBH) [15–21]. Black holes can be magnetized in a couple of ways - the magnetic field could be from cosmological sources [22, 23], a far away magnetar with a strong magnetic dipole [20], and most relevant to us, charged plasma from the accretion disk orbiting the black hole itself [13, 15]. Though the structure of real magnetic fields may be complex, these examples are well-approximated by an asymptotically uniform magnetic field when the source of these magnetic fields are far from the black hole [15]. Several qualities of the trajectories of singular charged particles orbiting this system have been analyzed in previous works. Specifically of note are the bounded trajectories, both equatorial and non-equatorial [17, 19], and unbounded trajectories that can escape the black hole vicinity [18, 20, 21]. In this work, a straightforward simplification will be done where we replace the Relativistic black hole with a Classical Newtonian gravitational point mass, or simply a *Magnetized Newtonian Center* (MNC). To the best of our knowledge, no study for this system has been done; this thesis aims to fill that void.

## 1.2 Escapes

The main interest for jets is the plasma outflows, so we focus on charged particle trajectories that can escape from the system. Escapes from systems have a rich background and rigorous study, but we first have to define what escape is. Escapes occur for Hamiltonian systems with sufficiently high energy, such that the phase space extends to spatial infinity. Escapes from a region of phase space can then be defined as trajectories that travel to the asymptotic region at infinity, and never return to the said region [24–26]. Some studies use a large distance from a region to quantify escape [21, 24], and some use *Lyapunov orbits*, closed orbits that exist in saddle points and unstable equilibrium points of potential energies as a border for escape, i.e. a trajectory that passes through this orbit is automatically considered to be escaping

[27–30].

To properly characterize a trajectory in a system with escapes, there are multiple escape measures that can be used [26, 31, 32]. A common measure is the escape time, which is simply the time it takes for a trajectory from a certain initial condition to be considered escaping. Another is what we will call the escape pass [26]; Here we consider a surface and count how many times a trajectory passes through this surface until it escapes. In previous studies, some authors simply use escape pass as the escape time itself [31, 32]. Due to the existence of multiple locations of escapes in the systems to be discussed, escape basins, where trajectories end up after escape [21, 33, 34], will also be studied.

### 1.3 Chaos

A prominent feature found in many systems, and in both MBH and MNC systems, is *chaos*. The most common definition of chaos is extreme sensitivity to initial conditions [26, 35–38]. What makes chaos interesting, is that trajectories are still deterministic, but due to the sensitivity, small perturbations of initial conditions will produce wildly different outcomes, which makes these systems practically and realistically unpredictable. Because of this sensitivity, it is important to distinguish and differentiate initial conditions that would produce chaotic and ordered trajectories, as this would allow at least some portion of the phase space to be practically predictable. There are multiple ways to characterize chaos; here, we introduce the approaches that will be used. They will be discussed in detail in later sections.

First are the *Poincaré plots*, also called *Poincaré maps* or *Poincaré surface of section* [26, 32, 35], where trajectories are mapped into a 2D plot by first choosing a region called a Poincaré surface, then, when the trajectories intersect through the surface, two components of their phase space coordinate are plotted on the Poincaré plot. Ordered and chaotic trajectories will have different topologies on the Poincaré plot. The distinction for chaos here is very visual and qualitative, and it would be very difficult to do numerics and statistics using Poincaré plots.

Second is the *Lyapunov exponent* [35, 38], which is a measure of the time evolution of the phase space distance between two nearby initial conditions. Chaotic trajectories tend to have exponentially increasing deviations, which results in a positive Lyapunov exponent. Ordered trajectories, on the other hand, have non-positive

Lyapunov exponents. It is a numerical way of distinguishing chaos, but it is slowly converging, i.e. numerical integration would take a very long time to fully distinguish chaos. This would be very time-consuming and inefficient when one wants to study the global chaotic dynamics of a system, as we would want to numerically integrate a large number of trajectories.

Third, and final, approach is the *Single Alignment Index* or *SALI* for short [35–37, 39]. It is another numerical way of distinguishing chaos, that relies on how the alignment of two deviation vectors time-evolve for ordered and chaotic trajectories. Deviation vectors of chaotic trajectories tend to align, while for ordered trajectories, the deviation vector tends to stay separated. When integrated in time, it is comparatively faster to converge than Lyapunov exponents, so it is more useful than the Lyapunov exponent for analysing global dynamics of a system.

## 1.4 Problem Statement

This thesis aims to describe and study the escape dynamics of a charged particle orbiting either the MNC (classical), or the MBH (relativistic). In detail, we describe how trajectories can escape in this system, which depends on the qualities of the systems' potential energy. Then, we determine for what parameters would escape be possible. Once these have been defined, we analyze the global qualities of escapes in the system, and how that changes when we tune the parameters. We also probe how the chaotic nature of the systems affects escape. Lastly, we study how the answers on the above questions differ for the MNC and the MBH, i.e. how does general relativity affect the escape dynamics.

# Chapter 2

## Magnetized Newtonian Center

In this chapter, the equations of motion of the magnetized Newtonian center (MNC) system will be derived and analyzed without recourse to numerical integration. We first introduce the MNC system, then derive its Hamiltonian. The Hamiltonian is then non-dimensionalized to reduce the parameters for analysis. The effective potential derived from the Hamiltonian is then analyzed, where we are able to find the stable equilibrium point, and the energy needed for the phase space to open towards the infinities along the direction of the magnetic field. The opening allows trajectories to theoretically escape from the system, hence the energy and the radius of where this opening occurs become significant parameters that dictate the conditions that allow escape. The minimum energy and escape energy allow us to reparametrize our energy for the purposes of numerics, where we find that under this reparametrized energy, the Hamiltonian and equations of motion are symmetrical under a parity transformation of the nondimensionalized angular momentum  $L$ , such that we only need to analyze trajectories for which  $L > 0$ .

### 2.1 System Set-up

We represent the system in cylindrical coordinates, which is chosen as a compromise for the radial symmetry of Newtonian gravity, and the rectilinear homogeneity of the uniform magnetic field. Fig. (2.1) shows the cylindrical coordinate representation of the system at hand, including its various parameters. We set the Newtonian point mass with mass  $M$  to be at the center  $r = 0$ , and the magnetic field  $\mathbf{B} = B\hat{\mathbf{z}}$  to be pointing along the positive  $z$  direction. The coordinates give the position of the test particle with mass  $m$  and charge  $q$ .

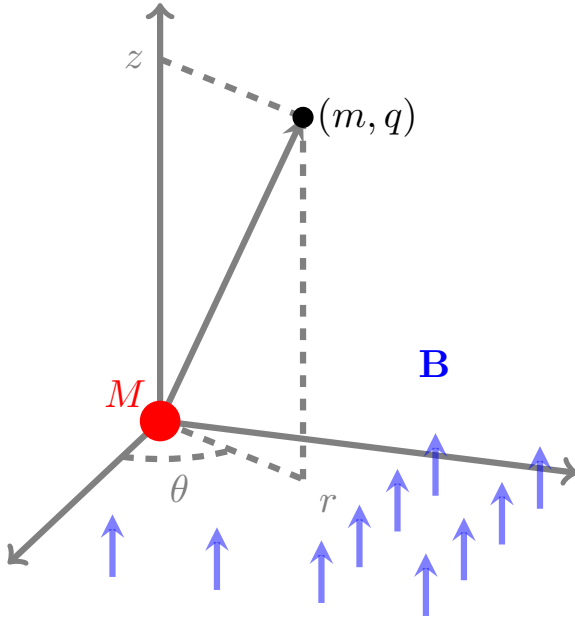


Figure 2.1: The MNC system in cylindrical coordinates  $(r, \theta, z)$ . The test particle has mass  $m$  and charge  $q$ . It is orbiting a central point mass  $M$  immersed in a uniform magnetic field  $\mathbf{B}$  along the  $+z$  direction.

## 2.2 Hamiltonian of the System

The total potential energy of the system is simply the superposition of the potential energies of the two sources (the Newtonian center and the uniform magnetic field). Using the variables defined in the previous section, the Newtonian gravitational potential energy is

$$U_{\text{grav}} = -\frac{GMm}{R}, \quad R = \sqrt{r^2 + z^2}, \quad (2.1)$$

where  $R$  is the spherical distance from the center, defined for notational convenience, and  $G$  is the Newtonian gravitational constant. The potential energy of any magnetic field is given in terms of the particle velocity  $\mathbf{v}$  and the magnetic field vector potential  $\mathbf{A}$  [40]:

$$U_{\text{mag}} = -q(\mathbf{v} \cdot \mathbf{A}) \quad (2.2)$$

For a uniform magnetic field  $\mathbf{B}$

$$\mathbf{A} = \frac{1}{2}(\mathbf{B} \times \mathbf{R}) = \frac{1}{2}Br\hat{\theta}, \quad (2.3)$$

which gives the magnetic potential energy expression

$$U_{\text{mag}} = -\frac{1}{2}qBr^2\dot{\theta}. \quad (2.4)$$

We can quickly check if Eq. (2.3) does indeed give the uniform magnetic field by taking its curl,

$$\mathbf{B} = \nabla \times \mathbf{A} = B\hat{\mathbf{z}}. \quad (2.5)$$

Now, we can derive the Lagrangian  $\mathcal{L}$  for our system in cylindrical coordinates:

$$\mathcal{L} = \frac{1}{2}m(\dot{r}^2 + r^2\dot{\theta}^2 + z^2) + \frac{1}{2}qBr^2\dot{\theta} + \frac{GMm}{R}. \quad (2.6)$$

Then, we get the canonical momenta for each coordinate of the Lagrangian:

$$\frac{\partial \mathcal{L}}{\partial \dot{r}} = p_r = m\dot{r} \quad (2.7)$$

$$\frac{\partial \mathcal{L}}{\partial \dot{\theta}} = p_\theta = mr^2\dot{\theta} + \frac{1}{2}qBr^2 \quad (2.8)$$

$$\frac{\partial \mathcal{L}}{\partial \dot{z}} = p_z = m\dot{z}. \quad (2.9)$$

Taking the Legendre transform gives the Hamiltonian  $\mathcal{H}$ :

$$\mathcal{H} = \frac{1}{2}m(\dot{r}^2 + \dot{z}^2) + \frac{1}{2m}\left(\frac{p_\theta}{r} - \frac{1}{2}qBr\right)^2 - \frac{GMm}{R}. \quad (2.10)$$

Since  $\theta$  does not appear in the Hamiltonian, its conjugate momentum must be a constant of motion, which we set to be the canonical angular momentum  $p_\theta = L$ .

Before we derive the full set of equations of motion, it is advantageous to non-dimensionalize  $\mathcal{H}$  to reduce the parameters we need to analyze. A trick we can do is to use arbitrary characteristic scales to factor out the units:

$$r \rightarrow r_c r \quad (2.11)$$

$$z \rightarrow r_c z \quad (2.12)$$

$$t \rightarrow t_c t \quad (2.13)$$

$$\mathcal{H} \rightarrow \frac{mr_c^2}{t_c^2} \mathcal{H}, \quad (2.14)$$

which gives

$$\frac{mr_c^2}{t_c^2} \mathcal{H} = \frac{1}{2} \frac{mr_c^2}{t_c^2} (\dot{r}^2 + \dot{z}^2) + \frac{1}{2m} \left( \frac{L}{r_c r} - \frac{1}{2} q B r_c r \right)^2 - \frac{GMm}{r_c R} \quad (2.15)$$

$$\mathcal{H} = \frac{1}{2} (\dot{r}^2 + \dot{z}^2) + \frac{1}{2} \left( \frac{Lt_c}{mr_c^2 r} - \frac{1}{2} \frac{q B t_c}{m} r \right)^2 - \frac{GMt_c^2}{r_c^3 R} \quad (2.16)$$

Then, we can choose the characteristic scales to make some dimensionful parameters disappear. We choose

$$t_c = \frac{m}{qB} \quad (2.17)$$

$$r_c = \sqrt[3]{GMt_c^2}, \quad (2.18)$$

which cancels out some constants and simplifies the Hamiltonian to

$$\mathcal{H} = \frac{1}{2} (\dot{r}^2 + \dot{z}^2) + \frac{1}{2} \left( \sqrt[3]{\frac{qB}{(GMm^2)^2}} \frac{L}{r} - \frac{r}{2} \right)^2 - \frac{1}{R}.$$

Lastly, we can set the remaining parameter group as

$$\sqrt[3]{\frac{qB}{(GMm^2)^2}} L \rightarrow L \quad (2.19)$$

To give the final Hamiltonian as

$$h = \mathcal{H}(r, z) = T(\dot{r}, \dot{z}) + U(r, z) \quad (2.20)$$

where

$$T(\dot{r}, \dot{z}) = \frac{1}{2} (\dot{r}^2 + \dot{z}^2) = \frac{1}{2} (p_r^2 + p_z^2) \quad (2.21)$$

is the effective kinetic energy, and

$$U(r, z) = \frac{1}{2} \left( \frac{L}{r} - \frac{r}{2} \right)^2 - \frac{1}{R} \quad (2.22)$$

is the effective potential energy. The corresponding Hamilton's equations of motion are

$$\dot{r} = p_r \quad (2.23)$$

$$\dot{\theta} = \frac{L}{r^2} - \frac{1}{2} \quad (2.24)$$

$$\dot{z} = p_z \quad (2.25)$$

$$\dot{p}_r = \frac{L^2}{r^3} - \frac{r}{4} - \frac{r}{R^3} \quad (2.26)$$

$$\dot{p}_\theta = 0 \quad (2.27)$$

$$\dot{p}_z = - \frac{z}{R^3} \quad (2.28)$$

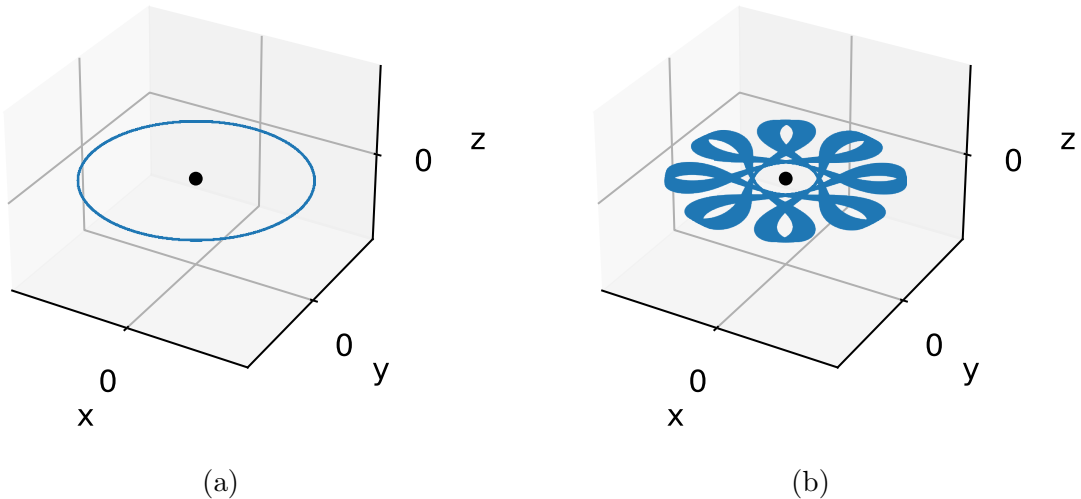
Eq. (2.27) manifests the fact that  $L$  is a constant of motion. The Hamiltonian value is also a constant of motion  $h$ , which we call the effective energy.

Overall, our system consists of two constants of motion, the angular momentum  $L$ , and energy  $h$ .  $L$  being a constant of motion goes with the fact that  $\theta$  is an ignorable coordinate, which means we have effectively reduced our system to just  $(r, z)$ . This alone is enough for us to create trajectories by numerical integration, some examples are shown in Fig. (2.1). [41] Here, we can see a rich and diverse set of trajectories,

where some are equatorial bound orbits, Figs. (2.1a, 2.1b), some are non-equatorial bound orbits, Figs. (2.1c, 2.1d), which seem to have hints of chaotic motion, and some orbits that have trajectories that seem to have helical motion similar to a cyclotronic motion that translates along  $z$ , Figs. (2.1e, 2.1f). The numerical integrator to be used for all trajectories in this thesis is the symplectic integrator with fourth-order optimal coefficients [41]. This is chosen so that the energy is generally conserved when we numerically integrate.

Due to the non-dimensionalization we have chosen, the  $L$  that appears in the Hamiltonian is effectively both a constant of motion and what we call a dimensionless group [42]. We can look at how we can tune  $L$  such that we get the limiting cases of pure gravitational orbit and pure magnetic cyclotron assuming that the dimensionful angular momentum is fixed. The transformation in Eq. (2.19) shows that a strong magnetic effect  $qB$ , corresponds to a high value of  $L$ , and a strong gravitational effect  $GMm^2$  corresponds to a low value of  $L$ . Henceforth, we shall refer to  $L \rightarrow \infty$  as the magnetic limit and  $L \rightarrow 0$  as the gravitational limit.

From [43], we can use physical values of the magnetized black hole to get a sense of the scales of the system. We use the values  $M \approx 7.96 \times 10^{36}$ m, and a range of  $B = (5.6 \times 10^{-3}, 6.4 \times 10^{-2})$ T. For an electron, we get  $t_c = (8.9 \times 10^{-11}, 1.0 \times 10^{-9})$ s and  $r_c = (1.6 \times 10^2, 8.2 \times 10^2)$ m. For a proton, we get  $t_c = (1.6 \times 10^{-7}, 1.9 \times 10^{-6})$ s and  $r_c = (2.4 \times 10^4, 1.2 \times 10^5)$ m. We see here that the time scales are around the nanosecond scale, which would mean that the events in this dimensionless system happen for a very short amount of time.



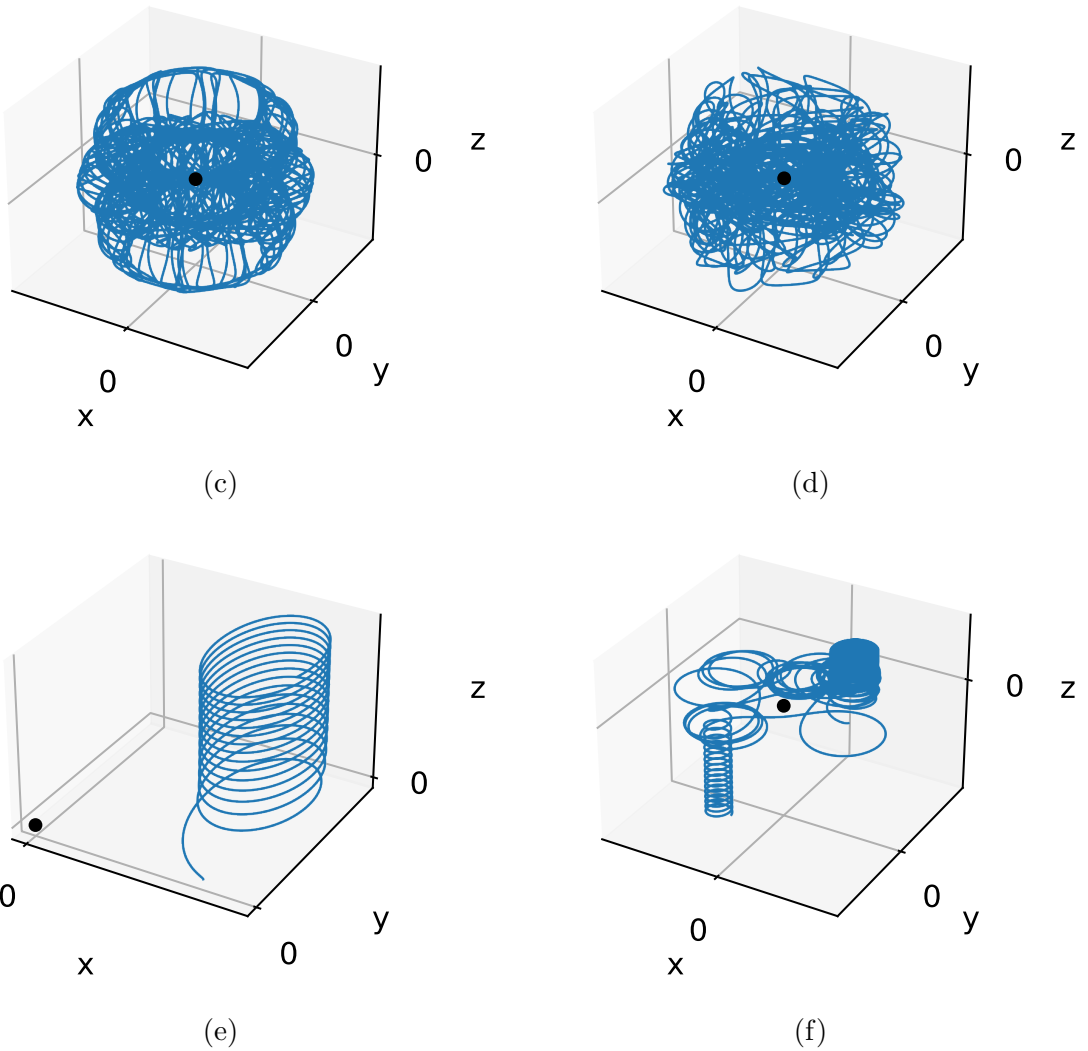


Figure 2.1: Sample 3d trajectories of particles in the MNC, where the origin is marked by a black dot.

## 2.3 Potential Analysis

In this section, we analyze the effective potential of the system. We first derive the minimum, of the effective potential, which is a single point along the equatorial plane. This implies that every trajectory in the phase space is attracted towards this one point. We then introduce zero velocity curves, which is simply the boundary of the phase space that separates kinematically allowed from kinematically forbidden regions. Kinematically forbidden simply means that the potential energy is higher than the total energy, which is considered impossible for kinematic purposes. This allows us to study the nature of our phase space for differing values of the constants

of motion. We find that for low energies, the zero velocity curves are generally closed, corresponding to a compact phase space. But for sufficiently high energies, the zero velocity curves open towards the infinities of  $z$ , allowing trajectories to go infinitely far away from the Newtonian center along the direction of the magnetic field.

### 2.3.1 Equilibrium Points

To find equilibrium points in this system, we simply find where the gradient of the effective potential  $U$  is equal to 0. In other words, where the effective force is 0.

$$r_{\text{eq}}^4 + 4r_{\text{eq}} - 4L^2 = 0 \quad (2.29)$$

$$U_{\text{eq}} = \frac{1}{2} \left( \frac{L}{r_{\text{eq}}} - \frac{r_{\text{eq}}}{2} \right)^2 - \frac{1}{r_{\text{eq}}} \quad (2.30)$$

We find that there is only a single equilibrium point at  $(r, z) = (r_{\text{eq}}, 0)$ , which can be obtained numerically by finding the root of Eq. (2.29). The equation only has a single positive real root. We can then get the minimum potential energy  $U_{\text{eq}}$  by inputting the equilibrium point to Eq. (2.22) to get Eq. (2.30).

The equilibrium point represents the circular orbit of this system as  $r$  and  $z$  stays constant, but not  $\theta$ . A sample circular orbit is in Fig. (2.1a). Because there is only one equilibrium point, the potential energy is strictly decreasing towards this point. In other words, the effective force is always attractive towards the equilibrium point, which makes it more interesting that escaping trajectories will be eventually shown to be possible.

### 2.3.2 Zero Velocity Curves

If we set the kinetic energy to 0, i.e.  $h = U$ , we get the equation of an implicit curve, aptly called a *Zero Velocity Curve* (ZVC) [25, 32]. A ZVC is just the equipotential curve of a given energy, but we choose this specific nomenclature to emphasize that particles or trajectories that are on this curve have zero velocities in  $r$  and  $z$ . The purpose is for defining escaping trajectories later on. Note that the curves occur for zero  $\dot{r}$  and  $\dot{z}$ , not necessarily a zero total velocity, meaning, we can still have angular velocities, it is just ignored since we have reduced the system to  $(r, z)$ . A sample set of ZVC's are shown in Fig. (2.2).

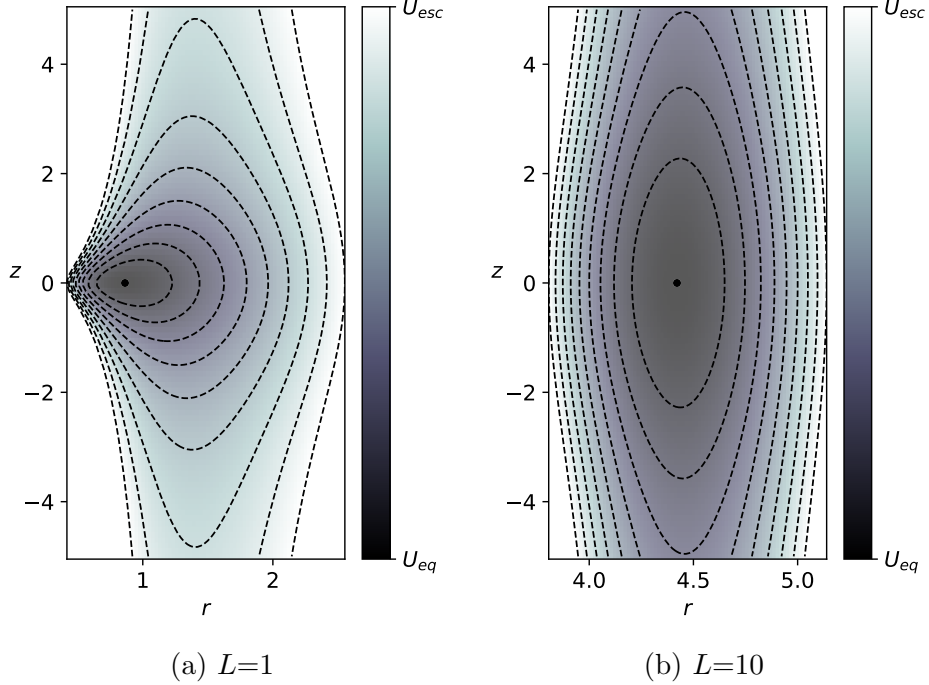


Figure 2.2: Each dashed curve represents a zero velocity curve of the potential for the given  $L$  and  $U$ . The sole minimum of the system is shown with a black dot, where the ZVC converges as we reduce the energy to  $U_{\text{eq}}$ . Darker colors mean lower magnitudes of the effective potential energy. ZVC's for energies higher than  $U_{\text{esc}}$  are omitted.

### 2.3.3 Open Zero Velocity Curves

We show that the ZVC's can open to infinity along  $z$ , this gives us where our trajectories can escape to. If we take the limit of the energy as  $z \rightarrow \infty$ , we get

$$U_{\text{esc}} = \frac{1}{2} \left( \frac{L}{r_{\text{esc}}} - \frac{r_{\text{esc}}}{2} \right)^2. \quad (2.31)$$

We preemptively call this as the energy of escape  $U_{\text{esc}}$ - as we will show later on, this gives us the threshold energy in which particles in this system can escape. We can then rearrange Eq. (2.31) to get  $r_{\text{esc}}$ .

$$0 = r_{\text{esc}}^4 - 4(2U_{\text{esc}} + L)r_{\text{esc}}^2 + 4L^2 \quad (2.32)$$

$$r_{\text{esc},\pm} = \sqrt{2(2U_{\text{esc}} + L) \pm 4\sqrt{(U_{\text{esc}} + L)U_{\text{esc}}}} \quad (2.33)$$

We only get the positive root of  $r_{\text{esc}}$  since  $r \in [0, +\infty)$ . What  $r_{\text{esc}}$  gives is where the ZVC asymptotically approaches as  $z \rightarrow \infty$ , hence we can call  $r_{\text{esc}}$  as the *asymptotes of escape* (AoE). There are two parameters that affect the number of real roots of  $r_{\text{esc}}$ , the discriminant  $(U_{\text{esc}} + L)U_{\text{esc}}$  and the vertex term  $2U_{\text{esc}} + L$ .

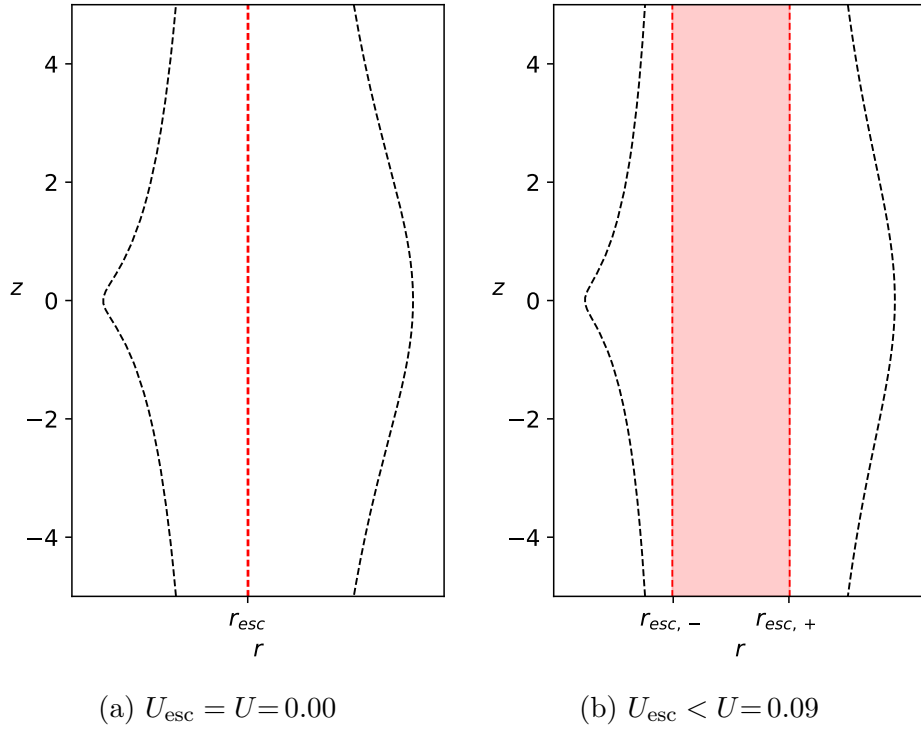


Figure 2.3: Zero Velocity Curves (black) of the potential given  $L = 1$  with energies equal to or greater than  $U_{\text{esc}}$  in Figs. (2.3a) and (2.3b) respectively. The asymptotes of escape are shown as red dashed lines. Higher energies widens this escape channel.

Let us first look at a case of a singular real root of  $r_{\text{esc}}$ , which we get if the discriminant is 0 and the vertex term is positive. Then there are two cases for a single root depending on the value of the parameter  $L$ . If  $L > 0$ , the only way for a single root to exist is if  $U_{\text{esc}} = 0$  because it gives a zero discriminant and a positive vertex term equal to  $L$ . If  $L < 0$ ,  $U_{\text{esc}} = 0$  cannot be a solution as the vertex term will be negative, thus,  $U_{\text{esc}} = -L$  (a positive number) gives the real solution. These conditions can be shortened to a single term as,

$$U_{\text{esc, min}} = \frac{1}{2}(|L| - L) = \begin{cases} 0 & , L > 0 \\ -L & , L < 0 \end{cases}. \quad (2.34)$$

Where  $U_{\text{esc, min}}$  is the minimum energy at which the ZVC first opens towards infinity at a single point. If we input this to Eq. (2.33), we get the position where the ZVC first opens to infinity, or simply the escape channel radius,

$$r_{\text{esc}} = \sqrt{2|L|}. \quad (2.35)$$

Energies greater than  $U_{\text{esc,min}}$  have two real roots, so the ZVC opens up into an escape channel as shown in Fig. (2.3).

## 2.4 Reparametrization of Energy

We can reparametrize our energy by introducing a new parameter  $E$ , such that the minimum energy for a given  $L$  is  $E = 0$ , and the escaping energy is at  $E = 1$ . We use Eqs. (2.30) and (2.34) to create a linear transformation.

$$h = U_{eq} + E(U_{\text{esc,min}} - U_{eq}) \quad (2.36)$$

Inputting Eqs. (2.30) and (2.35) to the right hand side of this equation, then simplifying gives

$$h = \frac{1}{2} \left( \frac{L}{r_{eq}} - \frac{r_{eq}}{2} \right)^2 - \frac{1}{r_{eq}} + E \left( \frac{1}{2}|L| - \frac{1}{2} \left( \frac{L^2}{r_{eq}^2} + \frac{r_{eq}^2}{4} \right) + \frac{1}{r_{eq}} \right) \quad (2.37)$$

Note that all quantities here are constants. Equating this to the Hamiltonian in Eq. (2.21), then cancelling out some terms gives

$$\begin{aligned} & \frac{1}{2} \left( \frac{L}{r_{eq}} - \frac{r_{eq}}{2} \right)^2 - \frac{1}{r_{eq}} + E \left( \frac{1}{2}|L| - \frac{1}{2} \left( \frac{L^2}{r_{eq}^2} + \frac{r_{eq}^2}{4} \right) + \frac{1}{r_{eq}} \right) \\ &= \frac{1}{2} (p_r^2 + p_z^2) + \frac{1}{2} \left( \frac{L}{r} - \frac{r}{2} \right)^2 - \frac{1}{R} \end{aligned} \quad (2.38)$$

$$\begin{aligned} & \frac{1}{2} \left( \frac{L^2}{r_{eq}^2} + \frac{r_{eq}^2}{4} \right) - \frac{1}{r_{eq}} + E \left( \frac{1}{2}|L| - \frac{1}{2} \left( \frac{L^2}{r_{eq}^2} + \frac{r_{eq}^2}{4} \right) + \frac{1}{r_{eq}} \right) \\ &= \frac{1}{2} (p_r^2 + p_z^2) + \frac{1}{2} \left( \frac{L^2}{r^2} + \frac{r^2}{4} \right) - \frac{1}{R}. \end{aligned} \quad (2.39)$$

Eq. (2.39) is essentially our energy equation, but with the reparametrized energy  $E$ .

Due to the length and complexity of this equation, this is not to be used analytically, only computationally, i.e., we pick energies in terms of  $E$ , and initial conditions  $p_r$ ,  $r$ , and  $z$ , then obtain  $p_z$  from Eq. (2.39). But we can still obtain a notable quality of the reparametrization; there is no more dependence on the sign of  $L$ , which implies a symmetry in the system when  $E$  is used as the energy. Meaning that if we chose the exact same initial conditions except for  $p_z$ , for example, and get the  $p_z$  value from the energy  $E$  using Eq. (2.39), we get that for any value of  $E$ , we get the same initial conditions for both  $L$  and  $-L$ . Also, our equations of motion along  $r$  and  $z$  (Eqs. (2.23) to (2.28)) do not depend on the sign of  $L$ , so overall, the trajectories for both  $L$  and  $-L$  are also similar, given that the initial conditions are the same. This allows us to reduce the needed range of analysis to just  $L \geq 0$ . All in all, given the reparametrized energy  $E$ , our system and its trajectories are symmetrical under a parity transformation of  $L$ .

# Chapter 3

## Escapes from a Magnetized Newtonian Center

In the previous chapter, we found that a certain energy threshold makes our Hamiltonian system open, i.e. allowing trajectories to go to infinity along  $z$ . For open Hamiltonian systems, it is interesting to analyze escaping trajectories. These are trajectories that goes toward infinity and will never return to a region of interest. A more robust definition would describe them to be those that pass through unstable periodic orbits known as Lyapunov orbits away from the region [25, 28, 32]. These Lyapunov orbits are the boundaries that separate a region of interest with stable minima, and escaping regions for which the effective force, the negative gradient of the effective potential, is repulsive from the region. This ensures that trajectories that pass through the Lyapunov orbits will continue moving away from the region of interest, thus escape.

Numerical studies of escapes have been done for many systems. Some of them focus on escape time [24, 25, 44], which is simply the time it takes for a trajectory to cross the Lyapunov orbit from a certain initial condition. One can show this using two-dimensional heatmaps, in which the color is the escape time, and the points are certain initial conditons. Using these escape times, we can also plot their distribution, showing a general sense of when trajectories escape for sets of initial conditions. Other authors have looked at the escape pass [26, 32]. For Hamiltonians with stable potential energy regions that have trajectories that recur, there is a point the system is attracted towards i.e. a potential energy minimum. Some examples are the equatorial plane of the Henon-Heiles system [25], of the MBH [17], and of the MNC. Sometimes, escape passes are used as the escape time itself [26], but here we will make a distinction

between these two quantities

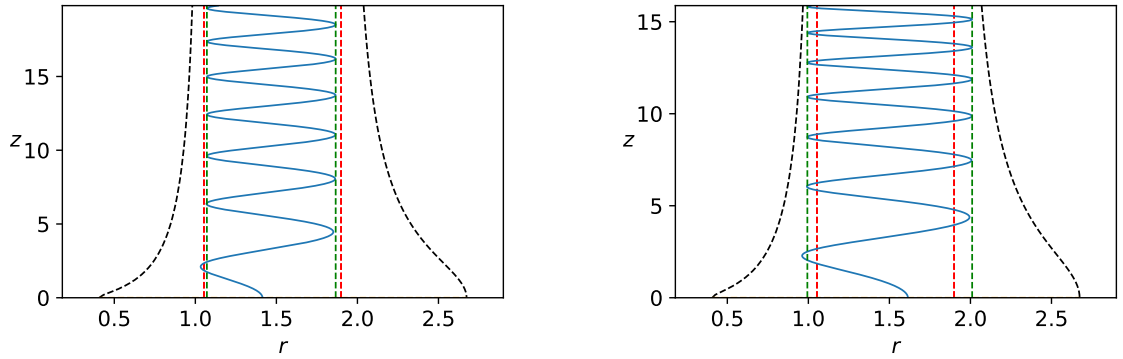
Because of the nature of the system, no Lyapunov orbits exists. This is because the potential energy of the system has only one equilibrium point, which is stable. This implies that the effective force on the system is always attractive towards the equilibrium point; no region with repulsive effective force exists. This would make the aforementioned definition of escape unusable in our case. To proceed, we shall provide a new definition of escape that is both physically well-motivated and efficient to check numerically. It will be constructed from some properties of our system. This new definition will be used in conjunction with the different escape quantities to analyze the MNC system. This would allow us to emphasize some special kinds of trajectories found in this system that is connected to the idea of escape.

### 3.1 New Definition of Escape

The potential energy of our system is strictly decreasing everywhere towards the minima on the equatorial plane, so there are no Lyapunov orbits. Hence we cannot use the typical definition of escape. Papers that have discussed escapes on the uniformly magnetized black hole case [20, 21] classified high  $|z|$  values as escaping with a certain threshold, or are outrightly vague about how escape is defined. We could use the same definition of escape for the MNC case, but the arbitrariness of choosing the threshold  $|z|$  makes some results questionable. Also, it was not shown if these trajectories will continue moving away from the center; as we will see later on, the effective force on the MBH case is also attractive. Some trajectories that are deemed escaping in that definition may not be truly escaping. Hence, we propose a more robust and exact definition of escape for this system.

There are two facts about this system that we can use as a basis to construct the escape definition. First, trajectories are oscillatory on  $r$  for far enough trajectories; and second, open Zero Velocity Curves are asymptotic along  $r$ . If a trajectory oscillates within the two asymptotes, it will never touch the ZVC, meaning, its non-angular velocity will never become 0 and collapse back towards  $z = 0$  (as the effective force is attractive to  $z = 0$ ). This is illustrated in Fig. (3.1).

So with this, we can define escapes in the MNC system as trajectories moving away from the equatorial plane with amplitudes of oscillation that are within the asymptotes of escape. A simpler way to define escape is that if the trajectory's



(a) Sample escaping trajectory, as the amplitudes of oscillation are within the asymptotes of escape

(b) Sample inescaping trajectory, as the amplitudes of oscillation are outside the asymptotes of escape

Figure 3.1: Sample trajectories that shows the difference between an escaping and an inescaping trajectory. Escape depends on whether or not the amplitudes of the cyclotronic oscillation (Green) are within the boundaries of the asymptotes of escape (Red). The escaping trajectory in 3d is shown in Fig. (2.1e). The inescaping trajectory in 3d is in Fig. (2.1f), it is shown there that it eventually escapes, not just in this specific launch.

oscillation “fits” inside the escape channel.

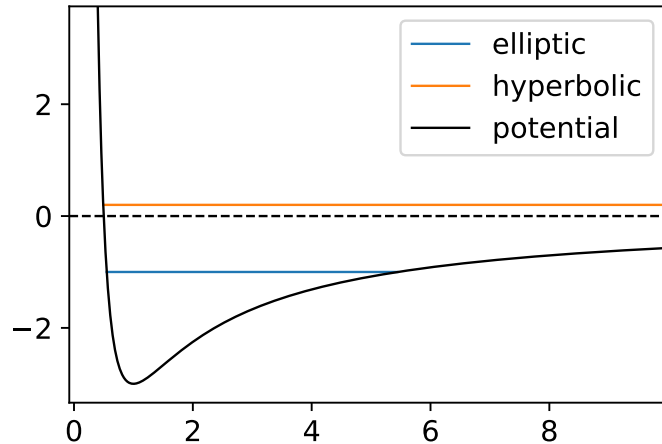


Figure 3.2: Newtonian gravity potential energy and specific trajectories, which are a bound elliptic orbit and an unbound escaping elliptic orbit.

The pure Newtonian gravity analog of escaping and inescaping trajectories are that the escaping trajectories are hyperbolic orbits which occurs for  $E > 0$ , and the inescaping ones are the elliptical orbits which occurs for  $E < 0$ . To elaborate on this, let us look at the potential of pure Newtonian gravity on Fig. (3.2). An MNC trajectory “touching the ZVC” is the same as saying that the potential and

total energy are equal, which in turn means that the non-angular velocity is 0. A pure Newtonian gravity trajectory has its own “ZVC”, which are two points  $R_{\min}$  and  $R_{\max}$  where the radial velocity is 0. The elliptical orbit has an upper bound for the ZVC  $R_{\max}$ , so we know that it will not continue moving away from the center, thus inescaping. The hyperbolic orbit on the other hand, has no upper bound, which means that its radial velocity will never be zero, so it will continue moving away from the center, thus escaping. So in general, the condition for escape in the pure Newtonian gravitational potential is  $E < 0$  for inescaping, and  $E \geq 0$  for escaping.

Algorithmically, we shall define escape as follows:

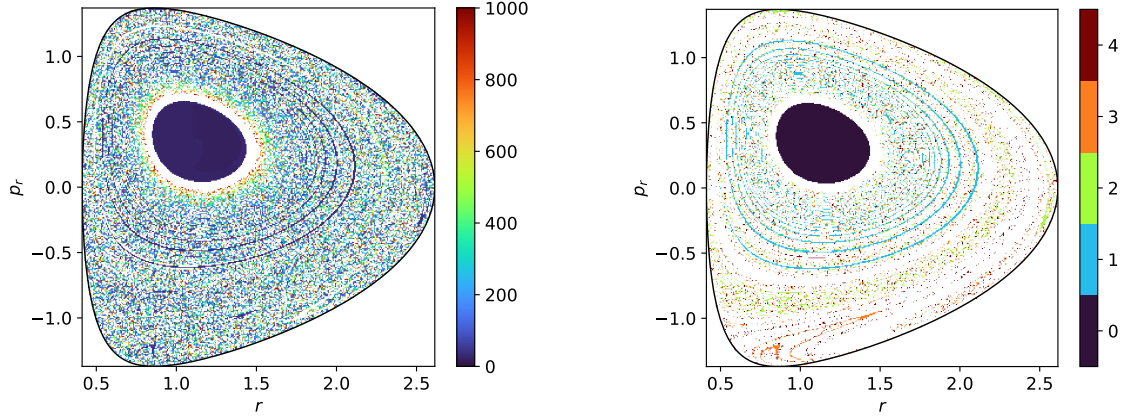
1. We record the last 4 maxima and 4 minima (or amplitudes) on each side of the trajectory along  $r$ . A point in the trajectory is computationally considered as an extrema if  $\dot{r}_n \dot{r}_{n+1} < 0$ .
2. Check if the amplitudes are within the boundaries of the asymptotes of escape, i.e.,  $r_{\text{asym},-} < r_{\min}$  and  $r_{\max} < r_{\text{asym},+}$  for all recorded oscillation amplitudes.
3. If yes, the trajectory is deemed as escaping. If no, continue integrating until a maximum time.

The number of extrema recorded is arbitrary, higher numbers lead to higher accuracy in defining a trajectory as escaping, but more computational power and time is required. The calculated escape time will increase as more extrema are recorded, but this only shifts all escape times by an approximately even amount. This does not matter much for our analysis as what is relevant are the relative escape times of the ensemble.

## 3.2 Escape Time and Escape Pass

Now that we have well-defined escapes for the MNC system, we can start analyzing escaping trajectories. What we will do first is calculate the time it takes for trajectories to escape using our definition. We then plot the escape times for different initial conditions. We choose trajectories that originate from the equatorial plane  $z = 0$  with initial values  $r_0$  and  $p_{r0}$  chosen as the points of the plot. The test charge is then launched upwards with  $p_{z0} \geq 0$ , such that it has the energy  $h$ . So, we have a

2D heatmap plot of escape times along  $r$  and  $p_r$ , for a given pair of  $L$  and  $h$  values. We originate the trajectories at  $z = 0$  so that we can capture as many trajectories as possible. This is because any trajectory in the system is attracted towards the equatorial plane, so all off-equatorial initial conditions that are not directly escaping at some point will return to this plane, and the exact point where it returns to can be treated as an initial condition of another trajectory that already exists in the plot. Lastly, we can derive  $p_{z0}$  from the Hamiltonian, since we are given all other needed initial conditions to obtain this value. We also just take the positive value, as the symmetry of the system along  $z = 0$  means just changing the sign of  $p_{z0}$  will just flip the overall trajectory. Fig. (3.3a) shows a sample of this escape time plot. We also calculate the number of times a trajectory crosses the equatorial plane  $z = 0$ , which we call the escape pass. Note that odd number of escape passes are trajectories that escape to  $z \rightarrow +\infty$ , and even number of escape passes are trajectories that escape to  $z \rightarrow -\infty$ . Fig. (3.3b) shows the corresponding escape pass plot.



(a) Sample escape time plot. White points imply that the trajectory has not escaped within  $t = 1000$ .

(b) Sample escape pass plot, showing only up to 4 passes. Higher passes are omitted for clarity

Figure 3.3: Sample escape plots for constants of motion  $E = 1.05$ ,  $L = 1$ , and maximum integration time  $t = 1,000$ . A black line border around the plot bounds all trajectories, everything outside it is kinematically forbidden (negative kinetic energy).

In Fig. (3.3a) we see an ordered region with relatively low escape times shown in a solid blue color surrounded by a white band. These trajectories have relatively small escape times, and as shown by Fig. (3.3b), do not pass through the equatorial plane even once. They are trajectories that directly escape without passing through the equatorial plane, or more succinctly, the 0-pass trajectories for the given constants of

motion.

Surrounding the 0-pass region in Fig. (3.3a) is a white band, and further out, is a gradient of escape times that increases as it approaches the 0-pass region. This means that trajectories that are 1-pass or higher whose initial conditions are approaching those of the 0-pass ones have increasing escape times. This is shown in Fig. (3.4a), where we increased the integration time to  $t = 10,000$  and zoomed into the boundary of the 0-pass region and the gradient. The plot shows that trajectories with escape times lower than those of the permeating gradient do not exist, e.g. no blue dots exist in the red-green region, but there are plenty of red-green dots on the blue region. This is also shown by the existence of the white band, where no trajectories exist that escape before  $t = 10,000$ . We might think that low escape times should exist in these higher escape time regions due to the chaotic nature of the trajectories. This shows that what increases as the initial condition approaches the 0-pass region is the minimum escape time to be exact. Using the pure Newtonian gravity analog, these increasing gradient of escape times is similar to how for elliptic inescaping orbits, as the energy approaches  $E = 0$ , the orbits enlarges. Meaning, it would take a longer amount of time for it to return to the perihelion, the closest point of the orbit to the center.

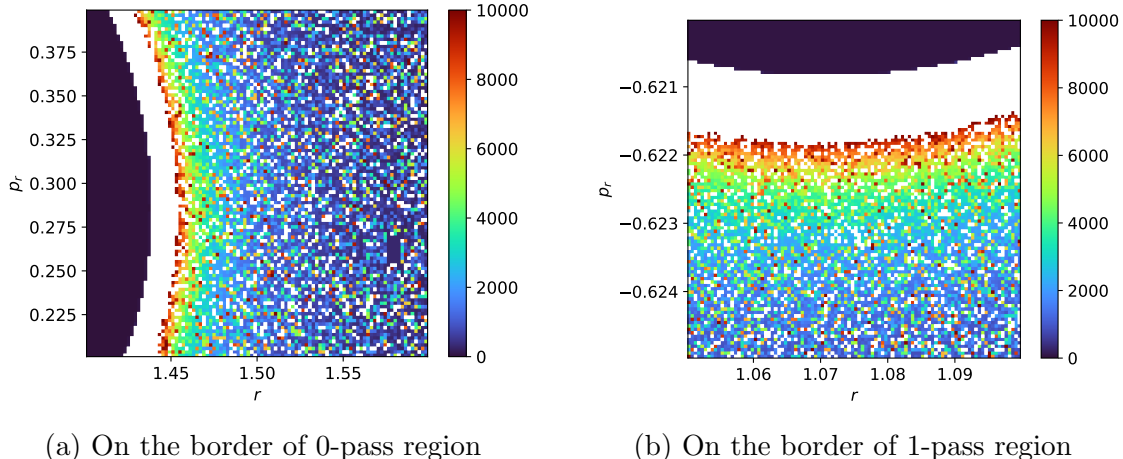


Figure 3.4: Escape plot zooming in on the border of ordered trajectories, showing the gradient of escape times that increases as the initial conditions approach the ordered region. Maximum integration time for this plot is  $t = 10,000$  to further probe into these asymptotic escape times

For trajectories with higher passes, specifically for those with 1-3 passes through  $z = 0$ , there are also ordered sets of trajectories that forms a solid shape similar to the

0-pass region. As seen in Fig. (3.3b), there is a spiral-like pattern for 1-pass initial conditions, that slowly becomes chaotic as it spirals into the 0-pass region, and small blotches of order in a generally chaotic set for 2-3 passes. If we zoom in near the borders of these ordered sets, we see a similar gradient as the trajectories approach these solid regions as seen in Fig. (3.4b).

So, in general, there are ordered sets of trajectories that are littered all around the phase space, and surrounding those are chaotic trajectories with a gradient of minimum escape times that increases as the initial conditions approach the ordered set. The reason for this gradient of minimum escape times is the trajectories with initial conditions close to the 0-pass ones, will look similar to these 0-pass trajectories, but will have its amplitude of oscillation be slightly outside the asymptotes of escape. Because they are close to the asymptotes of escape, these trajectories will take some time before it touches the ZVC and collapse back to the equator. This can be seen in Fig. (3.5), where we plot  $z$  value where the trajectories that are not directly escaping touch the ZVC. This  $z$  value is also the position of the turning point before the trajectory collapses back towards the equatorial plane  $z = 0$ . We see that there is a gradient in the  $z$  position of the turning point as these initial conditions approach the 0-pass region.

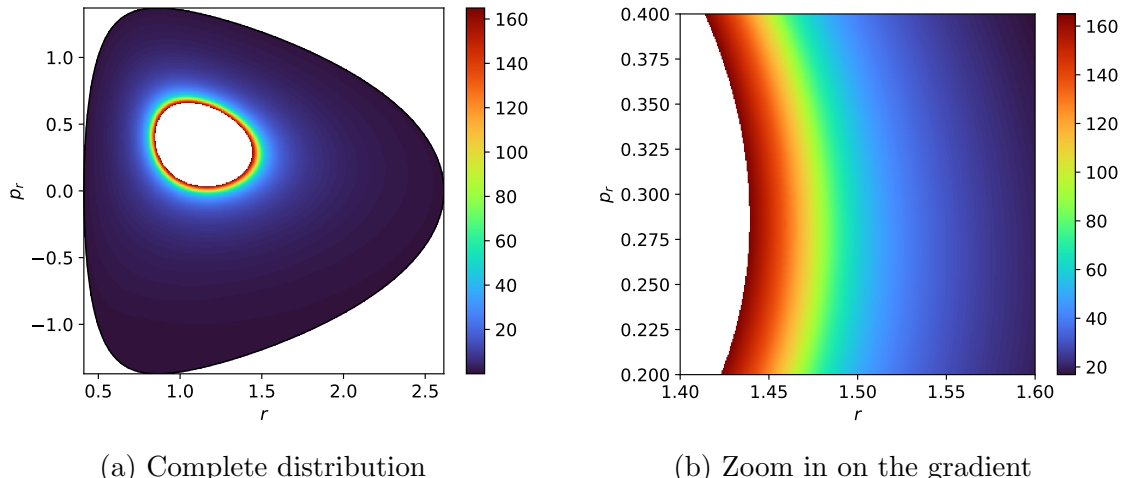


Figure 3.5: Heatmap of the turning point  $z$  value corresponding to initial conditions of trajectories that do not directly escape and eventually collapse back towards the equatorial plane  $z = 0$ .

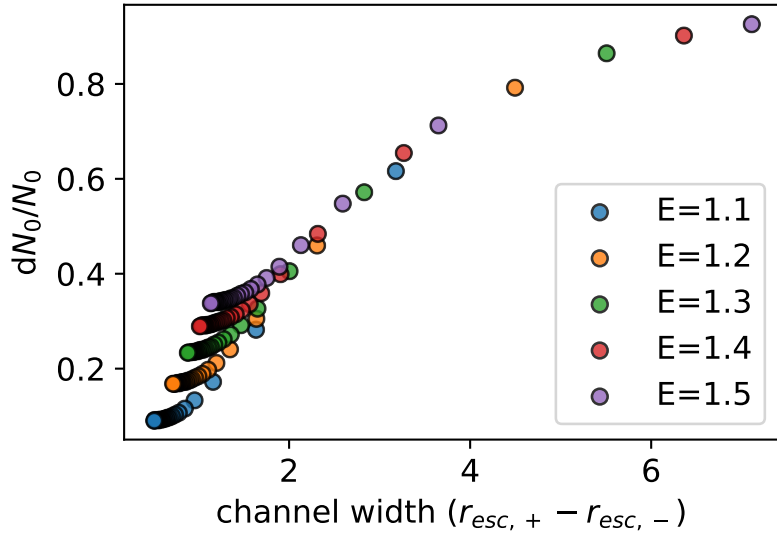


Figure 3.6: Proportion of 0-pass escaping trajectories to the total number of trajectories vs escape channel width. Each point represents a pair of constants of motion  $E$  and  $L$ .

### 3.3 0-pass Trajectories

We can also numerically analyze the 0-pass trajectories by taking their proportion out of the total set of trajectories integrated over a given set of constants of motion. Here we postulate that the proportion of 0-pass trajectories depends on the width of the escape channel  $r_{\text{esc},+} - r_{\text{esc},-}$  from Eq. (2.33), simply because larger escape channel widths would imply more trajectories can escape. The escape times and passes are calculated for a set of constants of motion  $L \in [0.2, 5]$  and  $E \in [1.1, 1.5]$ . Then, for each set of constants of motion, we calculated the proportion of initial conditions of 0-pass trajectories, to the total number of kinematically allowed initial conditions. The scatter plot of this is shown in Fig. (3.6), where each point represents a set of constants of motion.

As postulated, we find that the width of the escape channel directly correlates with the proportion of 0-pass escaping trajectories. Note that the correlation is not linear because the proportion of escaping trajectories has a maximum value of 1. It can also be seen from the plot that more energetic trajectories directly escape for smaller escape channel widths. But for larger escape channel widths, the probability of escape seems to asymptotically approach a curve. All in all, this means that higher energy allows more trajectories to directly escape, which is significant mostly for lower

channel widths, but as the channel width increase, energy seems to matter less (aside from the fact that channel width directly depends on the energy).

### 3.4 Trapped Orbits

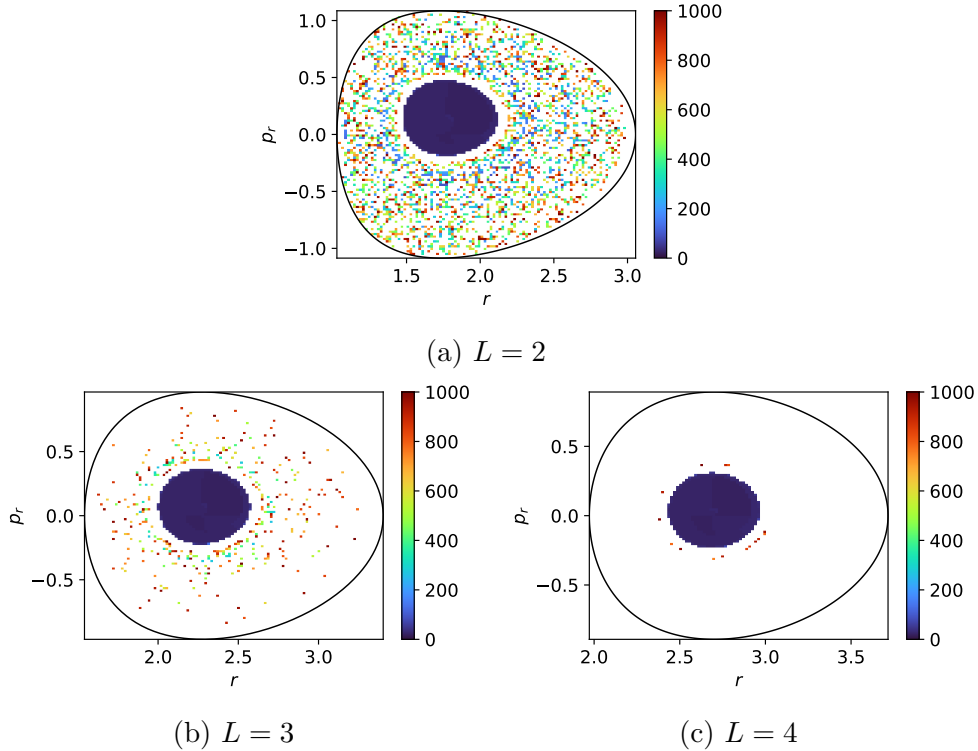


Figure 3.7: Escape time plots for increasing values of  $L$ , with a constant energy  $E = 1.1$ . Increasing  $L$  seems to decrease the number of escaping trajectories.

When we tune the values of  $L$  and  $E$ , we can see how the escape plots transform, this is demonstrated in Fig. (3.7). One peculiar quality of the escape plot shown is that the number of trajectories that escape by  $t = 1,000$  seem to decrease as  $L$  increases, though the 0-pass region barely changes relative size nor shape. We might be tempted to say that this is just due to the finite integration time, and that if we increase the integration time, these trajectories might finally escape. But we can show through the corresponding escape pass plots in Fig. (3.8), that it is not as simple as that. We see certain regions in the escape pass plots that have relatively high number of passes in red, seem to correspond to the regions in Fig. (3.7) with no escapes. This implies that inescaping trajectories correspond to high number of passes through the equatorial plane. There seems to be something that “traps” these orbits to stay near

the equatorial plane. The big question becomes what is the nature of these trapped orbits, and for what exact constants of motion these trapped orbits occur in. This is to be answered in the next chapter.

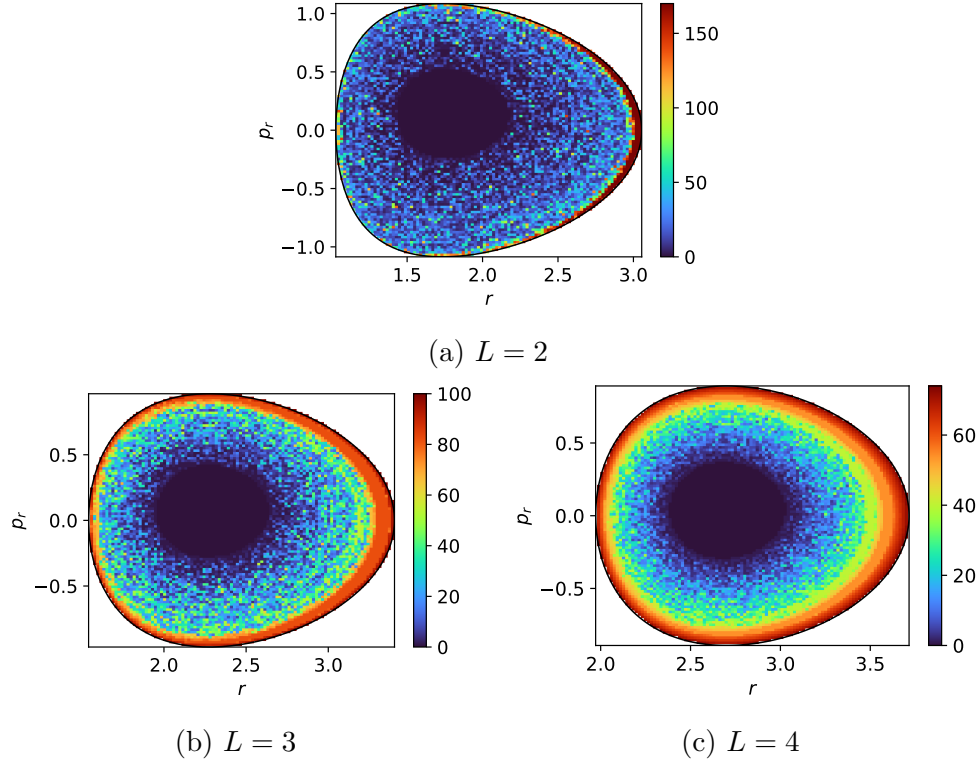


Figure 3.8: Escape pass plots for increasing values of  $L$ , with a constant energy  $E = 1.1$ . The regions with no escaping trajectories in Fig. (3.7) seem to have high number of passes.

# Chapter 4

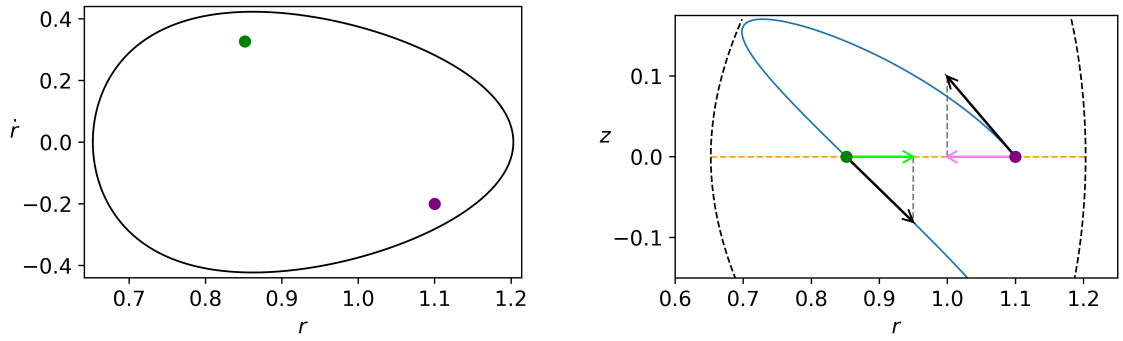
## Chaos on a Magnetized Newtonian Center

To elucidate these trapped orbits, we ought to discuss one quality of the system we have yet to elaborate on, which is chaos. Chaos is classically defined as extreme sensitivity to initial conditions [26, 35–38]. Chaotic systems are still deterministic, which means their equations of motion are fully known and do not have any stochastic entities, but the sensitivity to initial conditions makes trajectories practically unpredictable, which increases the difficulty and complexity of analysing chaotic systems. The system at hand contains chaotic trajectories, and to better probe into this nature, we will use two methods of chaos indicators. First, are Poincaré plots, which are very qualitative and rely on visual plots to loosely pick off where chaotic trajectories are. Second is the Single Alignment Index, or SALI for short, which is a scalar value for a given trajectory, that converges to different values depending on the sensitivity of the initial conditions. This allows a more quantitative measure for chaos that is more useful for numerics.

Using the SALI method, we will define a new quantity for a given set of constants of motion ( $L, E$ ), which is the proportion of ordered orbits. Using this quantity, the nature of these trapped orbits will be elucidated. How chaotic these trapped orbits are is the key to explaining their existence. We will also see at what parameters these trapped orbits occur.

### 4.1 Poincaré Plots

Poincaré plots are two-dimensional projections of ensembles of phase space trajectories [26, 32, 35]. They are useful for studies on chaos because ordered and chaotic



(a) Poincaré plot for the trajectory shown in (b). The black curve is the trajectory of the equatorial orbit that encloses the kinematically permissible phase space.

(b) Trajectory (blue curve) with the Poincaré section (orange), compounded with black arrows that shows the momentum with the  $r$  component of the momentum projected onto the Poincaré section. The trajectory is bounded by the black dashed ZVC.

Figure 4.1: A sample Poincaré plot (a) with its corresponding trajectory plot (b).

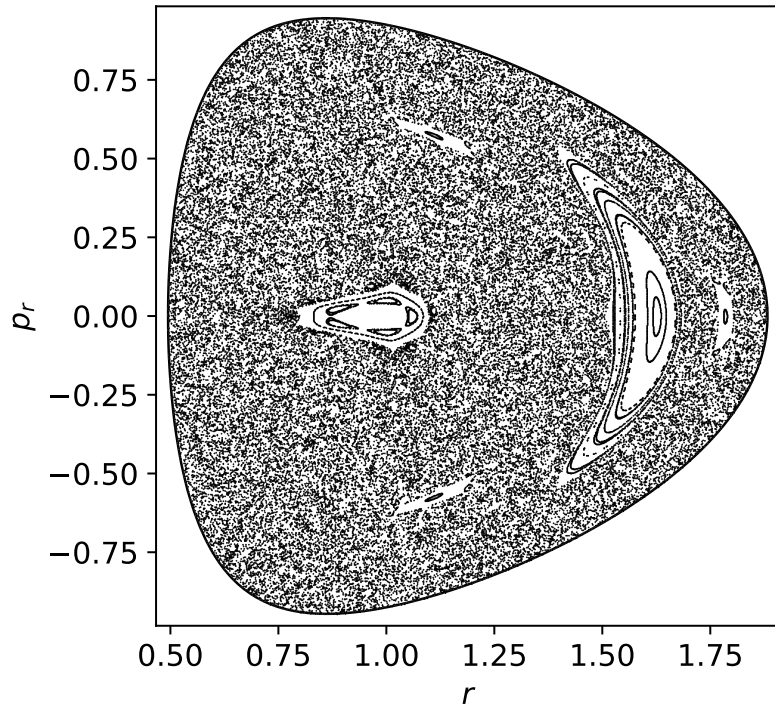
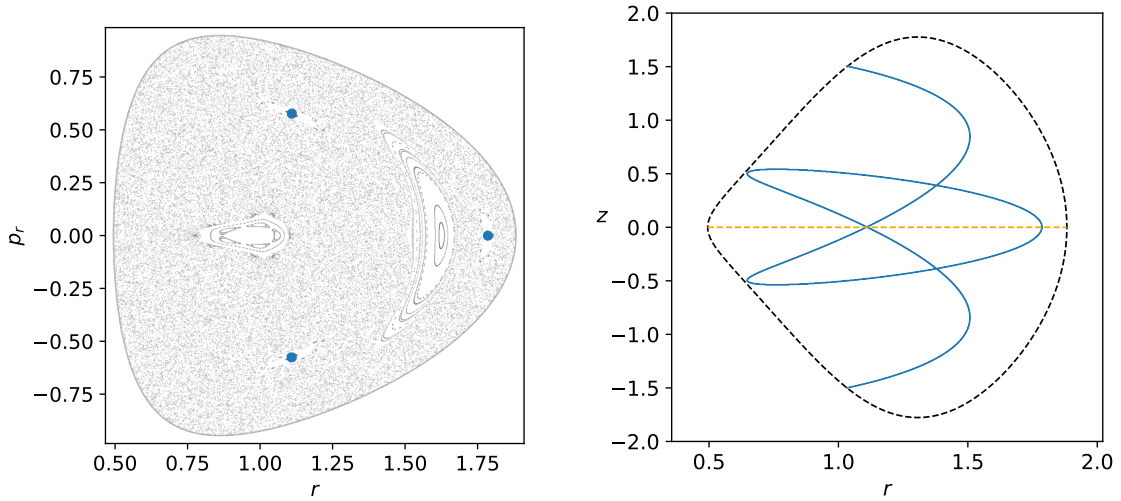


Figure 4.2: A sample Poincaré plot for  $E = 1.5$  and  $L = 1$  with an ensemble of 20 trajectories time integrated until each trajectory generated 200 Poincaré points. Different regions of display different topologies that correspond to ordered and chaotic trajectories, i.e., the region with closed curves are generally ordered periodic and quasi-periodic trajectories, and the region with noise-like structure are chaotic trajectories.

trajectories have different topologies on the Poincaré plots. Poincaré plots can be generated first by choosing a Poincaré surface (here we choose  $z = 0$ ), then every time an integrated trajectory passes through the surface, its coordinate is plotted in the Poincaré plot. Fig. (4.1) compares the actual trajectory of a particle to its corresponding Poincaré plot.

Fig. (4.2) shows an example Poincaré plot along  $(r, p_r)$ , where we plot an ensemble of 20 trajectories time integrated until each trajectory generated 200 Poincaré points, for a total of 4,000 points. We see 2 distinct regions in the Poincaré plot formed from the Poincaré points, which are the resonant islands, represented by these dotted and closed curves, and the chaotic sea, where we see noise-like scattering of the Poincaré points [26]. These regions represent trajectories that are ordered and chaotic respectively. To see why, let us analyze specific trajectories and their corresponding Poincaré points.



(a) Poincaré points of the trajectory are highlighted in blue. There are 3 points, which corresponds to the 3 passes of the trajectory at  $z = 0$ .

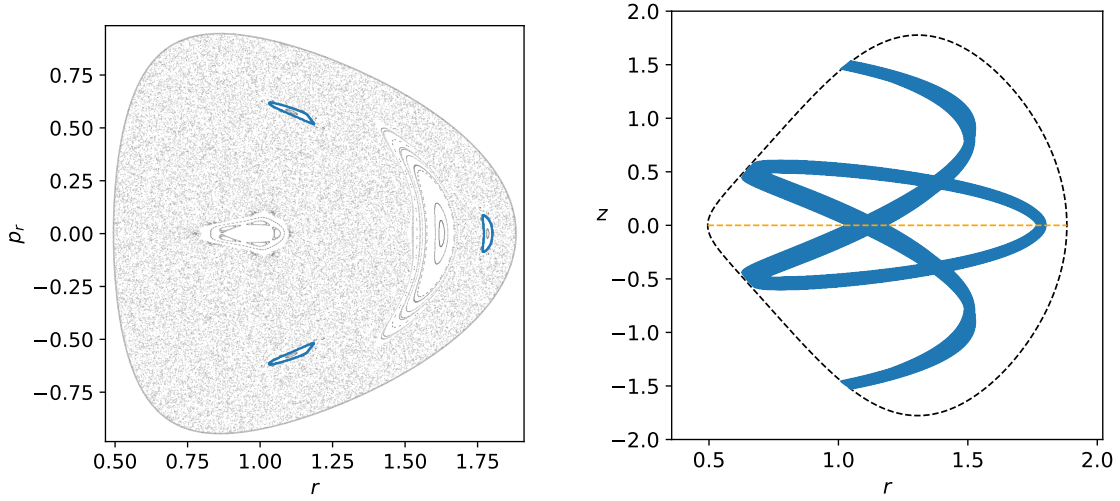
(b) A periodic trajectory that forms a closed curve.

Figure 4.3: Sample Poincaré and trajectory plot of an ordered periodic trajectory with constants of motion  $(L, E) = (1, 0.5)$ , and initial conditions  $(r, p_r, z) = (1.7844903, 0, 0)$ .

If we look at the central converging point of the curves in the resonant island, that Poincaré point represents a trajectory that locally passes exclusively through that point at  $z = 0$  as shown in Fig. (4.3). These Poincaré points correspond to a trajectory that forms a closed curve, which is a periodic orbit in  $(r, z)$ . Note that in

3d, this orbit is not periodic as shown in Fig. (2.1c), it is only periodic in  $(r, z)$ .

For the curves that form the resonant islands themselves, they correspond to trajectories that are weakly perturbed, weakly enough that their trajectories are similar enough to the periodic orbit in their center. An example of this is shown in Fig. (4.4), where the trajectory has a comparable structure to that of Fig. (4.3). These trajectories are ordered, but are distinguished from periodic with the name quasi-periodic trajectories.



(a) Poincaré points of the trajectory are highlighted in blue. These points create a closed curve that encloses its corresponding periodic orbit.

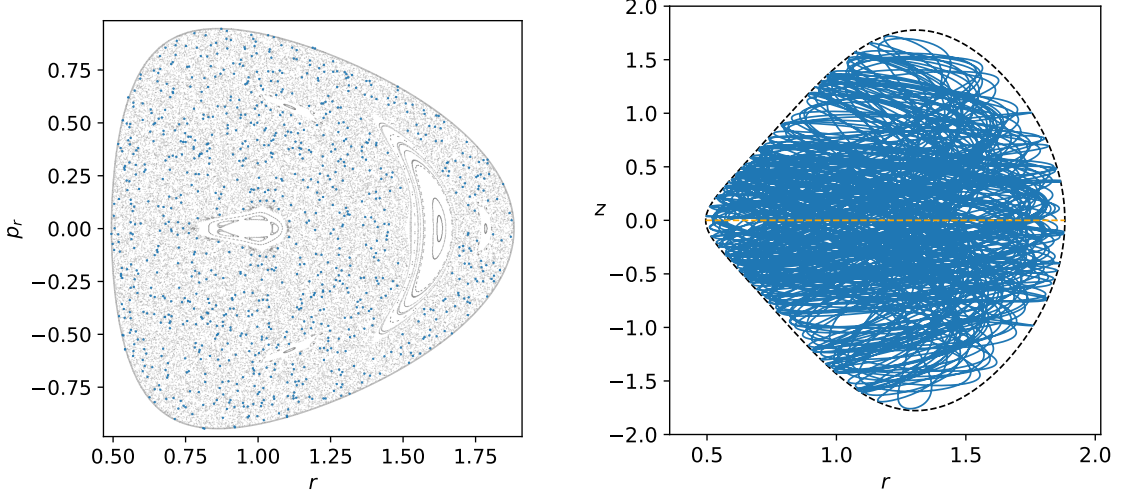
(b) A quasi-periodic trajectory, which covers a region near its corresponding periodic orbit

Figure 4.4: Sample trajectory and Poincaré plot of an ordered quasi-periodic trajectory with constants of motion  $(L, E)=(1, 0.5)$ , and initial conditions  $(r, p_r, z)=(1.8, 0, 0)$ .

What we want to show in this chapter is that trapped orbits are the ordered periodic and quasi-periodic trajectories themselves. This is because ordered trajectories are those by definition, will return to their initial condition. Because the trajectory returns, we know that they will never escape, thus are trapped.

Lastly, chaotic trajectories are present in the Poincaré plot in the chaotic sea, where the noise-like and practically random distribution of points imply sensitivity to small perturbations for every trajectory in this region. A sample trajectory is shown in Fig. (4.5).

The differing topologies of ordered and chaotic trajectories in the Poincaré plots allow us to quickly distinguish ordered and chaotic trajectories by eye, but our goal



(a) Poincaré points of the trajectory are highlighted in blue. The distribution of these points looks random all throughout the chaotic sea.

(b) A chaotic trajectory, whichy do not form closed curves or stay close to a closed curve

Figure 4.5: Sample trajectory and Poincaré plot of a chaotic trajectory with constants of motion  $(L, E)=(1, 0.5)$ , and initial conditions  $(r, p_r, z)=(1.85, 0, 0)$ .

is to accurately distinguish ordered and chaotic trajectories. Poincaré plots are sometimes unclear on which trajectories are ordered or chaotic, especially for plots with richer and more complex structures. Besides that, the distinction is qualitative at best. We cannot, for example, count how many trajectories are ordered. What we need is a more quantitative discriminator between ordered and chaotic trajectories, but we will still use Poincaré plots as a benchmark for the measure of chaos that we will actually use.

## 4.2 SALI

A famously known measure for chaos is the Lyapunov exponent  $\lambda$ , or Lyapunov Characteristic Number (LCN)[35]. It is defined using an initial deviation vector  $\vec{v}_0 = (v_{pr}, v_{pz}, v_r, v_z)$ , then for long enough times, the length of the deviation changes exponentially as it is time-evolved, i.e.

$$\|\vec{v}\| = \lim_{t \rightarrow \infty} \|\vec{v}_0\| e^{\lambda t}. \quad (4.1)$$

If a trajectory is chaotic,  $\lambda \geq 0$ , so that nearby trajectories deviate exponentially, which corresponds to sensitivity to initial conditions. If a trajectory is ordered,  $\lambda \approx 0$ ,

so that nearby trajectories don't approach each other (an example are trajectories in dissipative systems) nor deviate. To time-evolve these deviation vectors, we can get the variational equations by linearizing the equations of motion in Eqs. (2.23) to (2.28) [35]. For Eq. (2.26), the corresponding variational equation is

$$\dot{v}_{pr} = v_r \frac{\partial \dot{p}_r}{\partial r} + v_z \frac{\partial \dot{p}_r}{\partial z} + v_{pr} \frac{\partial \dot{p}_r}{\partial p_r} + v_{pz} \frac{\partial \dot{p}_r}{\partial p_z} \quad (4.2)$$

$$= - \left( \frac{1}{4} + \frac{3L^2}{r^4} + \frac{1}{R^3} - \frac{3r^2}{R^5} \right) v_r + \left( \frac{3rz}{R^5} \right) v_z \quad (4.3)$$

For the other equations of motion, their variational equations are

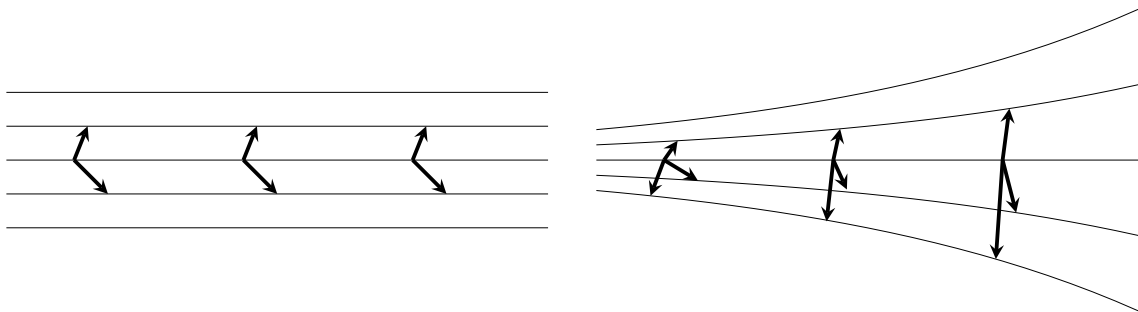
$$\dot{v}_{pz} = \left( \frac{3rz}{R^5} \right) v_r - \left( \frac{1}{R^3} - \frac{3z^2}{R^5} \right) v_z \quad (4.4)$$

$$\dot{v}_r = v_{pr} \quad (4.5)$$

$$\dot{v}_z = v_{pz}. \quad (4.6)$$

Generally, LCN is slowly converging [37]. If we want to analyze the chaotic motion of a large ensemble of trajectories, LCN is inefficient. We want to use a faster-converging measure to determine chaos.

What we can do is to use 2 deviation vectors instead of just 1, then compare their alignment when they are time-evolved. Generally, ordered and chaotic trajectories produce different alignments.



(a) For ordered trajectories, deviation vectors tend to stay separated. (b) For chaotic trajectories, deviation vectors tend to align parallel or anti-parallel.

Figure 4.6: Illustration of the time evolution of deviation vectors for ordered and chaotic trajectories.

In Fig. (4.6), we illustrate how for ordered trajectories that do not deviate, a pair of deviation vectors do not change their alignment, while for deviating chaotic trajectories, deviation vectors tend to align parallel or anti-parallel. The measure we

can use is called the Single Alignment Index or SALI [35–37]. For 2 deviation vectors  $\vec{v}_1$  and  $\vec{v}_2$ , SALI is defined as

$$\text{SALI}(t) = \log_{10}(\min(\|\vec{v}_1(t) + \vec{v}_2(t)\|, \|\vec{v}_1(t) - \vec{v}_2(t)\|)) \quad (4.7)$$

Note that for parallel vectors,  $\vec{v}_1 - \vec{v}_2 = 0$ , and for anti-parallel vectors,  $\vec{v}_1 + \vec{v}_2 = 0$ . So aligned deviation vectors produce  $\text{SALI}=-\infty$  and unaligned vectors produce finite SALI values. The convergence of SALI at  $t \rightarrow \infty$  is that it becomes a constant if the trajectory is ordered, and 0 if chaotic. For our setup, we will use two orthogonal initial deviation vectors  $\vec{v}_1 = (0, 0, 1, 0)$  and  $\vec{v}_2 = (0, 0, 0, 1)$ , note that any initially orthogonal vectors can be used, since we only care about the long term convergence of SALI. In Fig. (4.7), we show how the SALI evolves for the initial conditions of the trajectories in Figs. (4.3) to (4.5).

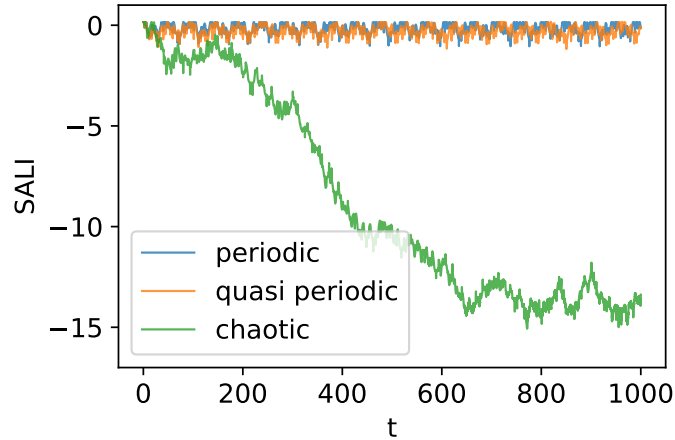


Figure 4.7: Time-evolved SALI values for a periodic ordered (blue), quasi-periodic ordered (orange), and chaotic (green) trajectory.

We can now calculate the SALI for a set of trajectories for our system and compare them to their corresponding Poincaré plots. In Fig. (4.8), we plot the initial conditions of the trajectories, then the color represents each trajectory's  $\log_{10}(\text{SALI})$ , and see that the low values (violet) represent SALI values that converges to 0, meaning, are the chaotic trajectories. On the contrary, the trajectories with relatively high values (yellow to orange), represent those with SALI converging to a non-zero value, which represents the ordered trajectories. Note how the yellow ordered trajectories in the SALI plot correspond to the resonant island of the Poincaré plot. We chose  $L$  and  $E$  such that the Poincaré plot exhibit a rich structure of order and chaos that is

somewhat obscure due to the nature of Poincaré plots. Contrary to that, the SALI plot makes it clear which trajectories are ordered and chaotic.

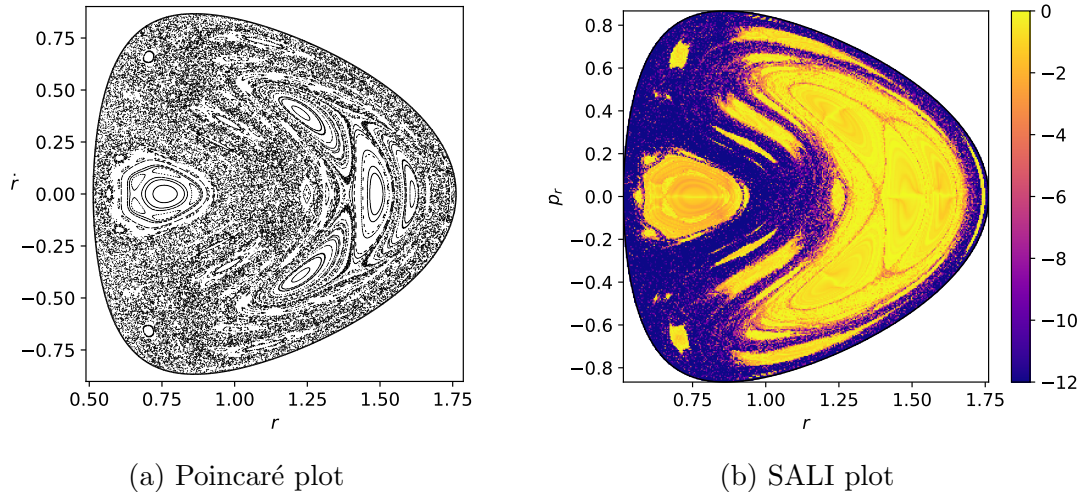


Figure 4.8: Plots for  $(L, E) = (1.0, 0.42)$  that differentiate order and chaos. The SALI plot (b) more clearly shows the distinction between ordered and chaotic trajectories compared to the Poincaré plot (a).

Now that we have a proper quantitative metric for chaos, we can use this as a basis for finding the existence of ordered trajectories, especially for those with escaping energy  $E > 1$ . What we first need is a threshold value for the SALI that allows us to separate ordered, and chaotic.

We can plot the SALI values of the same initial conditions as in Fig. (3.7) to see the nature of these trapped orbits. What we get is Fig. (4.9), where that the regions with the high pass values and no escaping trajectories, are those that have low SALI values. We can then conclude that the trapped inescapable orbits, are ordered trajectories that exist for  $E > 0$ , the energy range for open phase spaces that allow for escape.

We can be more exact with distinguishing between ordered and chaotic trajectories by setting a boundary SALI value. To do this, we can use the sample SALI plot in Fig. (4.10) with  $(L, E) = (5.0, 1.0)$ . We notice the orange colored region around the center. The existence of these region is similar to that of the 0-pass trajectories. But since the chosen energy here is  $E = 1$ , in which the escape channel is only a single point wide. We know these trajectories are just those that has not touched the ZVC, and that we just have not integrated for a long enough time to see them collapse. While they have not collapsed, they move cyclotronically similar to ordered orbits.

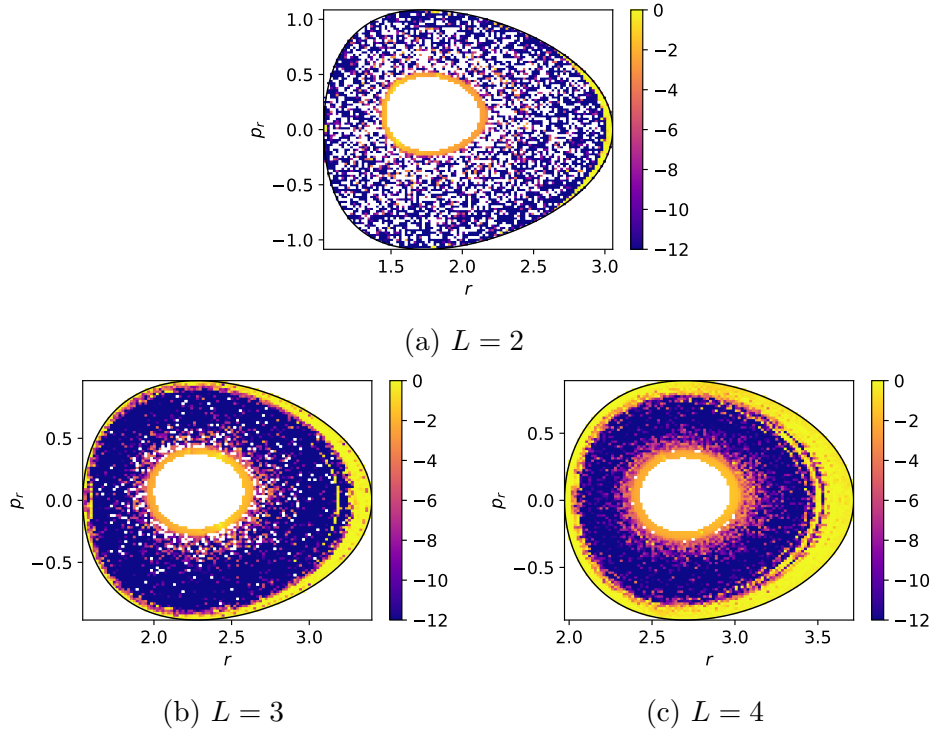


Figure 4.9: SALI plots of increasing  $L$ , with a constant energy  $E = 1.1$ . Escaping trajectories are omitted. The regions with no escaping trajectories in Fig. (3.7) have low SALI values.

So, we ought to choose a boundary that does not include these 0-pass trajectories as ordered. To do so, we plot the slice along  $p_r = 0$ , and see that the SALI values of the central region do not go above  $\text{SALI} = -1.0$ ; we choose this to be the boundary between ordered and chaotic. In Fig. (4.11) we show a version of Fig. (4.9) where we choose yellow to show ordered trajectories, and blue to show chaotic trajectories.

With this, we can now calculate the proportion of trajectories that are ordered, for a given set of constants of motion. Overall, we now have an explicit quantity of global chaos for a given  $(L, E)$ . We plot in Fig. (4.12) the percentage of ordered trajectories for a given  $L$  and  $E$ , showing the energy of escape. It can be seen that the system generally becomes ordered for lower  $E$ , which is reasonable as lower energies approach the stable equilibrium circular orbit. Also, higher  $L$ 's increase the amount of ordered trajectories; even for  $E > 1$ , the region of open Hamiltonian with possibility of escape, we see that the percent of ordered trajectories is non-zero, which tells us that ordered trajectories with escaping energy exist. These ordered trajectories will never escape, since they produce periodic or quasi-periodic motion, and are the trapped orbits of our system.

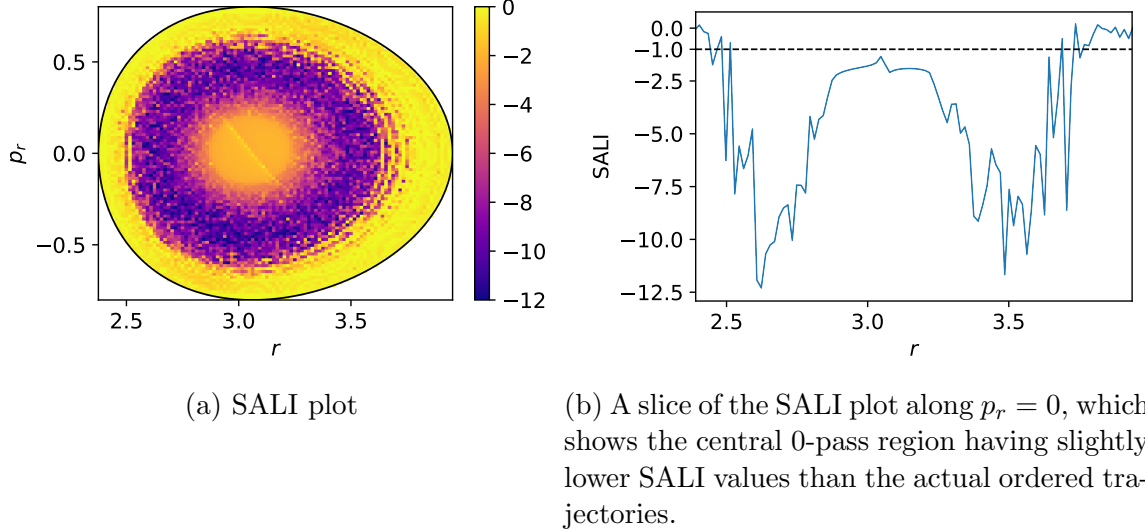


Figure 4.10: SALI plot for  $(L, E) = (5.0, 1.0)$

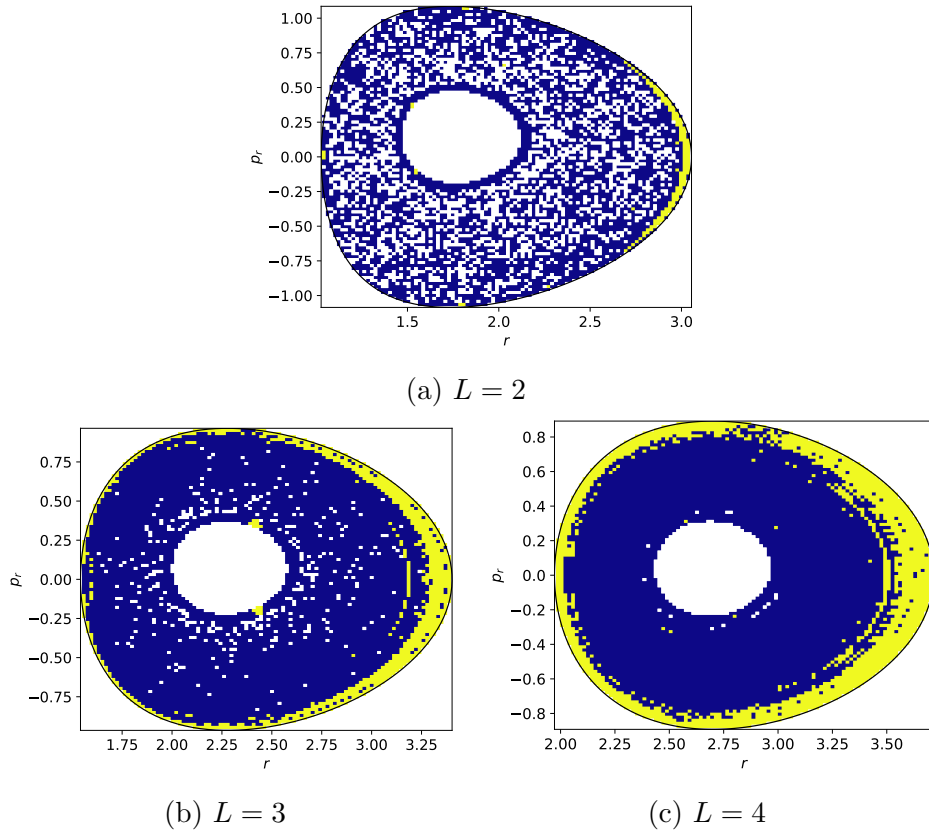


Figure 4.11: Plots of increasing  $L$ , with a constant energy  $E = 1.1$ , which show the ordered trajectories in yellow, and chaotic trajectories in blue.

With this, we can conclude that for energies greater than the energy of escape  $E > 1$ , it is possible that trajectories stay trapped, or more accurately, ordered. The parameter that increases the existence of these trapped orbits is the quantity

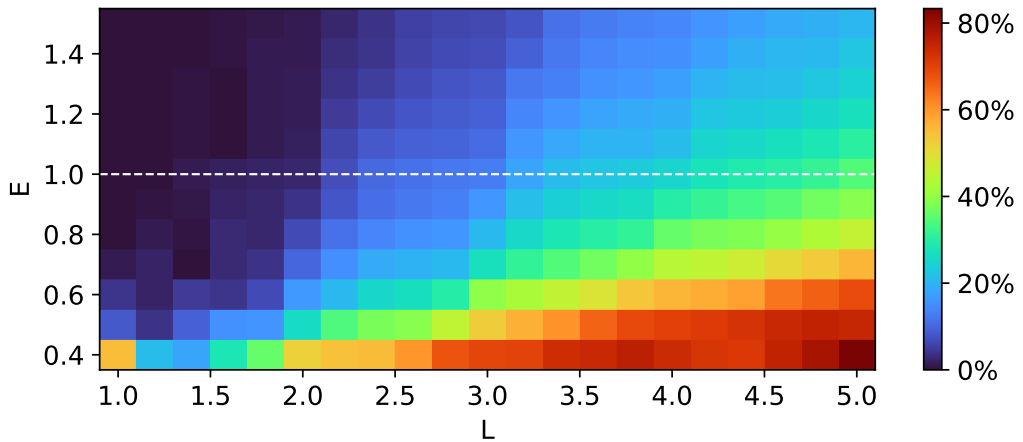
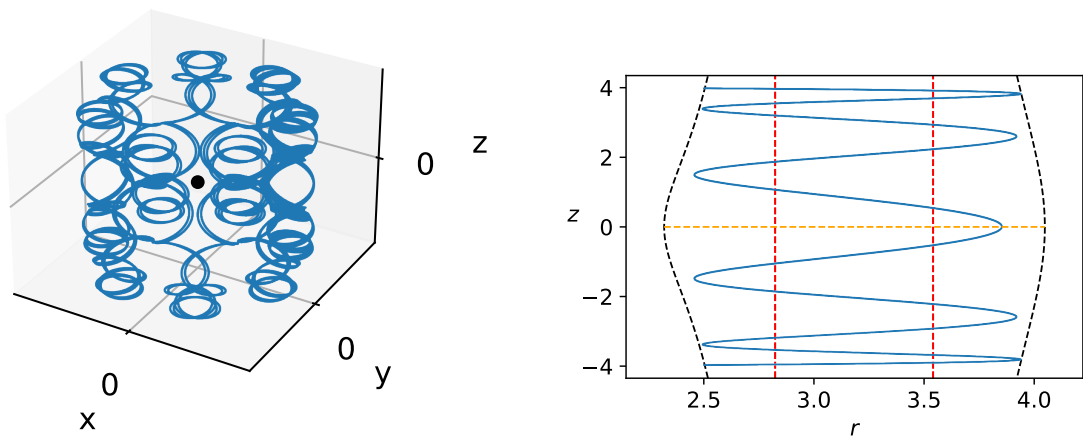


Figure 4.12: Heatmap showing the percentage of ordered trajectories for varying  $E$  and  $L$ .

$L$ . If we look back at Eq. (2.19), we see that high  $L$  is the regime of weak gravity and strong magnetic field. Thus, it can be concluded in the physical scales, that ordered trajectories exists for weak gravity. But note that the zero gravity limit corresponds to cyclotronic motion that continues on towards  $z \rightarrow \pm\infty$ . So, the weak gravitational force affects the system enough such that these cyclotronic trajectories become ordered orbits. This is demonstrated on Fig. (4.13), where the trajectory is plotted in 3D and 2D. Gravitational effects are weak enough to not perturb the trajectory from helical motion, but strong enough to make the trajectory return downwards.



(a) 3D plot of a trapped orbit. The ordered nature of the trajectory is obfuscated by the angular motion.

(b) 2D plot of a trapped orbit. The ordered nature of the trajectory is explicit here. Despite the trajectory being open to infinity, as shown by the red asymptotes of escape, the trajectory will never escape as it is restricted to an ordered periodic motion.

Figure 4.13: Trajectory plots of a trapped orbit showin in 3D (a) and in 2D (b). The gravitational force weak enough to keep the helical motion of the orbits, but strong enough to “trap” the orbit.

# Chapter 5

## Magnetized Black Hole

In this chapter, the equations of motion for the magnetized black hole (MBH) system will be derived. Much of the analysis done for the MNC case will be similarly done. The Hamiltonian will be derived, then non-dimensionalized. An effective potential will also be derived, as well as the special quantities for this potential: the equilibrium points, whose amount highly depends on the parameters, the minimum energy of escape, the energy where the phase space opens to infinity, and the escape channel radius, the radius where the phase space first opens to infinity. Because the system is now relativistic, the black hole becomes relevant as capture towards it is now possible, this would affect escapes from this system. Similar to what was done for the MNC case, we will derive a reparametrized energy such that the escape energy is at 1. The other two remaining parameters that are to be derived will also be non-dimensionalized, such that we find a symmetry, that allows us to restrict our analysis to just cases with positive angular momentum. Lastly, the classical limit of the Hamiltonian will be derived for the purposes of comparison to the MNC system.

### 5.1 System Set-up

For the system, we start by patterning our derivation from previous work that have studied this system [16, 17, 21]. We begin with the Schwarzschild metric expressed in time and spherically symmetric space ( $ct, R, \theta, \phi$ ):

$$ds^2 = g_{\mu\nu}dx^\mu dx^\nu = -fc^2dt^2 + \frac{1}{f}dR^2 + R^2d\Omega^2 \quad (5.1)$$

where

$$f = 1 - \frac{R_s}{R} \quad (5.2)$$

$$R_s = \frac{2GM}{c^2} \quad (5.3)$$

$$d\Omega^2 = d\theta^2 + \sin^2 \theta d\phi^2 \quad (5.4)$$

We use Einstein Summation Convention for the sake of brevity of the equations. There appears to be an apparent singularity on  $R = R_s$ , where the metric seems to break down.  $R_s$  can be thought of as the radius of the black hole, where every particle that reaches this distance is captured by the black hole. It is known as the *Schwarzschild radius* [45, 46].

Explicitly, the non-zero metric components are

$$g_{tt} = -fc^2 \quad (5.5)$$

$$g_{RR} = \frac{1}{f} \quad (5.6)$$

$$g_{\theta\theta} = R^2 \quad (5.7)$$

$$g_{\phi\phi} = R^2 \sin^2 \theta \quad (5.8)$$

The symmetry of the metric is apparent- it is just along the variables that do not explicitly appear in the metric components,  $t$  and  $\phi$ . The symmetry of the metric is mathematically described using *Killing vectors*, which are the vectors that point to the direction of the symmetry [15, 46, 47]. In component form, they are

$$\xi_{(t)}^\mu = (1, 0, 0, 0) \quad (5.9)$$

$$\xi_{(\phi)}^\mu = (0, 0, 0, 1), \quad (5.10)$$

where the parenthesized subscript is not a summation index, but the direction of the Killing vector symmetry.

The 4-potential of the uniform magnetic field with strength  $B$  is [15, 16]

$$A^\mu = \frac{B}{2} \xi_{(\phi)}^\mu = \left( 0, 0, 0, \frac{B}{2} \right). \quad (5.11)$$

Let us check if this 4-potential gives the proper magnetic field. First, we derive the electromagnetic Faraday Tensor  $F_{\mu\nu}$  [46].

$$F_{\mu\nu} = \nabla_\mu A_\nu - \nabla_\nu A_\mu, \quad (5.12)$$

where  $\nabla_\mu$  is the covariant derivative. The non-zero components of  $F$  are

$$F_{R\phi} = BR \sin^2 \theta = -F_{\phi R} \quad (5.13)$$

$$F_{\theta\phi} = BR^2 \sin \theta \cos \theta = -F_{\theta\phi}. \quad (5.14)$$

Then, we get the magnetic field with

$$B^\mu = -\frac{1}{2} \frac{\epsilon^{\mu\nu\lambda\sigma}}{\sqrt{-g}} u_\nu F_{\lambda\sigma}, \quad (5.15)$$

where  $\epsilon$  is the Levi-Civita Tensor. For a rest observer, the 4-velocity is given by

$$u_\mu = \sqrt{f} (\xi_{(t)})_\mu. \quad (5.16)$$

All in all, this gives

$$B^\mu = B\sqrt{f} \left[ \cos \theta \delta_r^\mu - \frac{1}{r} \sin \theta \delta_\theta^\mu \right] = B\sqrt{f} \left( 0, \cos \theta, 0, -\frac{1}{r} \sin \theta \right) \quad (5.17)$$

For the classical limit  $R_s \ll R$  and transforming the magnetic field to cylindrical coordinates

$$B_{\text{cyl}}^\mu = \frac{\partial x_{\text{cyl}}^\mu}{\partial x_{\text{sph}}^\nu} B_{\text{sph}}^\nu, \quad (5.18)$$

we get the same magnetic field as in the MNC case ( $B\hat{\mathbf{z}}$ ). Overall, the magnetic field is axis-symmetric and uniform at infinity.

## 5.2 Hamiltonian of the System

We can derive the equations of motions from [17, 21]

$$m(\dot{x}^\mu + \Gamma_{\alpha\beta}^\mu \dot{x}^\alpha \dot{x}^\beta) = qF_\nu^\mu \dot{x}^\nu, \quad (5.19)$$

which can be thought of as similar to the force equation ( $ma = F$ ). But for the sake of comparison, and the usage of Hamiltonian in SALI, we ought to derive the equations of motion using the Hamiltonian formalism. The Hamiltonian of a relativistic particle influenced by a magnetic field can be expressed as [20, 45, 46]

$$\mathcal{H} = \frac{1}{2m} g^{\mu\nu} (p_\mu - qA_\mu)(p_\nu - qA_\nu) + \frac{1}{2} mc^2, \quad (5.20)$$

where  $p_\mu$  is the canonical momentum. Since the system is symmetrical along the coordinates  $t$  and  $\phi$ , their canonical momenta have to be constant. The canonical momenta  $p_\mu = g_{\mu\nu} (m\dot{x}^\nu + qA^\nu)$  are

$$p_t = -mc^2 f \dot{t} = -\mathcal{E} \quad (5.21)$$

$$p_R = m \frac{\dot{R}}{f} \quad (5.22)$$

$$p_\theta = m R^2 \dot{\theta} \quad (5.23)$$

$$p_\phi = R^2 \sin^2 \theta \left( m \dot{\theta} + \frac{qB}{2} \right) = L, \quad (5.24)$$

where  $\mathcal{E}$  and  $L$  are the total energy and angular momentum respectively. So explicitly, the Hamiltonian is

$$\mathcal{H} = \frac{1}{2m} \left( -\frac{\mathcal{E}^2}{fc^2} + fp_R^2 + \frac{p_\theta^2}{R^2} + \left( \frac{L}{R \sin \theta} - \frac{qB}{2} R \sin \theta \right)^2 \right) + \frac{1}{2} mc^2 \quad (5.25)$$

We non-dimensionalize this Hamiltonian using the characteristic scales

$$R_c = R_s \quad (5.26)$$

$$t_c = \frac{R_s}{c} \quad (5.27)$$

We also factor out the units of the Hamiltonian  $\mathcal{H}$ , energy  $E$ , and the canonical momenta  $p_R$  and  $p_\theta$ :

$$\mathcal{H} \rightarrow \frac{mR_c^2}{t_c^2} \mathcal{H} \quad (5.28)$$

$$\mathcal{E} \rightarrow \frac{mR_c^2}{t_c^2} \mathcal{E} \quad (5.29)$$

$$p_R \rightarrow \frac{mR_c}{t_c} p_R \quad (5.30)$$

$$p_\theta \rightarrow \frac{mR_c^2}{t_c} p_\theta \quad (5.31)$$

Overall, the Hamiltonian reduces to

$$\mathcal{H} = \frac{1}{2} \left( -\frac{\mathcal{E}^2}{f} + fp_R^2 + \frac{p_\theta^2}{R^2} + \left( \frac{L}{mcR_s R \sin \theta} - \frac{qBR_s}{2mc} R \sin \theta \right)^2 + 1 \right), \quad (5.32)$$

$$f = 1 - \frac{1}{R} \quad (5.33)$$

Finally, we get the non-dimensionalized angular momentum  $L$ , and the magnetic interaction parameter  $B$ , through the transformations

$$\frac{L}{mcR_s} \rightarrow L \quad (5.34)$$

$$\frac{qBR_s}{2mc} \rightarrow B. \quad (5.35)$$

This gives us the final Hamiltonian as

$$\mathcal{H} = \frac{1}{2} \left( -\frac{\mathcal{E}^2}{f} + fp_R^2 + \frac{p_\theta^2}{R^2} + \left( \frac{L}{R \sin \theta} - BR \sin \theta \right)^2 + 1 \right). \quad (5.36)$$

In turn, this gives the equations of motion to be used for numerical integration:

$$\dot{p}_R = -\frac{\mathcal{E}^2}{2(R-1)^2} - \frac{p_R^2}{2R^2} + \frac{p_\theta^2}{R^3} + \frac{L^2}{R^3 \sin^2 \theta} - RB^2 \sin^2 \theta \quad (5.37)$$

$$\dot{R} = p_R \left( 1 - \frac{1}{R} \right) \quad (5.38)$$

$$\dot{p}_\theta = \frac{L^2 \cos \theta}{R^2 \sin^3 \theta} - B^2 R^2 \sin \theta \cos \theta \quad (5.39)$$

$$\dot{\theta} = \frac{p_\theta}{R^2} \quad (5.40)$$

From the Hamiltonian in Eq. (5.36), we can also get the energy equation by setting  $\mathcal{H} = 0$  to get

$$\mathcal{E}^2 = f^2 p_R^2 + \frac{fp_\theta^2}{R^2} + U \quad (5.41)$$

$$U = \left( 1 - \frac{1}{R} \right) \left[ 1 + \left( \frac{L}{R \sin \theta} - BR \sin \theta \right)^2 \right] \quad (5.42)$$

This could also have been derived from the normalization condition of the 4-velocity  $\dot{x}^\mu \dot{x}_\mu = -1$ .

We will numerically integrate the equations of motion for a given set of initial conditions  $(p_R, R)$ , along the equatorial plane  $\theta = \pi/2$ .  $p_\theta$  will be derived using Eq. (5.41) given the finite parameters  $(B, L, \mathcal{E})$ . Next, we note what happens for the maximal values of  $p_R$ , which occurs for  $p_\theta = U = 0$ ,

$$p_R^2 = \frac{\mathcal{E}^2}{f^2}. \quad (5.43)$$

Near the black hole surface,  $R \rightarrow 1$  and  $f \rightarrow 0$ , so the range of values for  $p_R$  is  $[-\infty, \infty]$ . This would be very inconvenient for analysis of the dynamics of all initial conditions given a set of  $(B, L, \mathcal{E})$ . What we can do to remedy this is to instead use the raised index form of the momentum,

$$p_R = g_{RR} p^R = \frac{p^R}{f} \quad (5.44)$$

If this is substituted into Eq. (5.43), we get  $(p^R)^2 = \mathcal{E}^2$ , which restricts the range to  $p^R \in [-\mathcal{E}, \mathcal{E}]$ . For our numerical analysis, we will choose initial conditions in terms of  $p^R$ , then convert to  $p_R$  for direct numerical integration.

Compared to the dimensionless Hamiltonian and equations of motion of the MNC, we have an extra parameter in the form of  $B$ . This is due to the addition of another dimensionful parameter, the speed of light  $c$ . We opted to use the scales that we use to keep our black hole radius, thus black hole capture of trajectories, unchanging depending on the constants of motion.

If we again attempt to calculate our scales similar to what was done for the MNC, we again use  $M \approx 7.96 \times 10^{36}\text{m}$  [43]. We get  $r_c = 1.18 \times 10^{10}\text{m}$  and  $t_c = 39.3\text{s}$ . Here we see a less extreme time scale compared to MNC.

## 5.3 Potential Analysis

In this section, we analyze the potential in Eq. (5.42). The equilibrium point/s, and the openings to infinity will be elaborated and discussed in detail.

### 5.3.1 Equilibrium

For the potential of this system, there can be 0, 1, or 2 equilibrium points all along the equatorial plane  $\theta = \pi/2$ , the number depends on the values of  $L$  and  $B$ . The single equilibrium point is a special point that gives the radius of the Innermost Stable Circular Orbit (ISCO). The derivation of this point is thoroughly done by Frolov and Shoom [17]. It is derived by setting  $\partial_R U = \partial_R^2 U = 0$ , then getting the parameters  $(B, L)$  that gives the equilibrium point. For a given ISCO radius  $R = \rho$ , there are 2 sets of  $(B, L)$  that are possible, one for positive  $L$ , and one for negative  $L$ . These parameters are given in terms of the ISCO radius as

$$B_{\text{ISCO},\pm} = \frac{1}{\rho} \sqrt{\frac{3 - \rho}{2(4\rho^2 - 9\rho + 3 \pm \sqrt{(3\rho - 1)(3 - \rho)})}}, \quad (5.45)$$

$$L_{\text{ISCO},\pm} = \pm \rho \sqrt{\frac{3\rho - 1}{2(4\rho^2 - 9\rho + 3 \pm \sqrt{(3\rho - 1)(3 - \rho)})}}. \quad (5.46)$$

For  $L > 0$  the ISCO radius is limited to  $1 < \rho \leq 3$ , but for  $L < 0$ , the lower bound becomes  $(5 + \sqrt{13})/4 \approx 2.15$ .  $L$  dictates how many equilibrium point there exists.  $L = L_{\text{ISCO}}$  produces a single saddle point equilibrium. If  $L < L_{\text{ISCO}}$ , there are no equilibrium points and the potential is monotonically increasing. If  $L > L_{\text{ISCO}}$ , there are 2 equilibrium points, where the inner equilibrium point is always unstable, and the outer equilibrium point is always stable, as shown in Fig. (5.1). How the equilibrium points diverge for a given  $\rho$  depending on the value of  $L$  is shown in Fig. (5.2).

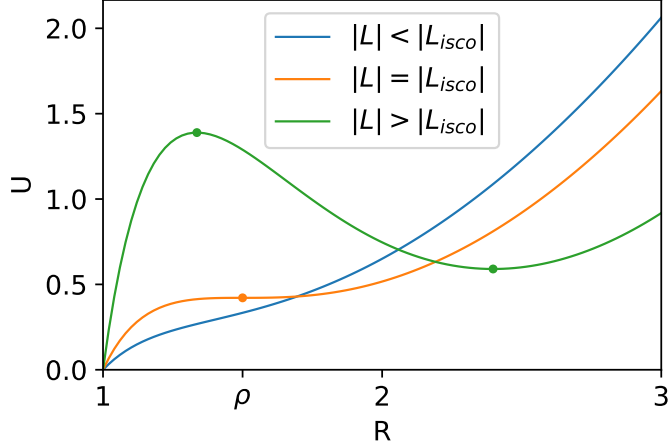


Figure 5.1: Sample plots of the potential along the equatorial plane. For  $|L| < |L_{\text{ISCO}}|$  (blue curve), there are no equilibrium points, so the potential energy is monotonically increasing away from  $R$ . For  $|L| = |L_{\text{ISCO}}|$  (orange curve), the equilibrium is located on the ISCO radius  $\rho$ . For  $|L| > |L_{\text{ISCO}}|$  (green), the equilibrium points diverge to two points, the inner being unstable, and the outer being stable.

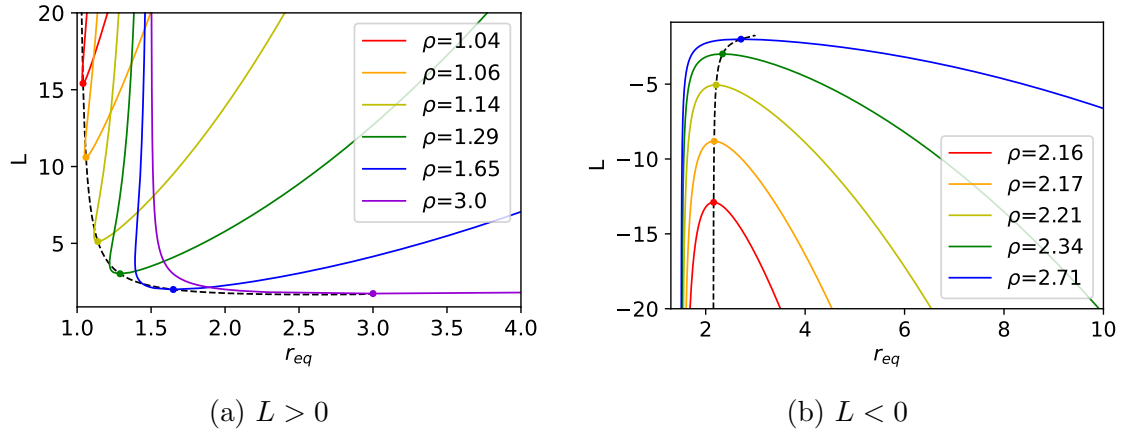


Figure 5.2: Plots that demonstrate how the equilibrium points bifurcate from  $\rho$  as  $|L|$  increases for  $L > 0$  values (a) and  $L < 0$  values (b). The equilibrium points originate from  $L_{\text{ISCO}}$  represented by the dashed black lines.

The limit  $\rho \rightarrow 3$  can be thought of as the null magnetic field limit, because as  $\rho \rightarrow 3$ ,  $B_{\text{ISCO},\pm} \rightarrow 0$ . On the other hand, as  $\rho$  approaches the lower limit,  $B_{\text{ISCO},\pm} \rightarrow \infty$ . Simply, low  $\rho$  is the strong magnetic field limit, while high  $\rho$  is the weak magnetic field limit.

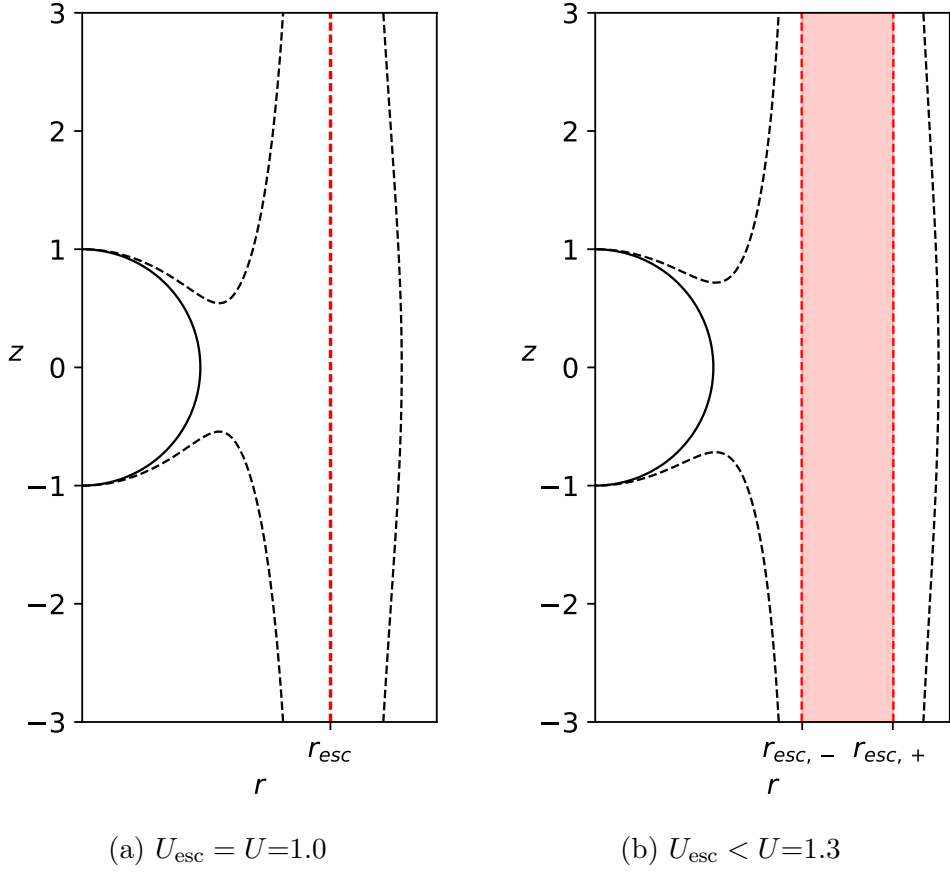


Figure 5.3: Zero Velocity Curves (dashed) of the potential for a given  $(B, L)$  with energies equal and greater than  $U_{\text{esc}}$ , where the asymptotes of escape are shown in red dashed lines. Higher energies widen this escape channel.

### 5.3.2 Open Zero Velocity Curves

To see where the potential opens to infinity for the purposes of escape analysis, we represent the potential from Eq. (5.42) in cylindrical coordinates  $(r, \theta, z)$  as

$$U(r, z) = \left(1 - \frac{1}{\sqrt{r^2 + z^2}}\right) \left[1 + \left(\frac{L}{r} - Br\right)^2\right]. \quad (5.47)$$

For the limit  $z \rightarrow \infty$ , we get the potential energy needed for the ZVC to exist at infinity, meaning, the potential needed for escape,

$$U_{\text{esc}} = 1 + \left(\frac{L}{r} - Br\right)^2. \quad (5.48)$$

Solving for the ZVC position at infinity  $r_{\text{esc}}$ , we get

$$0 = B^2 r_{\text{esc}}^4 + (1 - U_{\text{esc}} - 2lb)r_{\text{esc}}^2 + L^2 \quad (5.49)$$

$$r_{\text{esc},\pm} = \frac{1}{B\sqrt{2}} \sqrt{(U_{\text{esc}} + 2LB - 1) \pm \sqrt{(U_{\text{esc}} - 1)(U_{\text{esc}} - 1 + 4LB)}} \quad (5.50)$$

We get similar open ZVC properties to the MNC case. The ZVC is generally closed for low energies, then after a threshold energy  $\mathcal{E}^2 = U_{\text{esc}}$ , the ZVC opens towards infinity, where it asymptotically approaches the value  $r_{\text{esc},\pm}$ . The energy and radius where the ZVC first opens can be derived by finding when the discriminant of Eq. (5.50) vanishes; where we get the minimum energy of escape, and the radius where ZVC first opens towards infinity as

$$U_{\text{esc,min}} = 1 + 2B(|L| - L) = \begin{cases} 1 & , L > 0 \\ 1 - 4BL & , L < 0 \end{cases} \quad (5.51)$$

$$r_{\text{esc}} = \sqrt{\frac{|L|}{B}} \quad (5.52)$$

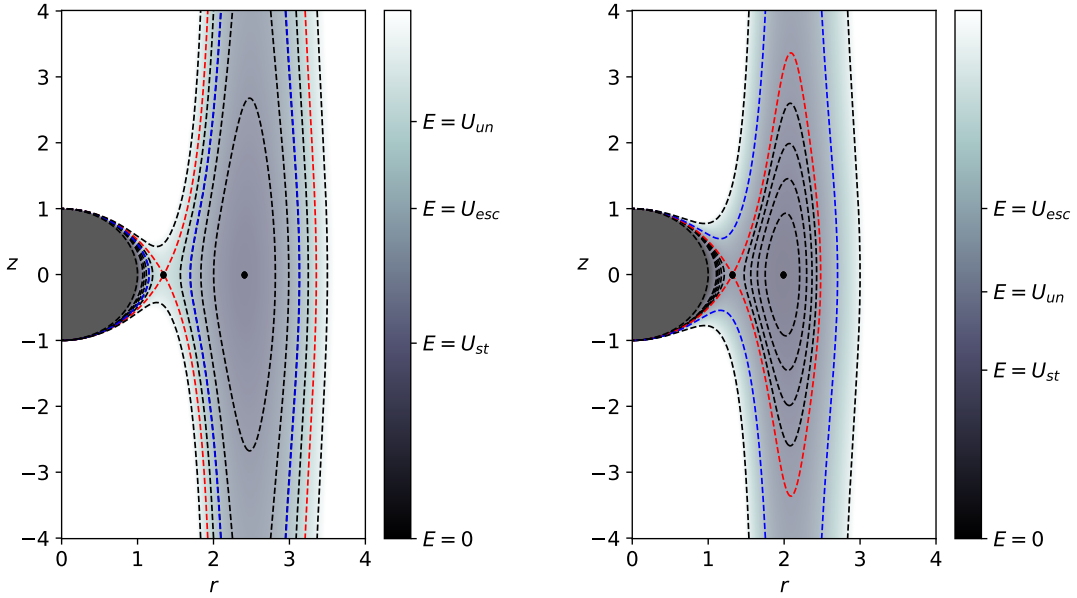
Potential energies greater than  $U_{\text{esc,min}}$  open the channel even further, as shown in Fig. (5.3)

### 5.3.3 Black Hole Capture

Along the surface of the black hole  $R = 1$ , the potential, given by Eq. (5.42), becomes 0. As discussed before, any trajectory that crosses  $R = 1$  is captured by the black hole. In some sense, black hole capture can be thought of as another escape basin [21], similar to escape along  $z \rightarrow \infty$ , and along  $z \rightarrow -\infty$ . For  $|L| \leq |L_{\text{ISCO}}|$ , black hole capture is always accessible as no equilibrium points exists, as shown by the blue curve in Fig. (5.1). But for cases where  $|L| > |L_{\text{ISCO}}|$ , the existence of an unstable equilibrium point allows some trajectories to never be captured by the black hole, as long as the total energy is less than that of the energy of the unstable equilibrium point. It is important to note that the energy needed for the ZVC to open towards  $z \rightarrow \infty$ , and to open towards the black hole, are independent of each other. Meaning, either capture to the black hole, or escape to infinity, can occur first if we slowly increase the energy of the system depending on the parameters. This is illustrated in Fig. (5.4), where the ZVC that first opens to infinity, may or may not occur for lower energies than the ZVC that first opens to black hole capture.

## 5.4 Reparametrization

In this section, we reparametrize the energy to a new parameter  $E$  such that the energy of escape is always at  $E = 1$ , similar to what was done in the MNC case, and



(a) Energy for opening to  $z \rightarrow \infty$  occurs for lower energy than opening to the black hole.

(b) Energy for opening to the black hole occurs for lower energy than opening to  $z \rightarrow \infty$ .

Figure 5.4: Each dashed curve represents a zero velocity curve of the potential for a given set of parameters. Darker colors mean lower magnitudes of the effective potential energy, in other words, darker colors represent the “depth” of the energy well. Lower energy ZVC’s are enclosed by the higher energy ones. Each plot represents a pair of parameters  $B$  and  $L$  chosen such that it differs whether capture to the black hole or escape to infinity opens first for lower energies. We highlight the ZVC that first opens to  $z \rightarrow \infty$  (blue) with potential energy  $U_{\text{esc}}$ , and the ZVC that first opens to the black hole (red) with potential energy  $U_{\text{un}}$ .  $U_{\text{st}}$  is the potential energy of the stable equilibrium.

we will also find a symmetry such that we only need to analyze  $L > 0$ . The energy reparametrization is defined as

$$\mathcal{E}^2 = U_{\text{esc},\min} E = [1 + 2B(|L| - L)] E. \quad (5.53)$$

Substituting in Eq. (5.51) gives,

$$E = \frac{1}{1 + 2B(|L| - L)} \left(1 - \frac{1}{R}\right) \left[1 + \left(\frac{L}{r} - Br\right)^2\right]. \quad (5.54)$$

Further, we can reparametrize  $B$  and  $L$  with the following conjecture: for  $L < 0$ , given the parameters  $(B, L) = (B_-, L_-)$  and the rescaled energy  $E$ , there exists a positive  $L$  parameter set  $(B_+, L_+)$  that produces the exact same energy  $E$  in Eq. (5.54). In other words,  $E$  is symmetrical under  $(B_+, L_+) \Leftrightarrow (B_-, L_-)$ . To prove this

and handwavingly derive  $(B_{\pm}, L_{\pm})$ , we simply equate the expression from Eq. (5.54) for  $(B_+, L_+)$  and  $(B_-, L_-)$ .

$$\left(1 - \frac{1}{R}\right) \left[1 + \left(\frac{L_+}{r} - B_+ r\right)^2\right] = \frac{1}{1 - 4B_- L_-} \left(1 - \frac{1}{R}\right) \left[1 + \left(\frac{L_-}{r} - B_- r\right)^2\right] \quad (5.55)$$

Then, we substitute

$$L_{\pm} = \pm \frac{\mathcal{L}}{\sqrt{4\rho^2 - 9\rho + 3 \pm \sqrt{(3\rho - 1)(3 - \rho)}}} \quad (5.56)$$

$$B_{\pm} = \frac{\mathcal{B}}{\sqrt{4\rho^2 - 9\rho + 3 \pm \sqrt{(3\rho - 1)(3 - \rho)}}} \quad (5.57)$$

where  $\rho$  is the ISCO radius. Notice how the denominators we substitute are from Eqs. (5.45) and (5.46). Upon substituting and simplifying, we get

$$2\mathcal{B}\mathcal{L} = \sqrt{(3\rho - 1)(3 - \rho)} \quad (5.58)$$

This can be thought of as the condition that is needed to ensure the symmetry; we can freely choose  $\mathcal{B}$  and  $\mathcal{L}$  but they should adhere to the above equation. Next, we use the position of the escape channel  $r_{\text{esc}}$  from Eq. (5.52)

$$r_{\text{esc}}^2 = \frac{\mathcal{L}}{\mathcal{B}} \quad (5.59)$$

to solve directly for  $\mathcal{L}$  and  $\mathcal{B}$ , which gives

$$\mathcal{L} = \frac{r_{\text{esc}}}{\sqrt{2}} \sqrt[4]{(3\rho - 1)(3 - \rho)} \quad (5.60)$$

$$\mathcal{B} = \frac{1}{r_{\text{esc}}\sqrt{2}} \sqrt[4]{(3\rho - 1)(3 - \rho)}. \quad (5.61)$$

Substituting this back to Eq. (5.56) and (5.57), we get

$$L_{\pm} = \pm \frac{r_{\text{esc}} \sqrt[4]{(3 - \rho)(3\rho - 1)}}{\sqrt{2 \left(4\rho^2 - 9\rho + 3 \pm \sqrt{(3\rho - 1)(3 - \rho)}\right)}}, \quad (5.62)$$

$$B_{\pm} = \frac{\sqrt[4]{(3 - \rho)(3\rho - 1)}}{r_{\text{esc}} \sqrt{2 \left(4\rho^2 - 9\rho + 3 \pm \sqrt{(3\rho - 1)(3 - \rho)}\right)}}. \quad (5.63)$$

Overall, we have reparametrized from  $(B, L, \mathcal{E})$  to  $(r_{\text{esc}}, \rho, E)$  with Eqs. (5.53), (5.62), and (5.63). For the equilibrium points in this parameter space, we use Eqs.

(5.52), (5.45), and (5.46) to derive the  $r_{\text{esc}}$  value that produces the single equilibrium point

$$r_{\text{esc, ISCO}} = \rho \sqrt[4]{\frac{3\rho - 1}{3 - \rho}}. \quad (5.64)$$

$r_{\text{esc}}$  itself gives the ISCO parameters that produces 1 equilibrium point. Values higher than this gives 2 equilibrium point, and lower values gives no equilibrium points as demonstrated in Fig. (5.5)

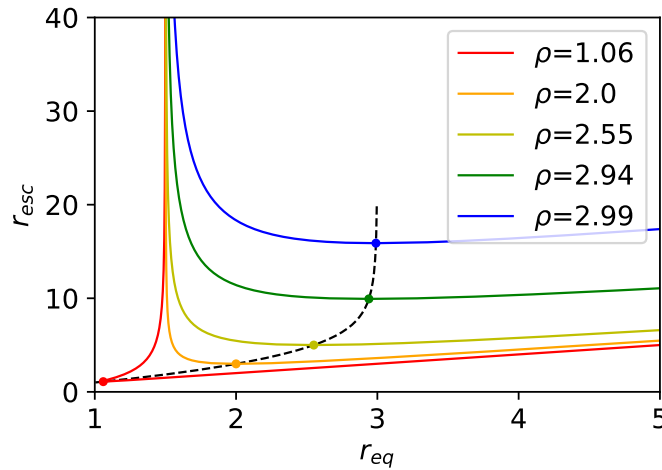


Figure 5.5: A plot that demonstrates how the equilibrium points bifurcate from  $\rho$  as  $r_{\text{esc}}$  increases. The equilibrium points originate from  $r_{\text{esc,ISCO}}$  represented by the dashed black lines.

To say that there is complete symmetry in this new parameter space, it is not enough that the reparametrized energy  $E$  is symmetrical under a parity transformation of  $L$ . We still have to see if the initial conditions along  $(p^R, R)$  with these parameters indeed produce the same trajectory for positive and negative  $L$ . We should look at the energy equation (5.41) and equations of motion (5.37) to (5.40) to ensure the symmetry.

The complete set of transformations that have symmetrical trajectories are

$$t \rightarrow \frac{t}{\sqrt{U_{\text{esc,min}}}} \quad (5.65)$$

$$p_\mu \rightarrow \sqrt{U_{\text{esc,min}}} p_\mu \quad (5.66)$$

$$\mathcal{H} \rightarrow U_{\text{esc,min}} \mathcal{H} \quad (5.67)$$

Note that these are just identity transformations for positive  $L$  as  $U_{\text{esc,min}} = 1$  for  $L > 0$ , so nothing has to be done numerically to ensure the symmetry.

## 5.5 Newtonian Limit

For the interest of comparing the MNC and MBH systems, we ought to rederive the MBH Hamiltonian in isotropic coordinates [45, 46]. Isotropic coordinates ensure that the spatial portion of the coordinates is Euclidean, similar to that of flat space. These are also the coordinates for the MNC. The conversion from the Schwarzschild radius  $R$  to the isotropic radius  $\rho$  is

$$R = \rho \left( 1 + \frac{R_s}{4\rho} \right)^2. \quad (5.68)$$

Applying this conversion on the Schwarzschild metric from Eq. (5.1) to convert it into isotropic coordinates  $(t, \rho, \theta, \phi)$  gives

$$ds^2 = - \left( \frac{4\rho - R_s}{4\rho + R_s} \right)^2 dt^2 + \left( 1 + \frac{R_s}{4\rho} \right)^4 (d\rho^2 + \rho^2 d\Omega^2). \quad (5.69)$$

For the benefit of comparison with the MNC Hamiltonian from Eq. (2.10), we convert the spatial portion from spherical  $(\rho, \theta, \phi)$  to cylindrical  $(r, \theta, z)$ , which gives

$$ds^2 = - \left( \frac{4\sqrt{r^2 + z^2} - R_s}{4\sqrt{r^2 + z^2} + R_s} \right)^2 dt^2 + \left( 1 + \frac{R_s}{4\sqrt{r^2 + z^2}} \right)^4 (dr^2 + r^2 d\theta^2 + dz^2) \quad (5.70)$$

Using this metric, we can derive the Hamiltonian from Eq. (5.20) and get

$$\begin{aligned} \mathcal{H} = & \frac{1}{2m} \left( - \left( \frac{4\sqrt{r^2 + z^2} + R_s}{4\sqrt{r^2 + z^2} - R_s} \right)^2 \frac{\mathcal{E}^2}{c^2} + \left( 1 + \frac{R_s}{4\sqrt{r^2 + z^2}} \right)^{-4} (p_r^2 + p_z^2) \right. \\ & \left. + \left[ \frac{L}{r} \left( 1 + \frac{R_s}{\sqrt{r^2 + z^2}} \right)^{-2} - \frac{qB}{2} r \left( 1 + \frac{R_s}{\sqrt{r^2 + z^2}} \right)^2 \right]^2 \right) + \frac{1}{2} mc^2 \end{aligned} \quad (5.71)$$

The limit to get the MNC Hamiltonian is the low-velocity limit, which can correspond to setting the speed of light  $c \rightarrow \infty$ . The low velocity limit also allows us to express the energy in terms of the rest mass ( $KE \approx 0$ ) [48]

$$\mathcal{E} \approx mc^2. \quad (5.72)$$

We then expand the Hamiltonian around  $\frac{1}{c}$  at  $c = \infty$ , remembering that  $R_s = \frac{2GM}{c^2}$ . The first few terms of the expansion are

$$\mathcal{H} = \frac{1}{2m} \left( p_r^2 + p_z^2 + \left( \frac{L}{r} - \frac{Bqr}{2} \right)^2 \right) - \frac{GMm}{\sqrt{r^2 + z^2}}$$

$$\begin{aligned}
& + \frac{1}{2m} \left( \frac{GM(B^2q^2r^4 - 4L^2)}{2r^2\sqrt{r^2+z^2}} - \frac{2G^2M^2m^2}{r^2+z^2} - \frac{2GM(p_r^2+p_z^2)}{\sqrt{r^2+z^2}} \right) \left( \frac{1}{c^2} \right) \\
& + \mathcal{O}\left(\frac{1}{c^3}\right)
\end{aligned} \tag{5.73}$$

What we see here, is that the term independent of  $c$ , is exactly the Hamiltonian of the MNC case in Eq. (2.10), so for the limit  $c \rightarrow \infty$ , we get the complete MNC Hamiltonian. Note that  $R_s$  depends on  $c$ , so it also means that  $R_s \rightarrow 0$ , which is why collapse to the central black hole disappears for the MNC case.

Aside from the Hamiltonian, we can also find the correct limit for the analytical escape quantities, specifically, the minimum energy of escape  $U_{\text{esc,min}}$  and the asymptotes of escape  $r_{\text{esc}}$ . We first take the limit  $z \rightarrow \infty$  of Eq. (5.71) to get

$$\mathcal{H} = \frac{1}{2m} \left( -\frac{\mathcal{E}^2}{c^2} + (p_r^2 + p_z^2) + \left[ \frac{L}{r} - \frac{qB}{2}r \right]^2 \right) + \frac{1}{2}mc^2. \tag{5.74}$$

Then, we take the low-velocity limit through  $\mathcal{E} \approx mc^2$ , which cancels out the relevant terms and leaves

$$\mathcal{H} = \frac{1}{2m} \left( p_r^2 + p_z^2 + \left( \frac{L}{r} - \frac{qB}{2}r \right)^2 \right). \tag{5.75}$$

This is already equivalent to the MNC Hamiltonian in Eq. (2.10) in the limit  $z \rightarrow \infty$ . Unlike the full Hamiltonian, the minimum energy and asymptotes that could be derived have no relativistic correction terms, i.e., no  $c$  terms. So these analytical escape quantities are exactly the same for both the MNC and MBH cases. This is reasonable as the escape quantities are taken in the no gravity limit  $z \rightarrow \infty$ .

# Chapter 6

## Escapes from a Magnetized Black Hole

In this section, we will do much of the analysis done for the MNC case in chapter 3 and apply it to the MBH case. A similar definition of escape can be used for escapes along the infinities of  $z$ , but we now add the capture to the black hole as another possible basin of attraction for trajectories. The escape measures used in the MNC case, escape times and escape passes will be computed here, with the inclusion of the escape basin, giving us a total of 3 escape quantities. The general qualities of the escape quantity plots will be analyzed for multiple cases, which depend on the number of equilibrium points in the system. Lastly, 0-pass trajectories and trapped orbits will be shown to exist in the MBH case, just as they do for the MNC case.

### 6.1 Escape Definition

Due to the existence of the asymptotes of escape similar to the MNC case, we can use the exact same definition, where we compare the amplitudes of cyclotronic oscillation with the asymptotes of escape defined by Eq. (5.50). If the amplitudes are within the asymptotes, the trajectory is escaping either upwards,  $z \rightarrow \infty$ , or downwards,  $z \rightarrow -\infty$ . Now, we add a third possible “escape location”, which is capture towards the black hole.

To be more precise with our definition of escape location, we turn to *basins of attraction* [33, 34] or *basins of escape* [21, 26]. Chaotic trajectories, after an infinite amount of time, tend to asymptotically end up in certain regions of the phase space, called basins of attraction. For our open Hamiltonian system, these basins of attractions are the escape basin, upwards to  $z \rightarrow \infty$ , downwards  $z \rightarrow -\infty$ , and capture

into the black hole. We have not discussed this in the MNC case, as it is a simple conversion away from the escape pass, i.e., even-valued escape passes imply upward escapes, odd-valued escape passes imply downward escapes. Besides, there are not much physically relevant results that have been found for escape basins in the MNC. But because of the addition of the black hole capture, the escape basin of MBH now has relevance.

## 6.2 Escape Quantities

We now plot the 3 escape quantities that have been discussed, escape times, passes, and basins. For a given set of parameters  $(r_{\text{esc}}, \rho, E)$ , we choose trajectories that originate in the equatorial plane  $\theta = \pi/2$  with initial values  $R_0$  and  $p_0^R$  chosen as the points of the plot. The parameters  $(B, L)$  are can be obtained from Eqs. (5.62) and (5.63). The test charge is then launched upwards with  $p_{\theta 0} \leq 0$ , derived from the energy equation (5.41). We use a maximum integration time of  $t = 1,000$ .

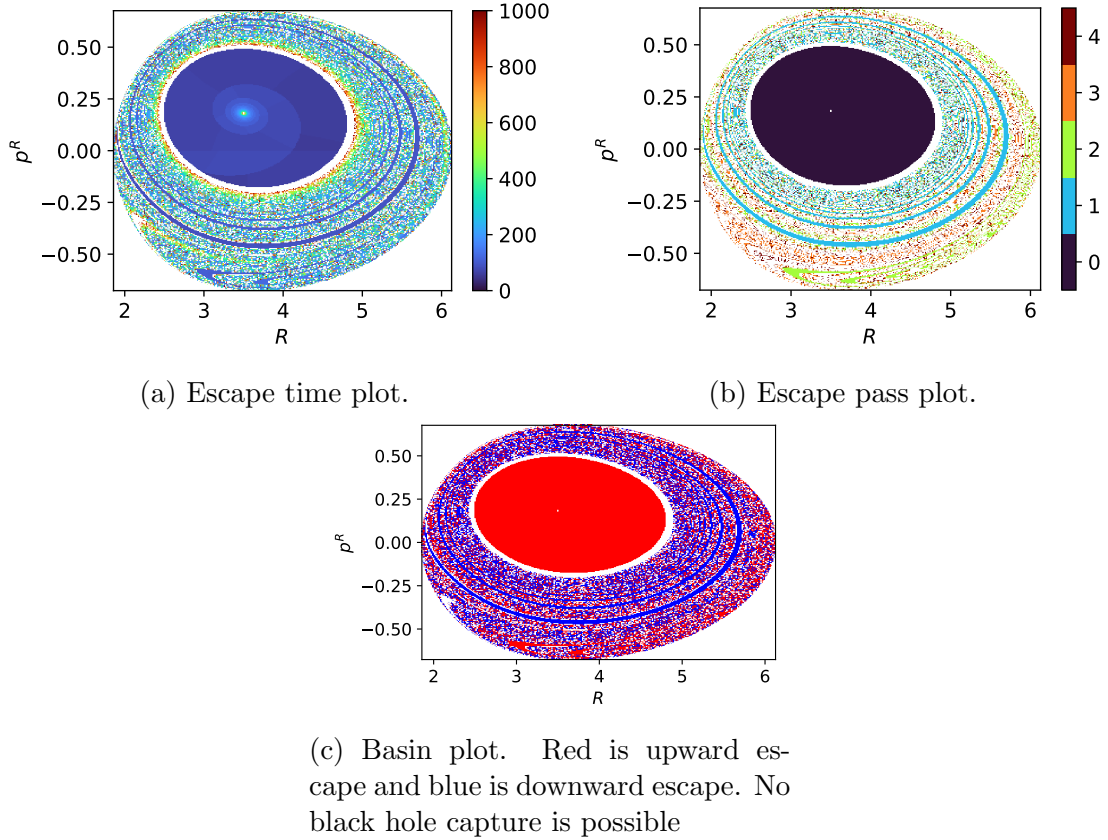


Figure 6.1: Case I: Black hole capture is impossible;  $(r_{\text{esc}}, \rho, E) = (4.0, 1.8, 1.2)$

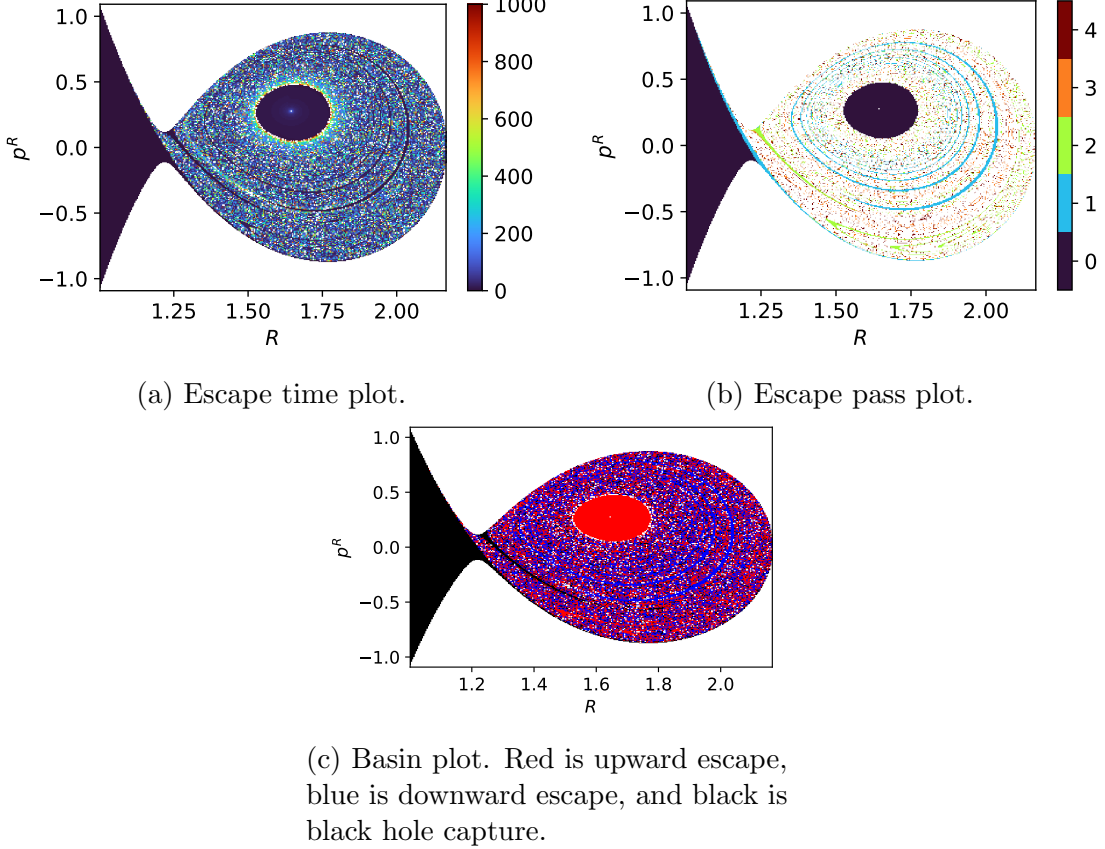


Figure 6.2: Case II: Black hole capture is possible;  $(r_{\text{esc}}, \rho, E) = (1.8, 1.2, 1.2)$

With this, we can generate 2d heatmap plots of each escape quantity. For escape time plots, we only plot trajectories that have escaped up to the maximum integration time. For escape pass plots, we plot only up to 4 passes, higher passes are omitted. For basin plots, we color upward escape in red, downward escape in blue, and black hole capture as black. We now show plots of 3 possible cases that relate to black hole capture. First for when the stable equilibrium point exists (i.e.,  $r_{\text{esc}} > r_{\text{esc,ISCO}}$  from Eq. (5.64)), we look at the cases where capture is impossible (I) and capture is possible (II). Lastly, we look at the case where no equilibrium points exists (i.e.,  $r_{\text{esc}} < r_{\text{esc,ISCO}}$ ) (III).

For case I in Fig. (6.1), we notice that the structure of the escape time and pass plots are very similar to the MNC case in Fig. (3.3). There exists an ordered set of trajectories with 0-passes, which directly escape upward to infinity, which we once again call the 0-pass trajectories. All other trajectories are those that return towards the equatorial plane, and scatter. For case II in Fig. (6.2), where black hole capture is permitted, a whole set of trajectories is added-those with initial conditions close to the

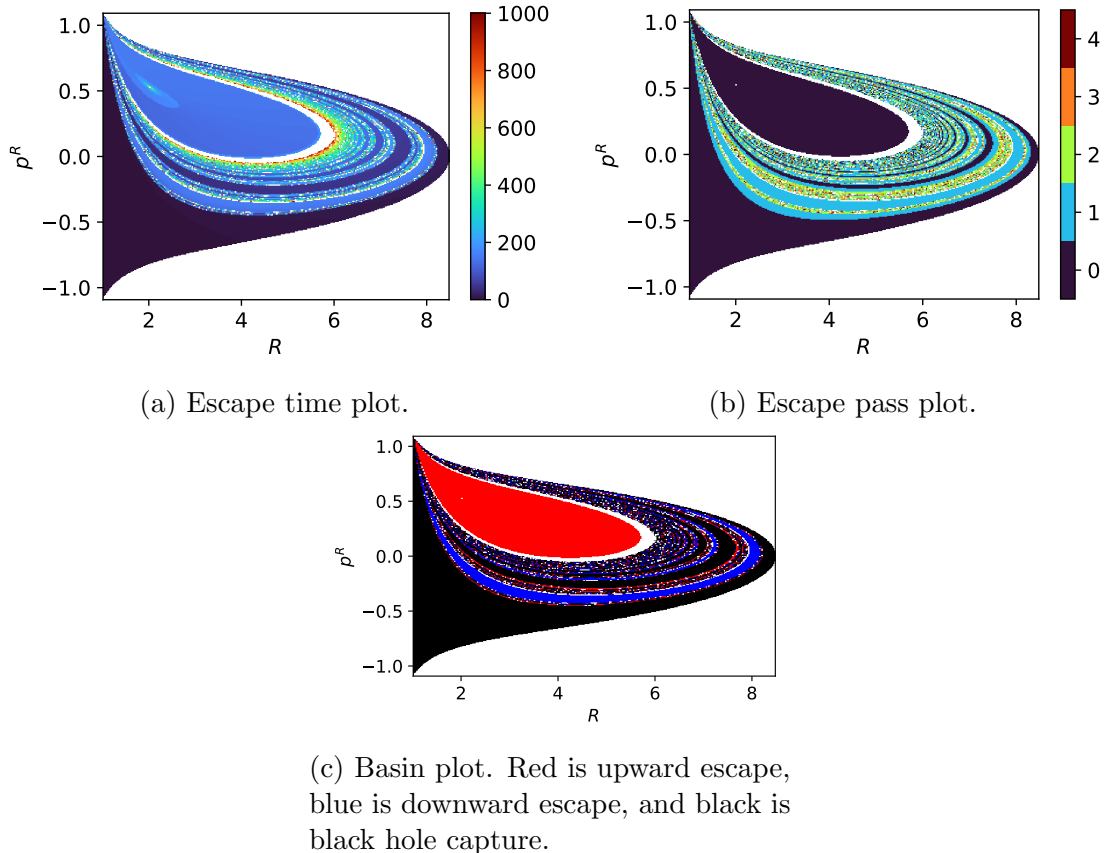


Figure 6.3: Case III: Black hole capture is possible;  $(r_{\text{esc}}, \rho, E) = (3.0, 2.8, 1.2)$

black hole surface  $R = 1$ . Most of the initial conditions near the black hole  $R \lesssim 1.2$  are captured by the black hole as shown in the basin plot. But generally, the structure is still similar to the MNC case, in the sense of existence of the 0-pass trajectories. Notice how some initial conditions near the black hole  $R \lesssim 1.2$ , can escape upwards or downwards, as long as their initial momentum  $p^R > 0$ , i.e. pointing away from the black hole. For case III in figure(6.3), where no equilibrium point exists, there still seems to be 0-pass trajectories, even close to the black hole, as long as  $p^R > 0$ . But a significant number of trajectories that have an initial  $p^R < 0$ , are captured by the black hole. This is reasonable as their initial trajectory are already moving towards the black hole. Note that inward pointing trajectories do not automatically mean escape. There are still trajectories that have  $p^R < 0$ , but still can escape, because of the deflection due to  $p_\theta$ .

Similar to what was found in the MNC case, one more quality of note in the escape time plots is the asymptotically increasing escape times as the initial conditions approach the ordered region as shown in Fig. (6.4), where we zoom in on the borders

of some ordered regions in Fig. (6.2). This can be explained once again by these trajectories having similar trajectories to the ordered trajectories they are surrounding, but will collapse back towards the equatorial plane due to their amplitudes of oscillation being outside the asymptotes of escape. The asymptotic escape time property does not occur near regions of ordered black hole capture, as trajectories whose initial conditions are close to that of the ordered region are immediately scattered, instead of following a similar path to the ordered set. This is demonstrated on Fig. (6.5), where two trajectories with close initial conditions are shown to immediately diverge from each other.

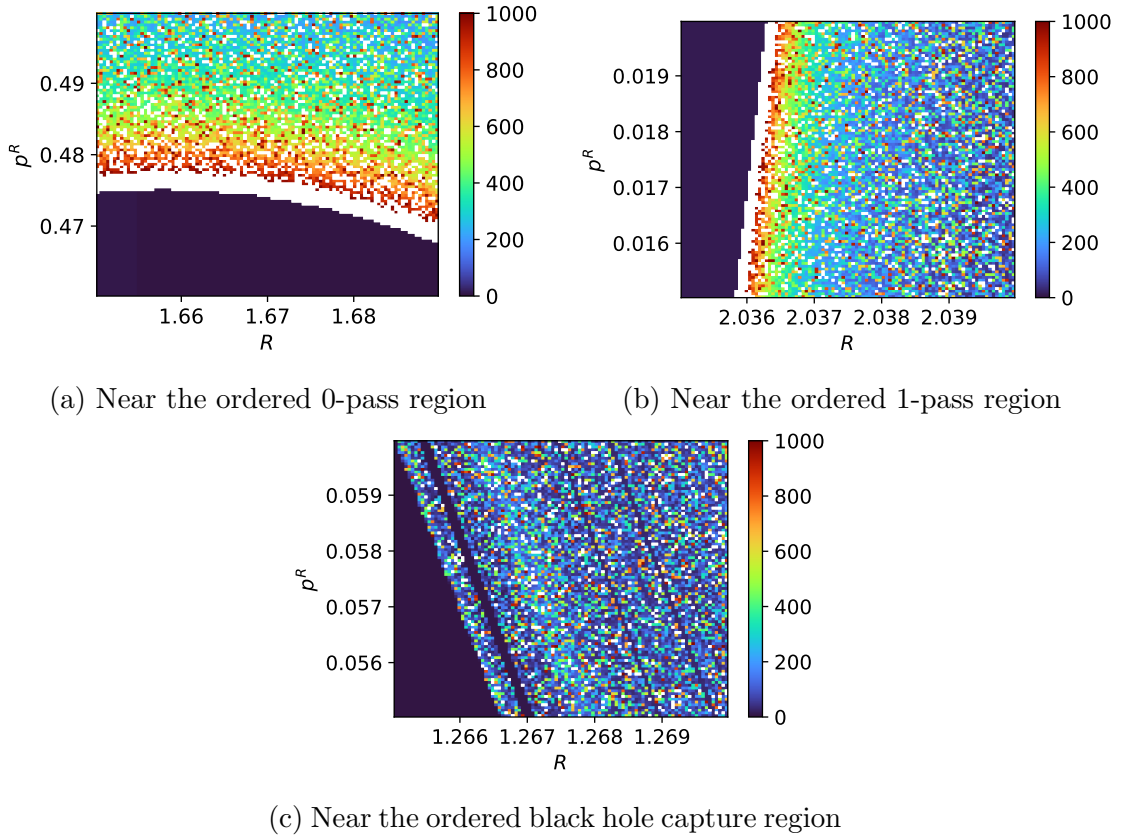


Figure 6.4: Zoom-ins on the borders of some ordered regions from Fig. (6.2) to demonstrate the asymptotically increasing escape times (a and b), or the lack thereof (c).

### 6.3 0-pass trajectories

Because the 0-pass trajectory ordered region is also present in the MBH case, we can analyze how the proportion of 0-pass trajectories changes for different parameters.

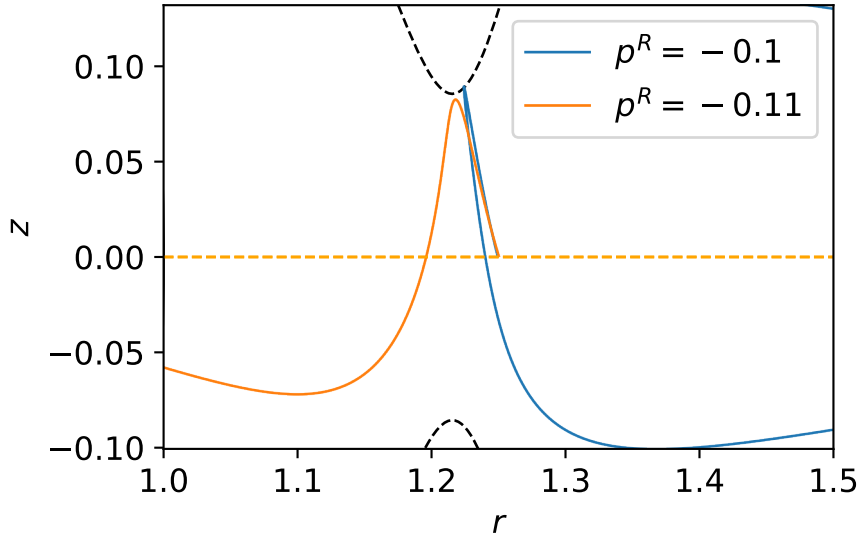


Figure 6.5: Two trajectories from case II, with initial conditions  $R = 1.25$ , and slightly different initial  $p^R$ . The equatorial plane (orange) and the ZVC (black) are also displayed.

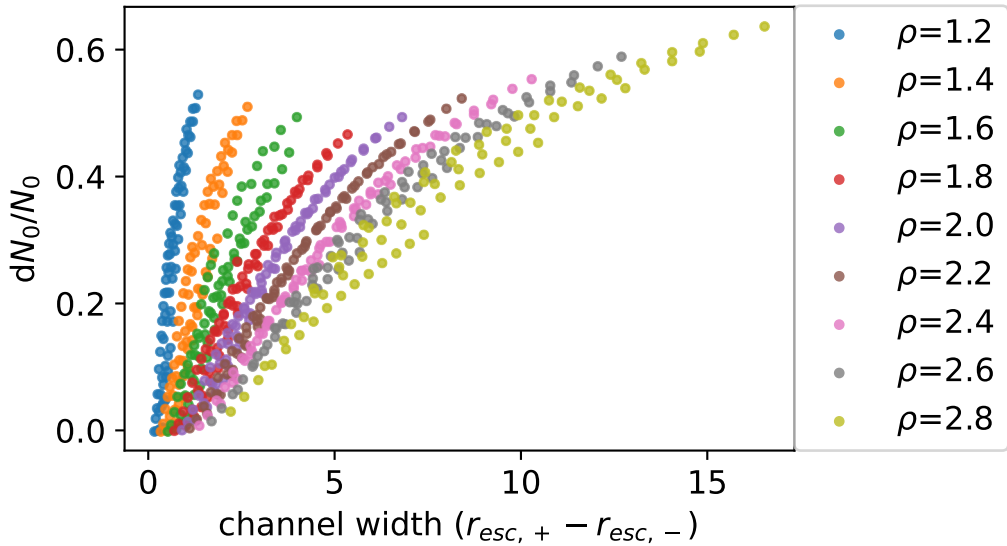


Figure 6.6: Proportion of 0-pass escaping trajectories to the total number of trajectories vs escape channel width. Each point represents a set of parameters  $E$ ,  $\rho$ , and  $r_{\text{esc}}$ .

We similarly postulate that the proportion of 0-pass trajectories once again depends on the width of the escape channel  $r_{\text{esc},+} - r_{\text{esc},-}$  from Eq. (5.50). The escape quantities are calculated for a set of parameters in the ranges  $r_{\text{esc}} \in [1.2, 4.0]$ ,  $\rho \in [1.2, 2.8]$  and  $E \in [1.2, 2.0]$ . Then, for each set of parameters, we calculated the proportion of initial conditions of 0-pass trajectories to the total number of kinematically allowed

initial conditions. The scatter plot of this is shown in Fig. (6.6), where each point represents a set of constants of motion.

We once again find that the width of the escape channel correlates with the proportion of the 0-pass escaping trajectories. But more interestingly,  $\rho$  affects this correlation. As discussed before, low  $\rho$  signifies strong magnetic interaction, and high  $\rho$  signifies weak magnetic interaction. As the plot shows, strong magnetic interactions allow more trajectories to directly escape for a smaller escape channel width. Meaning, stronger magnetic fields amplify the number of 0-pass trajectories for a given channel width.

## 6.4 Trapped Orbits

Orbits that do not escape even though their energies are above  $U_{\text{esc}}$ , seem to also exist in the MBH case as shown in Figs. (6.7) and (6.8). It is shown here for escape plots of increasing  $r_{\text{esc}}$ , as higher values seem to reduce the number of trajectories that escape for 1-pass or higher. We already know from the MNC case that these trajectories are trapped because they are ordered trajectories. But now the question becomes, for what sets of parameters do these trapped orbits exist, and how does the existence of black hole capture affect these ordered trajectories. Once again these questions will be answered in the next chapter.

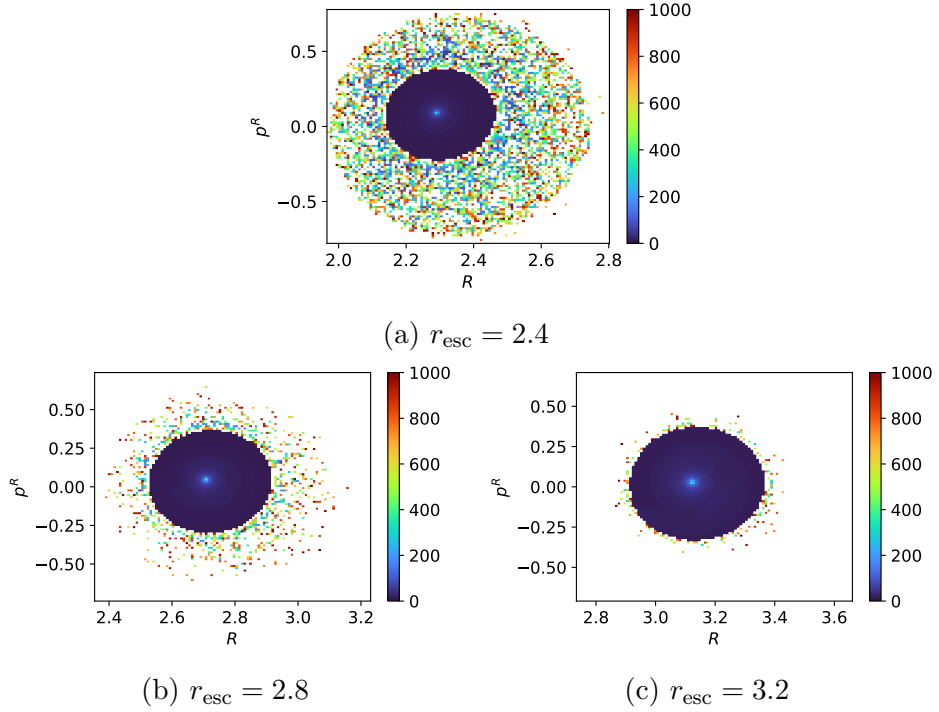


Figure 6.7: Escape time plots of increasing  $r_{\text{esc}}$ , with constant parameters  $\rho = 1.2$  and  $E = 1.2$ . Increasing  $L$  seems to decrease the number of escaping trajectories.

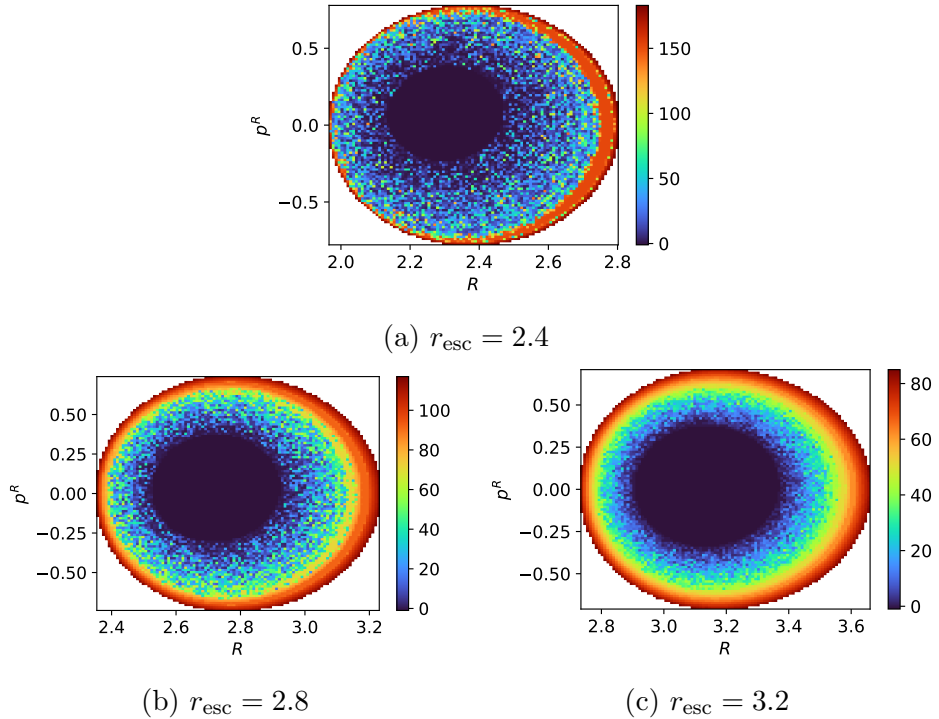


Figure 6.8: Escape pass plots of increasing  $r_{\text{esc}}$ , with constant parameters  $\rho = 1.2$  and  $E = 1.2$ . The regions with no escaping trajectories in Fig. (6.7) seem to have high number of passes.

# Chapter 7

## Chaos on a Magnetized Black Hole

Here we return to SALI, a measure of chaos, to analyze these trapped orbits introduced in Chapter (6). As established in Chapter 4, these trapped orbits are actually ordered orbits, in a sense that they should create asymptotically closed curves. This would imply that they do not escape, as escaping trajectories do not form closed curves. We do a similar analysis done on the MNC case, where we calculate the SALI, then calculate the percent of ordered trajectories/trapped orbits, then find for what sets of parameters these trapped orbits exist.

To calculate the SALI, we linearize the equations of motion, Eq.'s (5.37) to (5.40), to turn them into variational equations,

$$\begin{aligned} \dot{v}_{pR} &= \left( \frac{\mathcal{E}^2}{(R-1)^3} + \frac{p_R^2}{R^3} - \frac{3p_\theta^2}{R^4} - \frac{3L^2}{R^4 \sin^2 \theta} - B^2 \sin^2 \theta \right) v_R + \left( -\frac{p_R}{R^2} \right) v_{pR} \\ &\quad + \left( -\frac{2L^2 \cos \theta}{R^3 \sin^3 \theta} - RB^2 \sin(2\theta) \right) v_\theta + \left( \frac{2p_\theta}{R^3} \right) v_{p\theta}, \end{aligned} \quad (7.1)$$

$$\begin{aligned} \dot{v}_{p\theta} &= \left( -\frac{2L^2 \cos \theta}{R^3 \sin^3 \theta} - B^2 R \sin(2\theta) \right) v_R \\ &\quad + \left( -\frac{L^2(2 \cos^2 \theta + 1)}{R^2 \sin^4 \theta} - B^2 R^2 \cos(2\theta) \right) v_\theta, \end{aligned} \quad (7.2)$$

$$\dot{v}_R = \left( \frac{p_R}{R^2} \right) v_R + \left( 1 - \frac{1}{R} \right) v_{pR}, \quad (7.3)$$

$$\dot{v}_\theta = \left( -\frac{2p_\theta}{R^3} \right) v_R + \left( \frac{1}{R^2} \right) v_{p\theta}. \quad (7.4)$$

Using these, we can calculate SALI values for the same initial conditions in Chapter 6, which are  $r_{\text{esc}} \in [1.2, 4.0]$ ,  $\rho \in [1.2, 2.8]$  and  $E \in [1.2, 2.0]$ .

On Fig. (7.1), we plot the SALI values of the same set as the trapped orbits from Fig. (6.7). We once again see that the trapped orbits correspond to trajectories with SALI values of ordered orbits. So, the trapped orbits we see in the MNC case also

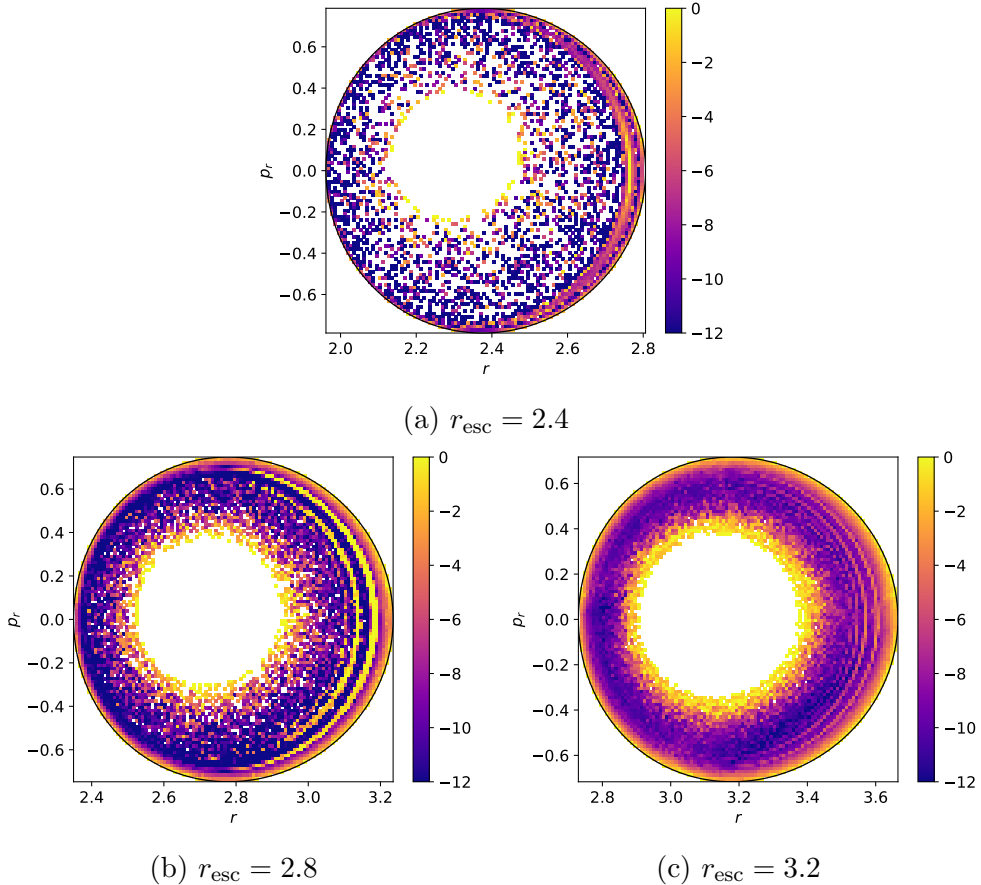


Figure 7.1: SALI plots of increasing  $r_{\text{esc}}$ , with constant parameters  $\rho = 1.2$  and  $E = 1.2$ . Escaping trajectories are omitted. The regions with no escaping trajectories in Fig. (6.7) have low SALI values.

occur for the trapped orbits in the MBH case. The question now is for what sets of parameters does these trapped orbits occur in? And does black hole capture affect these orbits?

We use the same prescription as that in Chapter 4, where ordered trajectories are those that have  $SALI > -1$ . We then count the number of ordered trajectories for a given set of parameters ( $E, r_{\text{esc}}, \rho$ ), then calculate the proportion of initial conditions that produce ordered orbits to all kinematically permitted initial conditions. These are plotted in Fig. (7.2).

Note that all the energies plotted in Fig. (7.2) are above the energy of escape, so all ordered trajectories here are already trapped orbits. Higher  $\rho$  value plots are not shown as the chosen range for  $r_{\text{esc}}$  and  $E$  made it so that their plots have no ordered orbits at all. It can be seen that trapped orbits occur for high  $r_{\text{esc}}$  values, meaning, trajectories whose escape channel are relatively far from the black hole center. Note

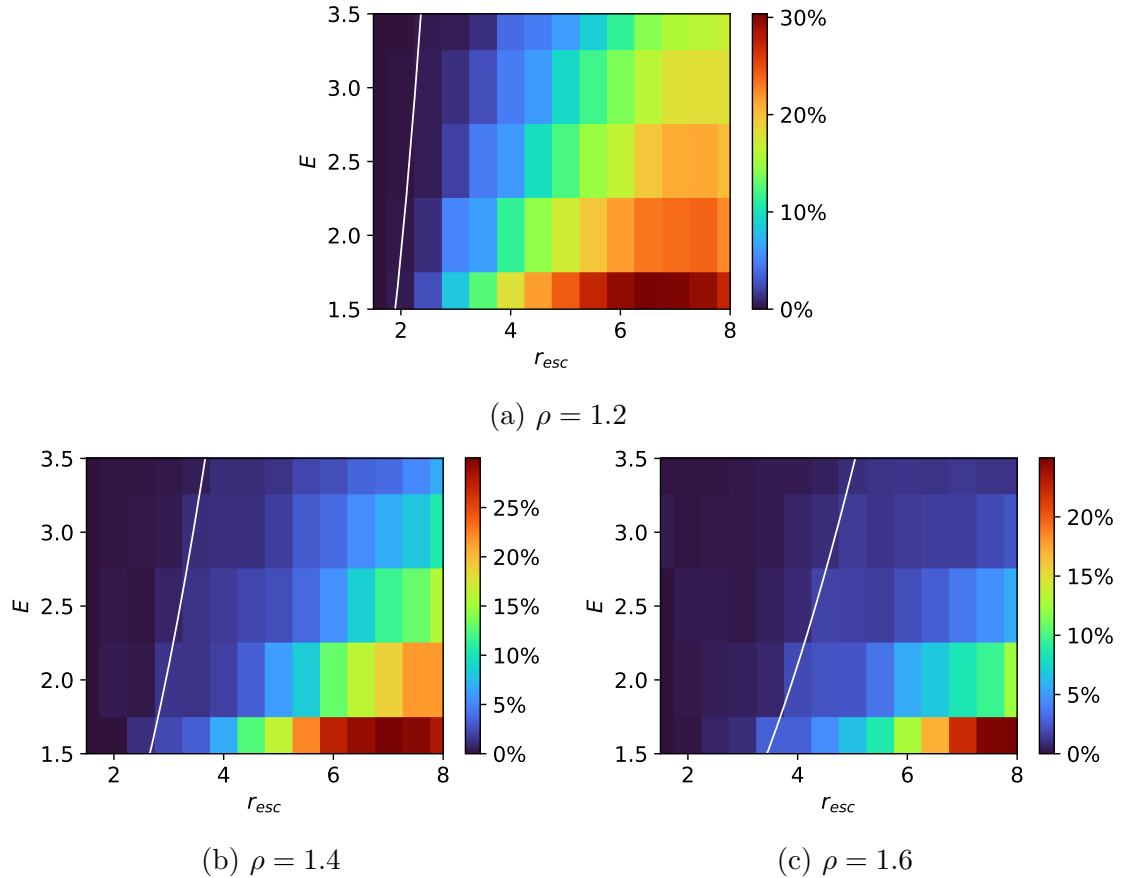


Figure 7.2: A plot of the percentage of ordered trajectories in a given set of parameters. The white line separates the region where black hole capture is possible (left of the line) and impossible (right of the line).

that this is a conclusion that can also be drawn for the MNC case. Remember that in Chapter 4, we concluded that trapped orbits occur for high  $L$  and Eq. (2.35) shows that  $r_{\text{esc}}$  is proportional to  $L$ . This means that the abundance of trapped orbits is proportional to  $r_{\text{esc}}$  for both MNC and MBH systems.

As shown by the white lines in the figures, these trapped orbits are very rare once black hole capture is possible. In other words, that if black hole capture is possible, most trapped orbits cease to exist. So trapped orbits generally exists given these 2 conditions: (1), the radius of the channel of escape  $r_{\text{esc}}$  for the given trajectory should be relatively far from the black hole center, and (2), the phase space should not be open to black hole capture, which is dictated by low energies and a  $r_{\text{esc}}$  value that is higher than the threshold in Eq. (5.64).

# Chapter 8

## Summary, Conclusions, and Recommendations

In this thesis, we studied the chaotic and escape dynamics of two systems, a charged massive particle orbiting either a point mass with Newtonian gravity or a black hole, both immersed in a uniform magnetic field. These two systems represent simplified models of astrophysical jets, where the plasma outflow is represented by the single charged particle. Because of the nature of these systems, we focused on describing, analyzing, and deriving conclusions on their escape and chaotic dynamics.

For the Newtonian gravity or the Magnetized Newtonian Center (MNC) case, we first derived its non-dimensionalized Hamiltonian, where we found 2 constants of motion: angular momentum and energy. We then fully described several qualities of the system. First, we identified the existence of a single equilibrium point, which implies that the potential energy is always strictly decreasing towards this equilibrium point, or that the effective force everywhere are attractive. Second, we found that that the phase space opens towards the infinities along the magnetic field direction, for a given energy called the energy of escape. This opening allows trajectories to possibly escape from the system. The Hamiltonian energy was also reparametrized, such that the escape energy is 1, this coincidentally made it so that under this reparametrized energy, there is a symmetry under a parity transformation of the angular momentum, meaning, we only need to study cases with positive angular momentum.

Escapes in MNC were then defined, as the typical definition of escape is not plausible in this system. This new escape definition is constructed using the asymptotic nature of the trajectory and phase space. A trajectory is escaping if the amplitudes of its cyclotronic oscillation are within the asymptotes of the phase space boundary.

This would imply that the trajectory will continue moving away from the equatorial plane. Using this new definition, we calculated 2 quantities that characterize escape for a given trajectory, escape time and escape pass. We found a set of ordered trajectories that directly escape from the system, called 0-pass trajectories. For initial conditions near the directly escaping trajectories and other ordered escaping sets, they initially act similar to these escaping trajectories, but because their amplitudes of oscillation are slightly outside the asymptotes of escape, they would eventually collapse back; the closer the initial condition is, the longer it would take for it to collapse. What this creates is an asymptotically increase in escape time as we choose initial conditions closer and closer to the 0-pass trajectory set. We also found that the proportion of trajectories, increase as the escape channel width increases, which is an intuitive result, as a larger channel would imply a larger amount of trajectories that can escape. Lastly, we found a set of trajectories that occur for high angular momentum, which never escape, and intersect the equatorial plane a high amount of times. These non-escaping trajectories are then called trapped orbits.

These trapped orbits are then studied using chaotic measures. The Single Alignment Index or SALI, is a measure of chaos, whose convergent value depends on whether the trajectory is ordered or chaotic. This is a quick, efficient, and accurate way to distinguish between order and chaos, which allows us to analyze the chaotic dynamics of the system for a large number of initial conditions and constants of motion. What this allowed us to find, is that these trapped orbits, are actually ordered trajectories. Them being ordered implies that they are asymptotically closed curves, and since closed curves cannot occur for escaping trajectories, they must never escape. These trapped orbits are found exclusively for high angular momentum cases.

All the analysis done above was similarly done for the case of a charged particle orbiting a uniformly magnetized black hole, or MBH. The Hamiltonian of the system is also derived and non-dimensionalized, then consequently analyzed. Because of the black hole, some qualities of the system are slightly different than the MNC case. The non-dimensionalization lead us to 3 parameters, energy  $\mathcal{E}$ , angular momentum  $L$ , and the magnetic interaction parameter  $B$ . There are between 0 to 2 equilibrium points, whose existence depends on the parameters  $L$  and  $B$ , where the special values are those that produces the Innermost Stable Circular Orbit or ISCO. For the parameters of the ISCO, there is only 1 equilibrium point, which is located at the radius of this

ISCO. The phase space also opens along the direction of the magnetic field, similar to the MNC case and the opening towards infinity is similar for both cases. But in this case, due to the proximity to the black hole, capture towards the black hole is also possible. Whether the black hole capture or escape to infinity opens first depends on the parameters. We similarly reparametrize the found constants, the energy, angular momentum, and magnetic interaction are reparametrized to escape energy  $E$ , ISCO radius  $\rho$ , and the radius of escape channel  $r_{\text{esc}}$ . This reparametrization once again introduces a symmetry under a parity transformation of the angular momentum.

For escapes from the MBH, the same definition as that of the MNC also applies, as the structure of the phase space boundary is very similar. The existence of 0-pass trajectories, the asymptotically increasing escape times as initial conditions approach that of any ordered set of escaping trajectories, and the existence of trapped orbits, all properties that are found in the MNC case, are also found in the MBH case. Due to the possible black hole capture, there are now some caveats to the above properties. For trajectories with no black hole capture, the structure of its escape time plot is extremely similar to the MNC case, but as we tune the parameters such that the phase space slowly open towards the black hole, more and more trajectories are then captured by the black hole. Also, the asymptotically increasing escape times do not exist for an ordered set of trajectories that are captured, unlike for the escapes toward infinity. Also, for the number of 0-pass trajectories, stronger magnetic interaction has more of these trajectories, for a smaller escape channel width, which implies that stronger magnetic interaction aids in escape.

Chaos also exists for this system, which again allows us to explain these trapped orbits as simply ordered trajectories. SALI was again used to measure the chaotic nature of trajectories in the MBH, then the proportion of ordered trajectories was also calculated, which leads to the following conclusion. Trapped orbits exists for escape channels that are relatively far from the black hole. Also, if black hole capture is possible, no trapped orbits exists.

Now, we can construct a possible picture of jets using these conclusions. Jets exists along the direction of the magnetic field, which is already known. And escapes require a certain amount of energy for it to even be possible. But energy is not the only factor for a trajectory to escape, we found that trajectories that seem to be escaping, may not escape if their amplitudes of oscillation are outside the asymptotes

of escape, so initial conditions also affect if a trajectory can escape or not in a finite time period. Even then, trapped orbits are found to exist, trajectories that have escaping energy, but do not escape even for an infinite amount of time. For these models of jets analysed, we found that specific choices of initial conditions can prevent escapes. This might explain why even though the magnetic field of Sagittarius A\* has been found, no jets from this black hole seems to have been observed. There are more limiting factors than just the energy that might prevent plasma from escaping the black hole for a given time period.

We also found that trapped orbits are more abundant in regions further from the gravitational center, i.e. larger  $r_{\text{esc}}$  would have more trapped orbits. This would imply for the accretion disk present around the black hole, if the MNC and MBH models are accurate, that the escaping jets are more prominent near the gravitational center. This is relevant as some models have shown that the magnetic field is also present in the accretion disk region, e.g. the Blandford-Znajek process.

There are multiple ways to extend this present work without extending to general relativistic magnetohydrodynamics. More accurate models can be used, e.g., the spin and charge of the black hole can be considered, non-uniform magnetic fields especially those that are closer to the twisted magnetic fields in the Blandford-Znajek process, which are closer to those observed in astrophysical systems, can also be used instead. The direct electric effects of the surrounding accretion disk may also have a non-negligible effect to the test charge. Different slicing of the plots could also be done to investigate non-equatorial initial conditions. Finally, the chaotic nature of the two systems can also be looked at more closely, expanding on the chaos analysis done here that only focused on escape analysis.

# Appendix A

## Code

Much of the numerics are done in `python`, with the aid of some packages like `NumPy`[49] for general numerics and array manipulation, `Numba`[50] as a JIT compiler, which heavily accelerates processing speed and with huge emphasis and acknowledgement of `Numba CUDA`, which allows GPU-accelerated parallel computing, and `Matplotlib`[51] for plotting and graphing. The code used is attached [here](#) or in the QR code below.

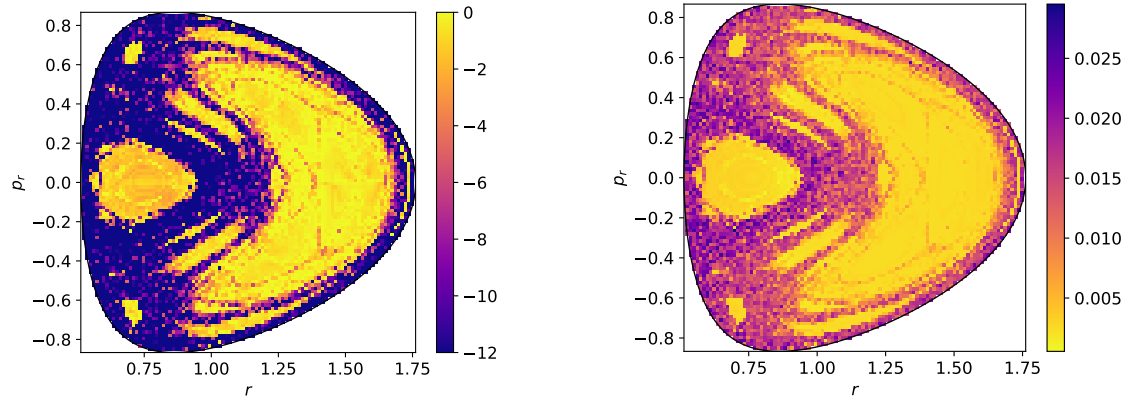


# Appendix B

## LCN vs SALI

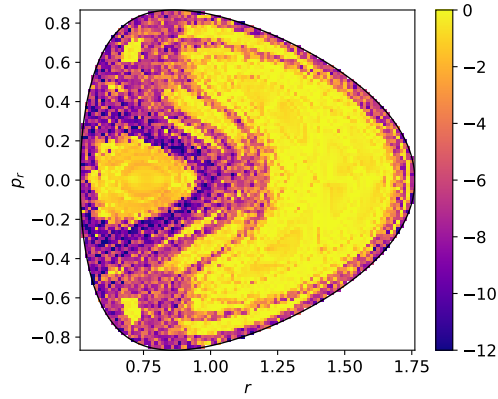
In chapter (4), it was asserted that the Lyapunov Characteristic Number (LCN) is a slowly converging value compared to the SALI, specifically for the purpose of discriminating ordered and chaotic trajectory. Here, we will show that though ultimately it is up to preference which of these two measures of chaos to use, SALI is comparatively faster. First, we replicate Fig. (4.8), but for a lower resolution in both SALI and LCN. We use  $\vec{v} = (0, 0, 1, 0)$  for the initial LCN deviation vector. We also measure the calculation time of running the code for generating these values. These plots are shown in Figs. (B.1a) and (B.1b). It can be seen that for the same integration time of  $t = 1000$ , the SALI plot produces a higher contrast between ordered and chaotic trajectories. So, with this, it is easier to choose the threshold value that separates ordered and chaotic trajectories with SALI, at the cost of higher calculation times. Note that the difference in calculation times adds up when we note that one of these plots represents a point in Fig. (4.12) for the MNC and Fig. (7.2). So small improvements in calculation time matters for the generation of these plots.

For a fairer comparison, we can plot the SALI for a lower integration time  $t = 500$  in Fig. (B.1c). Notice how this plot has a similar contrast to the LCN plot, which would lead to similar accuracies in discriminating between ordered and chaotic trajectories. We see that for SALI, we need a lower integration time compared to LCN to produce a similar contrast. This overall leads to a lower calculation time. So for the sake of efficiency and accuracy, we opted to use SALI over the LCN.



(a) SALI plot (integration time = 1000, calculation time  $\approx 900\text{s}$ )

(b) LCN plot (integration time = 1000, calculation time  $\approx 750\text{s}$ )



(c) SALI plot (integration time = 500, calculation time  $\approx 550\text{s}$ )

Figure B.1: Sample plots of SALI and LCN for the same constants of motion  $(L, E) = (1.0, 0.42)$  in the MNC system

# Bibliography

- [1] A. Einstein, “The foundation of the general theory of relativity,” 1916.
- [2] C. Davidson, F. W. Dyson, and A. S. Eddington, *A determination of the deflection of light by the Sun’s gravitational field, from observations made at the total eclipse of May 29, 1919.* 1920.
- [3] J. Earman and C. Glymour, *Relativity and eclipses: The British Eclipse Expeditions of 1919 and their predecessors.* 1980.
- [4] B. P. Abbott, R. Abbott, and e. a. Abbott, “Observation of gravitational waves from a binary black hole merger,” *Phys. Rev. Lett.*, vol. 116, p. 061102, Feb 2016.
- [5] E. H. T. Collaboration, “First m87 event horizon telescope results. i. the shadow of the supermassive black hole,” *The Astrophysical Journal Letters*, vol. 875, p. L1, Apr. 2019.
- [6] E. H. T. Collaboration, “First sagittarius a\* event horizon telescope results. VII. polarization of the ring,” *Astrophys. J. Lett.*, vol. 964, p. L25, Mar. 2024.
- [7] E. H. T. Collaboration, “First m87 event horizon telescope results. vii. polarization of the ring,” *The Astrophysical Journal Letters*, vol. 910, p. L12, Mar. 2021.
- [8] H. D. Curtis, “Descriptions of 762 Nebulae and Clusters Photographed with the Crossley Reflector,” *Publications of Lick Observatory*, vol. 13, pp. 9–42, Jan. 1918.
- [9] W. Baade and R. Minkowski, “On the Identification of Radio Sources.,” *APJ*, vol. 119, p. 215, Jan. 1954.
- [10] A. H. Bridle and R. A. Perley, “Extragalactic Radio Jets,” *ARAA*, vol. 22, pp. 319–358, Jan. 1984.

- [11] J. Beall, “Astrophysical jets: A review,” *Proceedings of Frontier Research in Astrophysics — PoS(FRAPWS2014)*, 2016.
- [12] R. D. Blandford and R. L. Znajek, “Electromagnetic extraction of energy from Kerr black holes.,” *MNRAS*, vol. 179, pp. 433–456, May 1977.
- [13] R. D. Blandford and D. G. Payne, “Hydromagnetic flows from accretion disks and the production of radio jets.,” *MNRAS*, vol. 199, pp. 883–903, June 1982.
- [14] B. Punsly, *Black Hole Gravitohydromagnetics*. Springer Berlin Heidelberg, 2009.
- [15] R. Wald, “Black hole in a uniform magnetic field,” *Physical Review D*, vol. 10, p. 1680–1685, September 1974.
- [16] A. N. Aliev and D. V. Gal’tsov, “Magnetized black holes,” *Sov. Phys. Uspekhi*, vol. 32, p. 75–92, Jan 1989.
- [17] V. Frolov and A. Shoom, “Motion of charged particles near a weakly magnetized schwarzschild black hole,” *Physical Review D*, vol. 82, October 2010.
- [18] A. M. Al Zahrani, V. P. Frolov, and A. A. Shoom, “Critical escape velocity for a charged particle moving around a weakly magnetized schwarzschild black hole,” *Physical Review D*, vol. 87, no. 8, 2013.
- [19] Y. Lim, “Motion of charged particles around a magnetized/electrified black hole,” *Phys. Rev. D*, vol. 91, p. 024048, January 2015.
- [20] Z. Stuchlík and M. Kološ, “Acceleration of the charged particles due to chaotic scattering in the combined black hole gravitational field and asymptotically uniform magnetic field,” *The European Physical Journal C*, vol. 76, January 2016.
- [21] J. Bautista and I. Vega, “Chaotic exits from a weakly magnetized schwarzschild black hole,” *Classical and Quantum Gravity*, vol. 38, p. 155016, July 2021.
- [22] E. Kunze, “Cosmological magnetic fields,” *Plasma Physics and Controlled Fusion*, vol. 55, p. 124026, November 2013.
- [23] A. Neronov and i. Vovk, “Evidence for strong extragalactic magnetic fields from fermi observations of tev blazars,” *Science*, vol. 328, p. 73–75, April 2010.

- [24] E. Zotos, “Elucidating the escape dynamics of the four hill potential,” *Nonlinear Dynamics*, vol. 89, pp. 135–151, March 2017.
- [25] E. Zotos, “An overview of the escape dynamics in the hénon–heiles hamiltonian system,” *Meccanica*, vol. 52, pp. 2615–2630, March 2017.
- [26] G. Contopoulos, *Order and Chaos in Dynamical Astronomy*. Astronomy and Astrophysics Library, Springer Berlin Heidelberg, 2013.
- [27] R. Churchill, G. Pecelli, and D. Rod, “Isolated unstable periodic orbits,” *Journal of Differential Equations*, vol. 17, no. 2, pp. 329–348, 1975.
- [28] G. Contopoulos, “Asymptotic curves and escapes in Hamiltonian systems,” *AAP*, vol. 231, pp. 41–55, May 1990.
- [29] C. V. Siopis, G. Contopoulos, and H. E. Kandrup, “Escape probabilities in a hamiltonian with two channels of escapea,” *Annals of the New York Academy of Sciences*, vol. 751, p. 205–212, May 1995.
- [30] C. Siopis, H. E. Kandrup, G. Contopoulos, and R. Dvorak, “Universal properties of escape in dynamical systems,” *The Dynamical Behaviour of our Planetary System*, p. 57–68, 1997.
- [31] G. Contopoulos and K. Efsthathiou, “Escapes and recurrence in a simple hamiltonian system,” *Celestial Mechanics and Dynamical Astronomy*, vol. 88, no. 2, p. 163–183, 2004.
- [32] G. Contopoulos, M. Harsoula, and G. Lukes-Gerakopoulos, “Periodic orbits and escapes in dynamical systems,” *Celest Mech and Dyn Astr*, vol. 113, p. 255–278, May 2012.
- [33] E. Ott, *Chaos in dynamical systems*. Cambridge Univ. Press, 2008.
- [34] H.-O. Peitgen, H. Jurgens, and D. Saupe, *Chaos and fractals: New frontiers of science*. Springer, 2012.
- [35] T. Bountis and C. Skokos, *Complex hamiltonian dynamics*. Springer, 2012.

- [36] C. Skokos, “Alignment indices: A new, simple method for determining the ordered or chaotic nature of orbits,” *Journal of Physics A: Mathematical and General*, vol. 34, no. 47, p. 10029–10043, 2001.
- [37] C. Skokos, C. Antonopoulos, T. C. Bountis, and M. N. Vrahatis, “Detecting order and chaos in hamiltonian systems by the sali method,” *Journal of Physics A: Mathematical and General*, vol. 37, no. 24, p. 6269–6284, 2004.
- [38] S. Strogatz, *Nonlinear Dynamics and Chaos: With applications to physics, biology, chemistry, and engineering*. CHAPMAN & HALL CRC, 2024.
- [39] E. E. Zotos, “Classifying orbits in the classical hénon–heiles hamiltonian system,” *Nonlinear Dynamics*, vol. 79, p. 1665–1677, Oct. 2014.
- [40] A. Zangwill, *Modern electrodynamics*. Cambridge: Cambridge Univ. Press, 2013.
- [41] R. McLachlan and P. Atela, “The accuracy of symplectic integrators,” *Nonlinearity*, vol. 5, pp. 541–562, March 1992.
- [42] M. H. Holmes, *Introduction to the foundations of Applied Mathematics*. Springer International Publishing, 2 ed., 2019.
- [43] E. H. T. Collaboration, “First sagittarius a\* event horizon telescope results. viii. physical interpretation of the polarized ring,” *The Astrophysical Journal Letters*, vol. 964, p. L26, mar 2024.
- [44] E. Ott and T. Tél, “Chaotic scattering: An introduction,” *Chaos: An Interdisciplinary Journal of Nonlinear Science*, vol. 3, no. 4, p. 417–426, 1993.
- [45] R. M. Wald, *General relativity*. Univ. of Chicago Press, 2009.
- [46] C. W. Misner, K. Thorne, J. A. Wheeler, and D. Kaiser, *Gravitation*. Princeton University Press, 2017.
- [47] E. Poisson, *A relativist’s toolkit: The mathematics of black-hole mechanics*. Cambridge University Press, 2007.
- [48] E. F. Taylor, *Spacetime Physics*. San Francisco,: W. H. Freeman, 1966.

- [49] C. Harris, K. Millman, S. van der Walt, R. Gommers, P. Virtanen, D. Cournapeau, E. Wieser, J. Taylor, S. Berg, N. Smith, R. Kern, M. Picus, S. Hoyer, M. van Kerkwijk, M. Brett, A. Haldane, J. del Río, M. Wiebe, P. Peterson, P. Gérard-Marchant, K. Sheppard, T. Reddy, W. Weckesser, H. Abasi, C. Gohlke, and T. Oliphant, “Array programming with NumPy,” *Nature*, vol. 585, pp. 357–362, Sept. 2020.
- [50] S. Lam, A. Pitrou, and S. Seibert, “Numba: A llvm-based python jit compiler,” in *Proceedings of the Second Workshop on the LLVM Compiler Infrastructure in HPC*, LLVM ’15, (New York, NY, USA), Association for Computing Machinery, 2015.
- [51] J. D. Hunter, “Matplotlib: A 2d graphics environment,” *Computing in Science & Engineering*, vol. 9, no. 3, pp. 90–95, 2007.